2019-04-27

Design of Random and Stationary Sources and Media for Structuring Light on Propagation and Scattering

Jia Li
University of Miami, jerry@aqchronos.com

UNIVERSITY OF MIAMI

DESIGN OF RANDOM STATIONARY SOURCES AND MEDIA FOR STRUCTURING LIGHT ON PROPAGATION AND SCATTERING

By

Jia Li

A DISSERTATION

Submitted to the Faculty
of the University of Miami
in partial fulfillment of the requirements for
the degree of Doctor of Philosophy

Coral Gables, Florida

May 2019

UNIVERSITY OF MIAMI

A dissertation submitted in partial fulfillment of
the requirements for the degree of
Doctor of Philosophy

DESIGN OF RANDOM STATIONARY SOURCES AND MEDIA FOR STRUCTURING LIGHT ON PROPAGATION AND SCATTERING

Jia Li

Approved:

_____
Olga Korotkova, Ph.D.
Professor of Physics

_____
Kenneth Voss, Ph.D.
Professor of Physics

_____
Mason Klein, Ph.D.
Assistant Professor of Physics

_____
Guillermo Prado, Ph.D.
Dean of the Graduate School

_____
Zhimin Shi, Ph.D.
Assistant Professor of Physics
University of South Florida

LI, JIA (Ph.D., Physics)
Design of Random Stationary Sources and Media for Structuring Light on Propagation and Scattering (May 2019)

Abstract of a dissertation at the University of Miami.

Dissertation supervised by Professor Olga Korotkova.
No. of pages in text. (104)

The dissertation incorporates a series of investigations relating to the design of coherence states for stationary, random sources, and correlation functions of spatially random, stationary media, for modulation of far fields radiated or scattered from them to the far zone, and, hence, for structuring of any observable statistical properties. In particular, we reveal how the coherence states of sources affect their far-zone radiated properties, including the spectral density, the scintillation index, and the intensity correlation function. Furthermore, we also present results that address how the spatial structuring of the refractive index correlation function of a three-dimensional (3D) medium influences the far-zone scattered spectral density of light. In so doing we have developed several novel, bona fide mathematical models for random stationary sources and media.

The first part of this thesis is dedicated to modeling of stationary 3D media. Our major contributions include modeling of media that produce a strongly peaked intensity profile off the scattering axis. Further, by extending the 2D laser coherent modes to those of a 3D medium, the Deterministic Mode Representation (DMR) method is introduced based on the eigenmode expansion of a broad class of stationary random media. This

method is envisioned to find applications to fine modeling and matrix-based reconstruction of correlations of spatially random media.

The second part of this thesis attributes to modeling of several novel classes of beam-like, partially coherent, stationary sources of Schell class, including Lorentz-correlated, Fractional Multi-Gaussian-correlated, and crescent-like sources. Specifically, we investigate, both analytically and experimentally, the evolution of beams radiated from the above-mentioned sources passing through the *ABCD* optical systems and atmospheric turbulence. The detailed synthesis procedures of these sources with the help of the Spatial Light Modulators (SLM) are outlined. In addition, we also achieve experimental realization of the I_m-Bessel-correlated beam via superposition of its coherent modes by using an SLM. These results are of importance for beam shaping, in Free Space Optical Communications and LIDAR sensing.

The third and the fourth parts of the thesis are concerned with two important natural media - atmospheric turbulence and soft biological tissues - being particular examples of the refractive index correlation functions that can influence the light statistics in a certain, well-defined manner. The third part of the thesis discusses sensing of correlation properties of the boundary-layer, non-classic atmospheric turbulence by laser light, in a single pass. In particular, a robust method is proposed to assess the anisotropy information of turbulence by using the two-point intensity correlation function of the optical beam obtained from experiments. The possibilities for sensing of non-classic, anisotropic turbulence via the Enhanced-Back Scatter (EBS) mechanism of collimated laser light in double passage mono-static link with a retro-reflector are also experimentally examined.

The final portion of the thesis includes in-depth investigations of laser light interaction with soft biological tissues, modeled as turbulent-like, stationary media. Since such media have been little explored so far for light propagation problems we first examine the important issue of a threshold depth at which the transition from weak to strong optical turbulence occurs, by examining the scintillation index of a plane wave. We also study the scintillation index of a spherical wave and of a Gaussian beam. Furthermore, an analytical method is introduced to solve both direct and inverse problems of weak scattering of light from a soft biological tissue. The results are of importance to optical sensing techniques for soft tissue diagnostics.

ACKNOWLEDGMENT

I would like to gratefully acknowledge many people who have provided me support in recent years as I have worked on this Ph.D. thesis. First, I would like to express the deepest appreciation to my Ph.D. advisor, Professor Olga Korotkova, who patiently guided me through my graduate education. Her unwavering enthusiasm for optical physics encouraged me constantly engaged with my research. Without her guidance and persistent help this dissertation would not have been possible.

I would like to sincerely appreciate the committee members, Dr. Kenneth Voss, Dr. Mason Klein, and Dr. Zhimin Shi for their encouragement, creative and comprehensive advice until this work came to existence.

Furthermore, I would like to thank Dr. Mohammad Hashemi for his guidance and strong support to enhance my experimental skills in lab.

Finally, I would like to express the deepest thanks to all my family members for their patience, support and encouragement to complete this work. They all keep me going, and this thesis would not have been possible without them.

Table of Contents

List of Figures

Chapter 1

Introduction

During the last several decades there has been a rapid development of the research field relating to coherent and partially coherent beam propagation through and scattering from deterministic and random media [1]. The coherence theory of stationary fields first proposed by Zernike [2] and further developed by Wolf, Thomson, van Cittert, Mandel, Glauber, Gamo, Gori, Goodman, and others has become an effective approach for complete characterization of the optical field observable properties on their propagation and interaction with various media [1-5]. Numerous methods have been devised to study statistical properties of coherent and partially coherent beams, including optical diffraction theorem [6], beam radiation theorem [7], angular spectrum representation [8-9], Wigner function method [10], as well as optical speckle theorem [11]. All these studies greatly inspired scientific interests to explore the effects of coherence and polarization of stationary random sources on their propagation or scattering properties [12-13]; and to examine the effects of media correlation on the light's scattered properties [14]. However, there is still a lack of studies that can completely utilize the intimate relations existing between a source's coherence state and the generated light's propagation properties, as well as between a medium's correlation state and the light's scattered characteristics. The specific aim of this thesis is to employ these relations in a detailed manner.

The thesis is organized as follows. In Chapter 1, we review the weak scattering theory of light from either a deterministic or random medium and introduce the fundamental nomenclature for dealing with stationary random sources and their

propagation properties through a variety of random media, including atmospheric turbulence and soft biological tissues. Moreover, we also review the mode decomposition theory of partially coherent random sources being an important theoretical frame for carrying out our work. Experimental synthesis procedures of random source generation are also reviewed for later use in our work. In Chapter 2, via modeling of two types of media's correlations to satisfy the non-uniform or Fractional Multi-Gaussian (FMG) functions, we show that the far-zone properties of generated light can be flexibly tuned by source parameters. We also introduce the Deterministic Mode Representation (DMR) of a 3D random medium and analyze the spectral density scattered to its far zone, under the assumption that the medium's spatial correlation is Gaussian. In Chapter 3 we present the methods for tuning the beams radiated from spatially random sources with the degree of coherence being Fractional Multi-Gaussian (FMG) and azimuthally non-symmetric types. We show that, through design of the source coherence states, the far-zone spectral densities of the radiated beams can be tuned to strongly focused and crescent-like profiles. Furthermore, we also develop the synthesis method of a classical random vortex beam via combinations of coherent modes. The method of measuring anisotropy of atmospheric turbulence is proposed in Chapter 4, and the experimental approach for producing the EBS effect is presented in the same chapter. Chapter 5 presents the solution to the direct and inverse scattering problems from soft biological tissues. We also investigate the scintillation index behavior of a plane wave, a spherical wave and a Gaussian beam in soft biological tissue. Then an analytic approach is proposed to determine the parameters of soft biological tissues.

1.1 Classical Theory of Weak Scattering

We start by reviewing the weak scattering theory of light waves from either a spatially deterministic or random medium. Weak scattering of light from a stationary, random medium indicates a situation in which a light wave first interacts with a medium transmits and then scatters far away from it. The scattering medium, in principle, can be spatially deterministic or have random nature, being either a single particle or collection of particles [15, 16]. First let us consider a scalar, monochromatic wave being a single component of the electric field vector:

$$U^{(i)}(\boldsymbol{r},t) = U(\boldsymbol{r},\omega)\exp(-i\omega t), \tag{1.1}$$

where $\boldsymbol{r}$ represents position vector, t and ω are time- and angular-dependent frequency, respectively. The optical field represented by Eq. (1.1) satisfies the Helmholtz differential equation [3]

$$\nabla^2 U(\boldsymbol{r},\omega) + k^2 n^2(\boldsymbol{r},\omega) U(\boldsymbol{r},\omega) = 0, \tag{1.2}$$

where $k=\omega/c$ is the wave number, $n(\boldsymbol{r}, \omega)$ denotes the spatially varying refractive index of medium, c is the speed of light in vacuum. We also define the scattering potential of the medium as a function of its refractive index, i.e.,

$$F(\boldsymbol{r},\omega) = \frac{1}{4\pi} k^2 \left[n^2(\boldsymbol{r},\omega) - 1 \right]. \tag{1.3}$$

Next, we may further assume that the total field $U^{(t)}(\boldsymbol{r},\omega)$ produced on scattering can be represented as the sum of the incident field, $U^{(i)}(\boldsymbol{r},\omega)$, and scattered field, $U^{(s)}(\boldsymbol{r},\omega)$:

$$U^{(t)}(\boldsymbol{r},\omega) = U^{(i)}(\boldsymbol{r},\omega) + U^{(s)}(\boldsymbol{r},\omega). \tag{1.4}$$

At the same time, the incident field $U^{(i)}(\boldsymbol{r},\omega)$ itself satisfies the Helmholtz differential equation

$$\left(\nabla^2+k^2\right)U^{(i)}(\boldsymbol{r},\omega)=0. \tag{1.5}$$

Based upon Eqs. (1.2), (1.4) and (1.5), one can further obtain the following expression for the total field by assuming that the scattered field is an outgoing spherical wave [Eq. (14) of [3], section 6.1]

$$U(\boldsymbol{r},\omega)=U^{(i)}(\boldsymbol{r},\omega)+\int_D F(\boldsymbol{r}',\omega)U(\boldsymbol{r}',\omega)G(|\boldsymbol{r}-\boldsymbol{r}'|,\omega)d^3r', \tag{1.6}$$

where D is the scatterer's volume and $G(|\boldsymbol{r}-\boldsymbol{r}'|,\omega)$ is the outgoing free-space Green function of the form

$$G(|\boldsymbol{r}-\boldsymbol{r}'|,\omega)=\frac{\exp(ik|\boldsymbol{r}-\boldsymbol{r}'|)}{|\boldsymbol{r}-\boldsymbol{r}'|}. \tag{1.7}$$

To obtain a more compact form for the scattered field, we suppose that the scattering between the incident wave and the medium is extremely weak, indicating that the magnitude of the scattered field is sufficiently small compared with that of the incident field, namely

$$U^{(t)}(\boldsymbol{r},\omega)=U^{(i)}(\boldsymbol{r},\omega)+\int_D F(\boldsymbol{r}',\omega)U^{(i)}(\boldsymbol{r}',\omega)G(|\boldsymbol{r}-\boldsymbol{r}'|,\omega)d^3r'. \tag{1.8}$$

By comparing Eqs. (1.4) with (1.8) we may readily represent the scattered field as

$$U^{(s)}(\boldsymbol{r},\omega)=\int_D F(\boldsymbol{r}',\omega)U^{(i)}(\boldsymbol{r}',\omega)G(|\boldsymbol{r}-\boldsymbol{r}'|,\omega). \tag{1.9}$$

Equations (1.8) and (1.9) are the well-known first-order Born approximation to the integral equation of potential scattering. Let the initial light field be a monochromatic plane wave at frequency ω, incident on the medium along direction specified by unit

vector $\boldsymbol{s}_0$. Then in the far zone of the medium the Green's function in Eq. (1.7) can be approximated as [Eq. (19) of [3], section 6.1]

$$G\left(\left|\boldsymbol{r}-\boldsymbol{r}'\right|,\omega\right)\approx\frac{\exp\left(ikr\right)}{r}\exp\left(-ik\boldsymbol{s}\cdot\boldsymbol{r}'\right), \tag{1.10}$$

where unit vector $\boldsymbol{s}$ describes the scattered wave direction. By these assumptions, it follows that the scattered field takes form

$$U^{(s)}\left(r\boldsymbol{s},\omega\right)=a\left(\omega\right)\frac{\exp\left(ikr\right)}{r}\tilde{F}\left[k\left(\boldsymbol{s}-\boldsymbol{s}_0\right),\omega\right], \tag{1.11}$$

where $\tilde{F}$ is introduced as the 3D Fourier transform of the scattering potential:

$$\tilde{F}\left[k\left(\boldsymbol{s}-\boldsymbol{s}_0\right),\omega\right]=\int_D F\left(\boldsymbol{r}',\omega\right)\exp\left[ik\left(\boldsymbol{s}-\boldsymbol{s}_0\right)\cdot\boldsymbol{r}'\right]d^3r'. \tag{1.12}$$

Equations (1.11) and (1.12) indicate that the far-zone scattered field is proportional to the 3D spatial Fourier transform of the scattering potential, meanwhile the field's amplitude is highly dependent of the scattered wave direction in the far zone.

1.2 Random, Stationary Fields

The original studies on random optical fields were made in the space-time domain. Suppose an optical field is scalar, occupies a finite region in the 2D space. Then it can be characterized by complex analytic signal $U(\boldsymbol{r}, t)$. The spatio-temporal correlation of the field is then characterized by the mutual coherence function which is the second-order statistical moment of field at two positions $\boldsymbol{r}_1$, $\boldsymbol{r}_2$ and two-time moments t_1, t_2 [17]

$$\Gamma\left(\boldsymbol{r}_1,\boldsymbol{r}_2;t_1,t_2\right)=\left\langle U^*\left(\boldsymbol{r}_1;t_1\right)U\left(\boldsymbol{r}_2;t_2\right)\right\rangle_t, \tag{1.13}$$

where the ensemble average is taken over a sufficiently long-time interval, and the asterisk denotes the complex conjugate. If the optical field is assumed to be random, wide-sense statistically stationary, Eq. (1.13) can be rewritten as [17]

$$\Gamma\left(\boldsymbol{r}_1,\boldsymbol{r}_2;\Delta\tau\right)=\left\langle U^*\left(\boldsymbol{r}_1;t\right)U\left(\boldsymbol{r}_2,t+\Delta\tau\right)\right\rangle_t, \tag{1.14}$$

where $\Delta\tau$ is the time delay between two moments. The mutual coherence function (1.14) satisfies a pair of partial differential equations [17]

$$\nabla_j^2\Gamma\left(\boldsymbol{r}_1,\boldsymbol{r}_2;\Delta\tau\right)-\frac{1}{c^2}\frac{\partial^2\Gamma\left(\boldsymbol{r}_1,\boldsymbol{r}_2;\Delta\tau\right)}{\partial\Delta\tau^2}=0,\qquad (j=1,2), \tag{1.15}$$

where ∇_j^2 is the Laplacian operator taken with respect to position vector $\boldsymbol{r}_j$. On taking the 2D Fourier transforms with respect to the two-time instants, Eq. (1.13) can be re-formulated to represent the wide-sense statistically stationary fields in the space-frequency domain. Then the so-called Cross-Spectral Density (CSD) function defined at two position vectors $\boldsymbol{r}_1$ and $\boldsymbol{r}_2$ and angular frequency ω can be obtained, being the Fourier transform of the mutual coherence function with respect to lag $\Delta\tau$. It can be understood as the ensemble average over the field's monochromatic realizations at frequency ω

$$W\left(\boldsymbol{r}_1,\boldsymbol{r}_2;\omega\right)=\left\langle U^*\left(\boldsymbol{r}_1;\omega\right)U\left(\boldsymbol{r}_2;\omega\right)\right\rangle_\omega, \tag{1.16}$$

and used as the second-order correlation function in space-frequency domain. Moreover, the Fourier transform of Eq. (1.15) implies that the CSD function given in Eq. (1.16) satisfies the Helmholtz equation:

$$\nabla_j^2W\left(\boldsymbol{r}_1,\boldsymbol{r}_2;\omega\right)+k^2W\left(\boldsymbol{r}_1,\boldsymbol{r}_2;\omega\right)=0,\qquad (j=1,2). \tag{1.17}$$

It has been shown that the CSD function of a stationary field must obey certain conditions [18]. First, it must be square-integrable over frequency ω, i.e.,

$$\int_0^{\infty} \left| W\left(\boldsymbol{r}_1, \boldsymbol{r}_2; \omega\right) \right|^2 d\omega < \infty. \tag{1.18}$$

Secondly, a CSD function should be continuous with respect to changes of its spatial variables

$$\int_{-\infty}^{+\infty} \int_{-\infty}^{+\infty} \left| W\left(\boldsymbol{r}_1, \boldsymbol{r}_2; \omega\right) \right|^2 d^2 r_1 d^2 r_2 < \infty. \tag{1.19}$$

Besides the conditions (1.18) and (1.19), the following two conditions should also be fulfilled for any arbitrary CSD function of planar source

$$W\left(\boldsymbol{r}_1, \boldsymbol{r}_2; \omega\right) = W^*\left(\boldsymbol{r}_2, \boldsymbol{r}_1; \omega\right), \tag{1.20}$$

and

$$\int_{-\infty}^{+\infty} \int_{-\infty}^{+\infty} W\left(\boldsymbol{r}_1, \boldsymbol{r}_2; \omega\right) f^*\left(\boldsymbol{r}_1\right) f\left(\boldsymbol{r}_2\right) d^2 r_1 d^2 r_2 \geq 0. \tag{1.21}$$

Equation (1.20) indicates that any CSD function must be quasi-Hermitian, while Eq. (1.21) that must hold for any function $f(\boldsymbol{r}_j)$, is known as non-negative definiteness condition. In addition, according to the Bochner's theorem, any CSD function of a stationary source must have the following representation [18]

$$W\left(\boldsymbol{r}_1, \boldsymbol{r}_2; \omega\right) = \int \int_{-\infty}^{+\infty} p\left(\boldsymbol{v}; \omega\right) H^*\left(\boldsymbol{r}_1, \boldsymbol{v}; \omega\right) H\left(\boldsymbol{r}_2, \boldsymbol{v}; \omega\right) d^2 v, \tag{1.22}$$

where H is an arbitrary function, $p(v)$ is a non-negative function of variable v.

1.3 Mode Decomposition of Random, Stationary Source

The mode decomposition of a random, stationary source is based upon classical optical coherence theory. By employing the classical description, we assume that $U(\boldsymbol{r}, t)$ represents a fluctuating scalar source localized within finite domain D. Here $\boldsymbol{r}$ denotes position vector of a typical point and t represents time. The fluctuations are supposed to

be characterized by a stationary ensemble. Let Γ denote the cross-correlation function of a source distribution $U(\boldsymbol{r}, t)$, as formulated by Eq. (1.14). We further assume that Γ function falls off sufficiently rapidly with $\Delta\tau$ so that it is absolutely integrable with respect to $\Delta\tau$. Consequently, the following Fourier pair holds true

$$W(\boldsymbol{r}_1, \boldsymbol{r}_2; \omega) = \frac{1}{2\pi} \int_{-\infty}^{+\infty} \Gamma(\boldsymbol{r}_1, \boldsymbol{r}_2; \Delta\tau) e^{i\omega\Delta\tau} d\tau, \tag{1.23}$$

where W is the CSD function of the source which satisfies the square-integrable, Hermitian, and non-negative definiteness properties, as shown by Eqs. (1.19)-(1.21). According to the Mercer's theorem, it admits a uniformly and convergent expansion [19]

$$W(\boldsymbol{r}_1, \boldsymbol{r}_2; \omega) = \sum_n \lambda_n(\omega) \phi_n^*(\boldsymbol{r}_1; \omega) \phi_n(\boldsymbol{r}_2; \omega), \tag{1.24}$$

where ϕ_n is the eigenfunction and λ_n is the eigenvalue of the Fredholm integral equation

$$\int_D W(\boldsymbol{r}_1, \boldsymbol{r}_2; \omega) \phi_n(\boldsymbol{r}_1; \omega) d^3 r_1 = \lambda_n(\omega) \phi_n(\boldsymbol{r}_2; \omega). \tag{1.25}$$

We stress that Eqs. (1.24) and (1.25) are valid whenever the set of the eigenfunctions $\phi_n(\boldsymbol{r})$ is complete in the Hilbert space of functions that are square-integrable throughout the domain D. Since each term in the right hand of Eq. (1.24) is factorized with respect to the variables $\boldsymbol{r}_1$ and $\boldsymbol{r}_2$ Eq. (1.24) represents the CSD function of the fluctuating source as a linear combination of contributions from spatially completely coherent elementary sources. Let us consider the special case of a partially coherent, Gaussian Schell-model source whose CSD function has the following form

$$W(\boldsymbol{r}_1, \boldsymbol{r}_2; \omega) = A_0 \exp\left[-p_0^2 (\boldsymbol{r}_1 + \boldsymbol{r}_2)^2 - m_0^2 (\boldsymbol{r}_1 - \boldsymbol{r}_2)^2 \right], \tag{1.26}$$

with

$$p_0^2 = \frac{1}{8\sigma_0^2}, \qquad m_0^2 = \frac{1}{8\sigma_0^2} + \frac{1}{2\delta_0^2}, \tag{1.27}$$

where σ_0 and δ_0 are effective width and coherence length of the Gaussian Schell-model source. For such source type, its CSD function can be factorized in the 2D Cartesian coordinates (x_i, y_i), (i=1, 2)

$$W(x_1, y_1, x_2, y_2; \omega) = \sum_{j=0}^{\infty} \sum_{h=0}^{\infty} \mu_{jh} \phi_{jh}^{*}(x_1, y_1; \omega) \phi_{jh}(x_2, y_2; \omega), \tag{1.28}$$

where the eigenfunctions are given by [20]

$$\phi_{jh}(x, y) = (2/\pi)^{1/2} \left(2^{j+h} j!h!\right)^{-1/2} \frac{1}{v_0} H_j\left(\frac{\sqrt{2}x}{v_0}\right) H_h\left(\frac{\sqrt{2}y}{v_0}\right) \exp\left(-\frac{x^2 + y^2}{v_0^2}\right), \tag{1.29}$$

and H_j is the jth Hermite polynomial, while the eigenvalues μ_{jh} are of the form

$$\mu_{jh} = \mu_0 q^{j+h}, \quad (j, h=0, 1, 2,\ldots). \tag{1.30}$$

The parameters v_0, μ_0, and q entering Eqs. (1.29) and (1.30) depend on A_0, m_0, and p_0 in the following way

$$v_0 = \frac{1}{(2m_0 p_0)^{1/2}}, \quad \mu_0 = \frac{A_0 \pi}{(m_0 + p_0)^2}, \quad \mathrm{q} = \frac{m_0 - p_0}{m_0 + p_0}, \tag{1.31}$$

where m_0 and p_0 associated with σ_0 and δ_0 are given by Eq. (1.27).

1.4 Light Propagation through Spatially Random Medium

Suppose a scalar beam-like field $U(\boldsymbol{r}'; \omega)$ is generated by a planar source located in the plane z=0 at a point with position vector ***r'***. The beam propagates into the half-space (z>0) filled with a spatially random medium. If we assume that the fluctuations in the refractive index of the medium are weak, the propagating field located at position vector $\boldsymbol{r}$=($\boldsymbol{\rho}$, z) satisfies the Helmholtz equation

$$\nabla^2 U(\boldsymbol{r}; \omega) + k^2 n^2(\boldsymbol{r}; \omega) U(\boldsymbol{r}; \omega) = 0. \tag{1.32}$$

The solution to Eq. (1.32) can be obtained as the form of the extended Huygens-Fresnel integral under the paraxial wave assumption

$$U(\boldsymbol{r};\omega) = -\frac{ik\exp(ikz)}{2\pi z}\int U(\boldsymbol{r}';\omega)\exp\left[ik\frac{(\boldsymbol{\rho}-\boldsymbol{\rho}')^2}{2z}\right]\exp\left[\Psi(\boldsymbol{\rho}',\boldsymbol{r};\omega)\right]d^2\rho', \quad (1.33)$$

where $\Psi(\boldsymbol{\rho}', \boldsymbol{r}; \omega)$ is the phase change induced by the random medium. Recalling the propagation law for the CSD function given in Eq. (1.16), and on substituting from Eq. (1.33) into Eq. (1.16), we find that the CSD function of the beam at distance z takes form

$$W(\boldsymbol{r}_1,\boldsymbol{r}_2;\omega) = \iint W(\boldsymbol{\rho}_1',\boldsymbol{\rho}_2';\omega)K(\boldsymbol{r}_1,\boldsymbol{r}_2;\boldsymbol{\rho}_1',\boldsymbol{\rho}_2';\omega)d^2\rho_1'd^2\rho_2', \quad (1.34)$$

where K is the propagator given by the expression

$$\begin{aligned} K(\boldsymbol{r}_1,\boldsymbol{r}_2;\boldsymbol{\rho}_1',\boldsymbol{\rho}_2';\omega) &= \left(\frac{k}{2\pi z}\right)^2\exp\left[-ik\frac{(\boldsymbol{\rho}_1'-\boldsymbol{\rho}_1)^2-(\boldsymbol{\rho}_2'-\boldsymbol{\rho}_2)^2}{2z}\right] \\ &\times\left\langle\exp\left[\Psi^*(\boldsymbol{\rho}_1',\boldsymbol{r}_1;\omega)+\Psi(\boldsymbol{\rho}_2',\boldsymbol{r}_2;\omega)\right]\right\rangle_M, \end{aligned} \quad (1.35)$$

where the angular bracket denotes the correlation function of phase perturbation induced by the random medium, and the subscript M represents the average over the fluctuating medium ensemble. On assuming that the medium satisfies the homogeneous and isotropic turbulence (power law) statistics, the correlation function of phase perturbation in Eq. (1.35) can be further expressed by the power spectrum $\Phi_n(\kappa)$ as [21]

$$\begin{aligned} &\left\langle\exp\left[\Psi^*(\boldsymbol{\rho}_1',\boldsymbol{r}_1;\omega)+\Psi(\boldsymbol{\rho}_2',\boldsymbol{r}_2;\omega)\right]\right\rangle_M \\ &= \exp\left[-4\pi^2k^2z\int_0^1\int_0^\infty\kappa\Phi_n(\kappa)\left[1-J_0\left[\left|(1-\xi)(\boldsymbol{r}_1-\boldsymbol{r}_2)+\xi(\boldsymbol{\rho}_1'-\boldsymbol{\rho}_2')\right|\kappa\right]\right]d\kappa d\xi\right], \end{aligned} \quad (1.36)$$

where J_0 denotes the zero-order Bessel function of the first kind. Under the assumption that the beam paraxially propagates through the medium, Eq. (1.35) becomes

$$K\left(\boldsymbol{r}_1,\boldsymbol{r}_2,\boldsymbol{\rho}_1',\boldsymbol{\rho}_2';\omega\right)=\left(\frac{k}{2\pi z}\right)^2\exp\left[-ik\frac{\left(\boldsymbol{\rho}_1'-\boldsymbol{\rho}_1\right)^2-\left(\boldsymbol{\rho}_2'-\boldsymbol{\rho}_2\right)}{2z}\right]$$
$$\times\exp\left[-\frac{\pi^2k^2z}{3}\left[\left(\boldsymbol{\rho}_1-\boldsymbol{\rho}_2\right)^2+\left(\boldsymbol{\rho}_1-\boldsymbol{\rho}_2\right)\cdot\left(\boldsymbol{\rho}_1'-\boldsymbol{\rho}_2'\right)+\left(\boldsymbol{\rho}_1'-\boldsymbol{\rho}_2'\right)^2\right]\right. \tag{1.37}$$
$$\left.\times\int_0^\infty\kappa^3\Phi_n\left(\kappa\right)d\kappa\right].$$

Another method for treating optical beams propagation in random media is known as the angular spectrum decomposition [4-5]. The principle of the method is that the incident beam field can be decomposed into a series of plane waves having different wave vectors and propagating through the medium. The resultant field then can be obtained by superposition of the contributing fields from the individual plane waves. It is assumed that any beam-like field obeys the integral expression

$$U\left(\boldsymbol{r};\omega\right)=\iint a\left(\boldsymbol{u};\omega\right)P\left(\boldsymbol{r};\omega\right)d\boldsymbol{u}_\perp, \tag{1.38}$$

where $P(\boldsymbol{r};\omega)$ is a plane wave, $a(\boldsymbol{u};\omega)$ is the angular spectrum with $\boldsymbol{u}$ being unit vector. Then the CSD function of the propagating beam at two position vectors $\boldsymbol{r}_1$ and $\boldsymbol{r}_2$ takes form

$$W\left(\boldsymbol{r}_1,\boldsymbol{r}_2;\omega\right)=\iint\iint a^*\left(\boldsymbol{u}_1;\omega\right)a\left(\boldsymbol{u}_2;\omega\right)\left\langle P^*\left(\boldsymbol{r}_1;\omega\right)P\left(\boldsymbol{r}_2;\omega\right)\right\rangle du_{1\perp}du_{2\perp}. \tag{1.39}$$

It is noteworthy that Eq. (1.39) can be alternatively written as

$$W\left(\boldsymbol{r}_1,\boldsymbol{r}_2;\omega\right)=\iint\iint A\left(\boldsymbol{u}_1,\boldsymbol{u}_2;\omega\right)\left\langle P^*\left(\boldsymbol{r}_1;\omega\right)P\left(\boldsymbol{r}_2;\omega\right)\right\rangle du_{1\perp}du_{2\perp}, \tag{1.40}$$

where

$$A\left(u_1,u_2;\omega\right)=\left\langle a^*\left(u_1;\omega\right)a\left(u_2;\omega\right)\right\rangle \tag{1.41}$$

is the angular correlation function of the source given by expression

$$A\left(\boldsymbol{u}_1,\boldsymbol{u}_2;\omega\right)=\frac{1}{\left(2\pi\right)^4}\iint\iint W\left(\boldsymbol{\rho}_1',\boldsymbol{\rho}_2';\omega\right)\left\langle P^*\left(\boldsymbol{\rho}_1';\omega\right)P\left(\boldsymbol{\rho}_2';\omega\right)\right\rangle d\rho_{1\perp}d\rho_{2\perp}. \tag{1.42}$$

Within the accuracy of the Rytov approximation, the CSD function of plane waves propagating in turbulence can be represented by product [4-5, 21]

$$\begin{aligned} W(\boldsymbol{r}_1,\boldsymbol{r}_2;\omega) &= P^*(\boldsymbol{r}_1;\omega)P(\boldsymbol{r}_2;\omega) \\ &\times\left\langle \exp\left[\psi^{(1)}(\boldsymbol{r}_1;\omega)+\psi^{(2)}(\boldsymbol{r}_1;\omega)+\psi^{(1)}(\boldsymbol{r}_2;\omega)+\psi^{(2)}(\boldsymbol{r}_2;\omega)\right]\right\rangle_M . \end{aligned} \tag{1.43}$$

The ensemble average in Eq. (1.43) can be approximated by retaining the terms up to the second order

$$\left\langle \exp[\psi]\right\rangle \approx \exp\left\{\left\langle\psi\right\rangle+\frac{1}{2}\left[\left\langle\psi^2\right\rangle-\left\langle\psi\right\rangle^2\right]\right\}. \tag{1.44}$$

With the help of Eq. (1.44), the CSD function in Eq. (1.43) can be further expressed as

$$W(\boldsymbol{r}_1,\boldsymbol{r}_2;\omega) = P^*(\boldsymbol{r}_1;\omega)P(\boldsymbol{r}_2;\omega)\exp\left[2E^{(1)}(\boldsymbol{r}_1,\boldsymbol{r}_2;\omega)+E^{(2)}(\boldsymbol{r}_1,\boldsymbol{r}_2;\omega)\right], \tag{1.45}$$

where $E^{(1)}$ and $E^{(2)}$ are given by the integral forms, respectively

$$E^{(1)}(\boldsymbol{r}_1,\boldsymbol{r}_2;\omega) = -\pi k^2\int_0^z d\xi\iint d^2\kappa\Phi_n(\xi,\boldsymbol{\kappa}), \tag{1.46}$$

$$E^{(2)}(\boldsymbol{r}_1,\boldsymbol{r}_2;\omega) = 2\pi k^2\int_0^z d\xi\iint d^2\kappa\Phi_n(\xi,\boldsymbol{\kappa})\exp\left[-i(z-\xi)(\boldsymbol{u_1}-\boldsymbol{u_2})\cdot\boldsymbol{\kappa}-i(\boldsymbol{r_2}-\boldsymbol{r_1})\cdot\boldsymbol{\kappa}\right]. \tag{1.47}$$

In Eqs. (1.46) and (1.47), ξ is the turbulence scale, Φ_n represents the power spectrum of the refractive index of turbulence, $\boldsymbol{\kappa}$ is 3D spatial frequency vector.

Chapter 2

Tuning the Scattered Properties of Light by Media Correlations

2.1 Deterministic Mode Representation of Stationary Random Medium

As is well known in functional analysis, the Mercer's theorem indicates that any non-negative definite, Hermitian operator can be expressed as a convergent summation of eigenmodes, being products of mutually orthogonal functions, which are weighted by a sequence of positive numbers. As a result, it may be feasible to represent a correlation function of a random field specified at a pair of spatial arguments as an infinite sum of weighted deterministic modes, each being a product of functions specified at a single spatial argument. Coherent-mode decomposition has played an important role in the analysis of multimode lasers [22]. The determination of the coherent modes of a given correlation function is never a simple task. The coherent-mode decomposition has the advantages to effectively reduce the complexity of propagation, diffraction, and scattering calculations for a variety of random light fields [23-27], and was used to elucidate the structure of non-radiating sources [28]. The modal expansion approach was also adopted to investigate a supercontinuum field generated in nonlinear fibers [29]. All these researches showed that it is more efficient to handle individual coherent modes rather than to solve wave equations for a specified partially coherent field.

In this section we use Mercer's theorem not for stationary light fields but rather for stationary scattering media that satisfy all necessary conditions. We first introduce the Deterministic Mode Representation (DMR) for the correlation function of the scattering

potential for a given medium, and then study the case when the Gaussian Schell-model medium type is assumed [30]. The DMR is further utilized to treat the far-field weak scattering of light from the medium, while the first-order Born approximation is adopted. The corresponding results are concluded, and potential applications of our study are also outlined.

2.1.1 Deterministic Mode Representation of Gaussian Schell-model Medium

We will now outline the method for describing a random stationary medium through its DMR. First let us consider a stationary random medium that occupies a 3D volume, and let its scattering potential be represented by $F_n(\boldsymbol{r}; \omega)$. For such a medium, the two-point correlation function of the scattering potential is given by expression [31-32]

$$C_F\left(\boldsymbol{r}_1,\boldsymbol{r}_2;\omega\right)=\left\langle F_n^*\left(\boldsymbol{r}_1;\omega\right)F_n\left(\boldsymbol{r}_2;\omega\right)\right\rangle_M. \tag{2.1}$$

The correlation function C_F is required to satisfy a set of conditions for the Hilbert-Schmidt kernel, i.e., square-integrability, hermiticity, and non-negative definiteness:

$$\int_D\int_D\left|C_F\left(r_1,r_2;\omega\right)\right|^2 d^3r_1 d^3r_2<\infty, \tag{2.2}$$

$$C_F\left(\boldsymbol{r}_2,\boldsymbol{r}_1;\omega\right)=C_F^*\left(\boldsymbol{r}_1,\boldsymbol{r}_2;\omega\right), \tag{2.3}$$

$$\int_D\int_D C_F\left(\boldsymbol{r}_1,\boldsymbol{r}_2;\omega\right)f^*\left(\boldsymbol{r}_1;\omega\right)f\left(\boldsymbol{r}_2;\omega\right)d^3r_1 d^3r_2\geq 0. \tag{2.4}$$

Here $f(\boldsymbol{r}; \omega)$ is an arbitrary square-integrable function, subscript "D" implies that the integration is taken over the entire medium volume. In general, the 3D Mercer's theorem stipulates that the correlation function C_F can be expressed by a convergent series of weighted modes [30]

$$C_F\left(\boldsymbol{r}_1,\boldsymbol{r}_2;\omega\right)=\sum_{n=0}^{\infty}\mu_n\left(\omega\right)\phi_n^*\left(\boldsymbol{r}_1;\omega\right)\phi_n\left(\boldsymbol{r}_2;\omega\right), \tag{2.5}$$

where μ_n and ϕ_n are the eigenvalues and eigenfunctions of the homogeneous Fredholm integral equation, and

$$\int_D C_F\left(\boldsymbol{r}_1,\boldsymbol{r}_2;\omega\right)\phi_n\left(\boldsymbol{r}_1;\omega\right)d^3r_1=\mu_n\left(\omega\right)\phi_n\left(\boldsymbol{r}_2;\omega\right). \tag{2.6}$$

The hermiticity and the non-negative definiteness of the correlation function indicate that all eigenvalues should be real and non-negative, i.e.,

$$\mu_n\left(\omega\right)\geq 0. \tag{2.7}$$

The eigenfunctions of the medium are orthogonal to each other, i.e.,

$$\int_D \phi_m^*\left(\boldsymbol{r};\omega\right)\phi_n\left(\boldsymbol{r};\omega\right)d^3r=\delta_{mn}\left(\omega\right), \tag{2.8}$$

where δ_{mn} is the Kronecker delta symbol. It is noteworthy that Eq. (2.5) takes the alternative form

$$C_F\left(\boldsymbol{r}_1,\boldsymbol{r}_2;\omega\right)=\sum_{n=0}^{\infty}\mu_n\left(\omega\right)C_n\left(\boldsymbol{r}_1,\boldsymbol{r}_2;\omega\right), \tag{2.9}$$

where

$$C_n\left(\boldsymbol{r}_1,\boldsymbol{r}_2;\omega\right)=\phi_n^*\left(\boldsymbol{r}_1;\omega\right)\phi_n\left(\boldsymbol{r}_2;\omega\right), \tag{2.10}$$

are the completely correlated modes. The correlation function specified at coinciding spatial arguments $\boldsymbol{r}_1=\boldsymbol{r}_2=\boldsymbol{r}$ is named as the strength of the scattering potential, i.e.,

$$I_F\left(\boldsymbol{r};\omega\right)=C_F\left(\boldsymbol{r},\boldsymbol{r};\omega\right). \tag{2.11}$$

Then, upon substituting from Eq. (2.9) into Eq. (2.11), we can readily obtain expression

$$I_F\left(\boldsymbol{r};\omega\right)=\sum_{n=0}^{\infty}\mu_n\left(\omega\right)I_n\left(\boldsymbol{r};\omega\right), \tag{2.12}$$

where

$$I_n(\boldsymbol{r};\omega) = C_n(\boldsymbol{r},\boldsymbol{r};\omega) = \left|\phi_n(\boldsymbol{r};\omega)\right|^2 \tag{2.13}$$

is the potential's strength of mode *n*, containing essential information about its intensity distribution, while eigenvalue $\mu_n(\omega)$ is a weighting factor of mode *n*, representing its maximum strength. By integrating Eq. (2.12) over the 3D volume of the medium, changing the order of integration, as well as using the property that

$$\int_D I_n(\boldsymbol{r};\omega)\, d^3r = 1, \tag{2.14}$$

one can find from Eq. (2.13) that

$$\int_D I_F(r;\omega)\, d^3r = \sum_{n=0}^{\infty} \mu_n(\omega), \tag{2.15}$$

which shows a close relation between the integrated scattering potential strength and the summation of all eigenvalues.

By following similar procedures of the mode decomposition of a random, stationary source shown in Chapter 1.3, we will now represent the correlation function of the 3D scattering medium in the Cartesian coordinate system. As a result, Eq. (2.5) becomes [30]

$$C_F(\boldsymbol{r}_1,\boldsymbol{r}_2;\omega) = \sum_{l=0}^{\infty}\sum_{m=0}^{\infty}\sum_{n=0}^{\infty} \mu_{lmn}(\omega)\, \phi_{lmn}^*(x_1,y_1,z_1;\omega)\, \phi_{lmn}(x_2,y_2,z_2;\omega), \tag{2.16}$$

where *l*, *m*, and *n* are the summation indexes along the *x*, *y*, and *z* axes, respectively. Let us now concentrate on a random, GSM medium type whose eigenvalues and eigenfunctions have the following forms

$$\mu_{lmn}(\omega) = A\mu_0^{3/2} q_0^{l+m+n} = A\frac{\pi^{3/2}}{(a_0+b_0)^3}\left(\frac{b_0-a_0}{b_0+a_0}\right)^{l+m+n}, \tag{2.17}$$

$$\phi_{lmn}(x,y,z)=\left(\frac{2}{\pi}\right)^{3/4}\left(2^{l+m+n}l!m!n!\right)^{-1/2}p_0^{-3/2}H_l\left(\frac{\sqrt{2}x}{p_0}\right)\times H_m\left(\frac{\sqrt{2}y}{p_0}\right)H_n\left(\frac{\sqrt{2}z}{p_0}\right)\exp\left(-\frac{x^2+y^2+z^2}{p_0^2}\right), \tag{2.18}$$

where

$$p_0=\frac{1}{\left(2a_0b_0\right)^2}, q_0=\frac{b_0-a_0}{b_0+a_0}, \mu_0=\frac{\pi}{\left(a_0+b_0\right)^2}, a_0^2=\frac{1}{8\sigma_0^2}, b_0^2=\frac{1}{8\sigma_0^2}+\frac{1}{2\delta_0^2}, \tag{2.19}$$

and $H_j(.)$ is the Hermite polynomial with order j. Upon substituting from Eqs. (2.17)-(2.19) into Eq. (2.16), we can readily obtain the correlation function of the scattering potential [30]

$$C_F(r_1,r_2;\omega)=A\left(\frac{2\mu_0}{\pi p_0^2}\right)^{3/2}\exp\left(-\frac{x_1^2+y_1^2+z_1^2+x_2^2+y_2^2+z_2^2}{p_0^2}\right)\times\sum_{l=0}^{\infty}\sum_{m=0}^{\infty}\sum_{p=0}^{\infty}\frac{\left(q_0/2\right)^{l+m+n}}{l!m!n!}H_l\left(\frac{\sqrt{2}x_1}{p_0}\right)H_m\left(\frac{\sqrt{2}y_1}{p_0}\right)H_n\left(\frac{\sqrt{2}z_1}{p_0}\right)\times H_l\left(\frac{\sqrt{2}x_2}{p_0}\right)H_m\left(\frac{\sqrt{2}y_2}{p_0}\right)H_n\left(\frac{\sqrt{2}z_2}{p_0}\right). \tag{2.20}$$

To perform further analysis, we define the Degree of Global Correlation (DGC) of a 3D stationary medium

$$l_g=\delta_0/\sigma_0, \tag{2.21}$$

Figs. 2.1(a) and 2.1(b) show the dependence of the eigenvalues of the GSM medium on the r.m.s. width of the strength of scattering potential, as well as the r.m.s. widths of the degree of correlation of the scattering potential. The eigenvalues consistently decrease with the increase of the mode numbers (l=m=n), no matter how σ_s and δ_s vary. For a medium with larger σ_s or δ_s, the corresponding eigenvalues are larger. For a medium with

δ_s =0.1λ, the eigenvalues are sufficiently small and remain invariant with increasing mode indexes.

The distribution of the individual eigenmodes of the GSM medium can be studied by using Eqs. (2.13) and (2.18)-(2.19). As shown in Fig. 2.2, the eigenmodes have Cartesian symmetry, and they can degenerate to classic Hermite-Gaussian laser modes as 2D projections onto the (x, y), (y, z) and (x, z) planes.

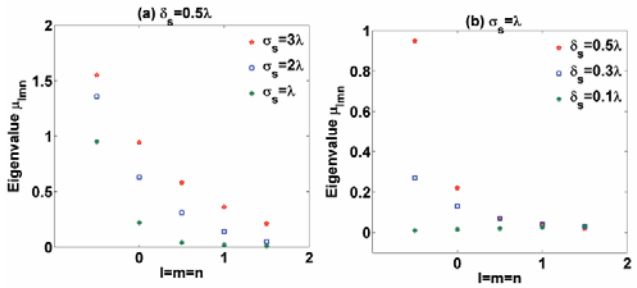

Fig. 2.1 The eigenvalues of the GSM-correlated medium versus the mode indexes (l=m=n) for (a) different potential strength r.m.s. widths: σ_s = λ, 2λ and 3λ, (b) different r.m.s. widths of potential's correlation: δ_s = 0.5λ, 0.3λ and 0.1λ. The figures are plotted from Eqs. (2.17) and (2.18) (from Fig. 2 of [30]).

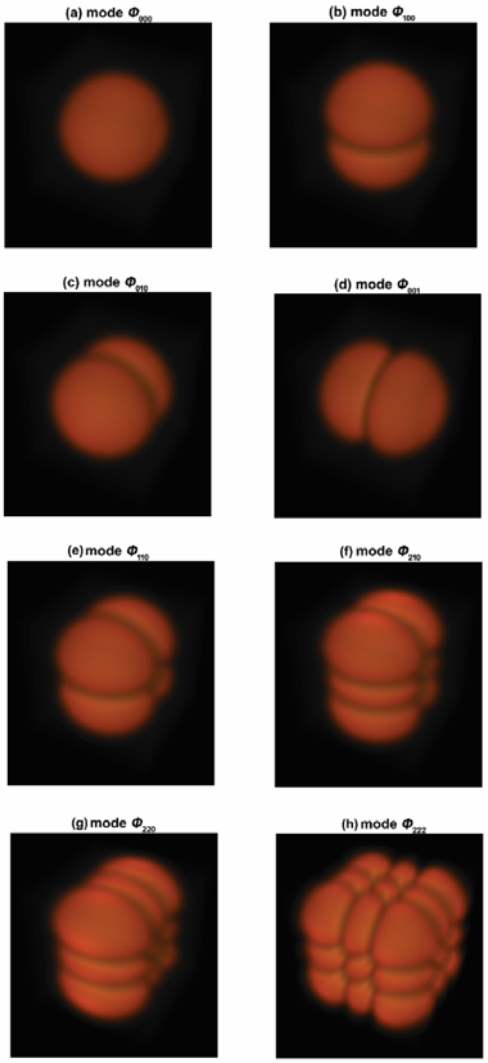

Fig. 2.2 3D profiles of individual eigenmodes of the medium. The scattering potential parameters are chosen as $\sigma_s=\lambda$, $\delta_s=0.2\lambda$. The figures are plotted from Eqs. (2.18)-(2.19) (from Fig. 3 of [30]).

2.1.2 Scattering from Random Medium with Deterministic Mode Representation

We now study the problem of far-field weak scattering of light from stationary media. First, we assume that a scalar, monochromatic plane wave is incident upon a 3D medium.

Then we further consider the CSD function of the scattered field in the far-zone region, implying that the Green's function has the far-zone approximation (see Eq. (1.10), section 1) [30]. Then the scattered CSD becomes

$$W^{(s)}\left(r's_1', r's_2'; \omega\right) = \frac{\left|a^{(i)}(\omega)\right|^2}{r'^2} \sum_{l=0}^{\infty}\sum_{m=0}^{\infty}\sum_{n=0}^{\infty} \mu_{lmn}(\omega)\left[\tilde{\phi}_{lmn}\left(\boldsymbol{K}_1'; \omega\right)\right]^* \tilde{\phi}_{lmn}\left(\boldsymbol{K}_2'; \omega\right), \quad (2.22)$$

where $\boldsymbol{K}_j' = k\left(\boldsymbol{s}_j' - \boldsymbol{s}_0\right)$ is the momentum transfer vector [31-32], and $\tilde{\phi}_{lmn}$ represents the Fourier transform of medium mode, i.e.,

$$\tilde{\phi}_{lmn}\left(\boldsymbol{K}_j'; \omega\right) = \int_D \phi_{lmn}(x, y, z) \exp\left(-i\boldsymbol{K}_j' \cdot \boldsymbol{r}\right) d^3 r. \quad (2.23)$$

Based on Eqs. (2.22) and (2.23), the far-zone scattered spectral density at two coinciding points contributed by all modes of the medium can be obtained by substituting from $\boldsymbol{s}_1' = \boldsymbol{s}_2' = \boldsymbol{s}'$ into Eq. (2.22):

$$S^{(s)}\left(r's'; \omega\right) = \frac{\left|a^{(i)}(\omega)\right|^2}{r'^2} \sum_{l=0}^{\infty}\sum_{m=0}^{\infty}\sum_{n=0}^{\infty} \mu_{lmn}(\omega)\left|\tilde{\phi}_{lmn}\left(\boldsymbol{K}'; \omega\right)\right|^2. \quad (2.24)$$

Eq. (2.24) indicates that the total spectral density scattered from a 3D medium can be represented as the summation of contributions from individual deterministic modes. Based upon this result, we can conclude that any desired intensity distribution of the scattered field can be generated by appropriately selecting medium's eigenmodes and eigenvalues. Moreover, if we further consider the scattered field in the 3D Cartesian coordinate system, Eq. (2.24) becomes

$$\begin{aligned} W^{(s)}\left(r's_1', r's_2'; \omega\right) = \frac{\left|a^{(i)}(\omega)\right|^2}{r'^2} \sum_{l=0}^{\infty}\sum_{m=0}^{\infty}\sum_{n=0}^{\infty} \mu_{lmn}(\omega)\left\{\tilde{\phi}_{lmn}\left[ks_{1x}', ks_{1y}', k\left(1 - s_{1z}'\right)\right]\right\}^* \\ \times \tilde{\phi}_{lmn}\left[ks_{2x}', ks_{2y}', k\left(1 - s_{2z}'\right)\right], \end{aligned} \quad (2.25)$$

where $s_{jx}', s_{jy}', s_{jz}'$ are components of the unit vectors $\boldsymbol{s}_j'$ (j=1,2) in the Cartesian coordinates. Further, the Fourier transforms of the individual modes have the form

$$\tilde{\phi}_{lmn}\left[ks_x', ks_y', k\left(1-s_z'\right)\right] = \int_D \phi_{lmn}\left(x,y,z\right)\exp\left\{-ik\left[s_x'x + s_y'y + \left(1-s_z'\right)z\right]\right\}dxdydz. \quad (2.26)$$

When deriving Eqs. (2.25) and (2.26), we have assumed that the incident plane wave propagates along the z axis; hence, s_{0x}=s_{0y}=0, s_{0z}=1. Furthermore, if we assume

$$\psi_{lmn}\left(r'\boldsymbol{s}';\omega\right) = \frac{a^{(i)}\left(\omega\right)}{r'}\tilde{\phi}_{lmn}\left(\boldsymbol{K}';\omega\right), \quad (2.27)$$

then Eqs. (2.25) and (2.27) result in the CSD of the scattered field, i.e.,

$$W^{(s)}\left(r'\boldsymbol{s_1}', r'\boldsymbol{s_2}';\omega\right) = \sum_{l=0}^{\infty}\sum_{m=0}^{\infty}\sum_{n=0}^{\infty}\mu_{lmn}\left(\omega\right)\psi_{lmn}^{*}\left(r'\boldsymbol{s_1}';\omega\right)\psi_{lmn}\left(r'\boldsymbol{s_2}';\omega\right). \quad (2.28)$$

From Eq. (2.28) it can be observed that the CSD function of the scattered field also obeys the DMR form. It is shown that the eigenvalues of the CSD of the scattered field remain unchanged, but its eigenmodes are proportional to the Fourier transforms of the eigenmodes of the 3D scatterer, except for the coefficient $a^{(i)}\left(\omega\right)/r'$ generally being a constant.

2.1.3 Examples and Concluding Remarks

Based on the equations derived in the previous section, we now investigate how the eigenmodes of the medium influence the scattered intensity profiles in the far field from a GSM medium. Upon substituting from Eqs. (2.17) and (2.18) into Eq. (2.25) and substituting $\boldsymbol{s}_1' = \boldsymbol{s}_2' = \boldsymbol{s}'$ into the same expression, the spectral density of the scattered field can be obtained by performing the Fourier transforms of the eigenmodes of the GSM medium, viz.,

$$S^{(s)}(r's') = \frac{A}{r'^2}\left(\frac{\sqrt{2}\pi p_0}{a_0+b_0}\right)^3 \exp\left[-k^2 p_0^2 (1-s_z')\right]$$
$$\times\sum_{l=0}^{\infty}\sum_{m=0}^{\infty}\sum_{n=0}^{\infty}\frac{1}{l!m!n!}\left(\frac{b_0-a_0}{2b_0+2a_0}\right)^{l+m+n} H_l^2\left(\frac{kp_0 s_x'}{\sqrt{2}}\right) \tag{2.29}$$
$$\times H_m^2\left(\frac{kp_0 s_y'}{\sqrt{2}}\right) H_n^2\left[\frac{kp_0}{\sqrt{2}}(s_z'-1)\right].$$

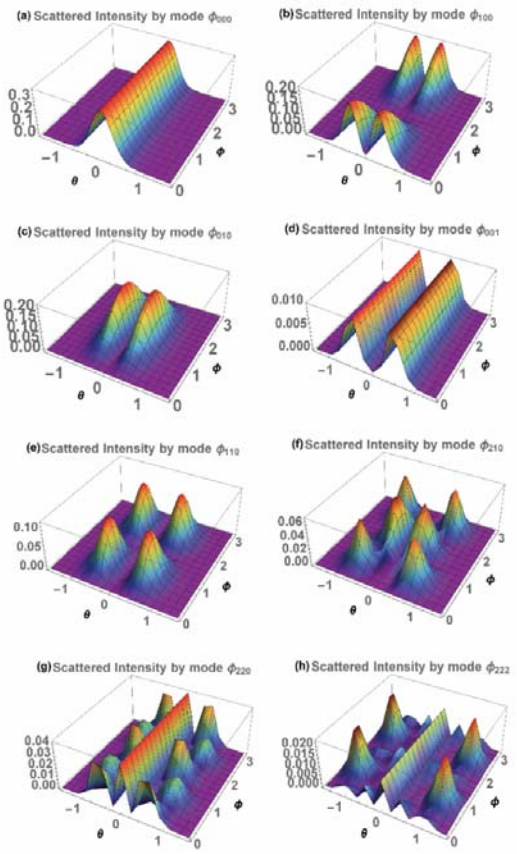

Fig. 2.3 3D plots of the spectral density scattered by individual eigenmodes of the medium for the same parameters as in Fig. 2.2. The figures are plotted from Eq. (2.29) (from Fig. 5 of [30]).

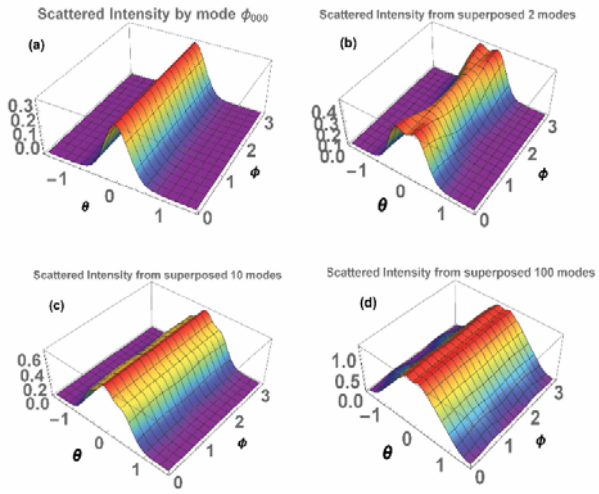

Fig. 2.4 3D plots of the spectral density scattered from superpositions of eigenmodes. The medium parameters are the same as in Fig. 2.2. The figures are plotted from Eq. (2.29) (from Fig. 6 of [30]).

Fig. 2.3 illustrates the spectral densities which scatter from individual deterministic modes of the medium, as shown by Fig. 2.2, while its dependence on polar and azimuthal angles ϕ and θ in the spherical coordinate are revealed in the figure.

Fig. 2.4 shows the far-field scattered intensities from the fundamental mode by superposition of 2, 10, and 100 deterministic modes, respectively. As of the stretching effects along the axes due to Hermite functions appeared in deterministic modes, the intensity contributed by the superposed eigenmodes exhibits the nonsymmetric profile, being observed extremely evident in Fig. 2.3(b) for ϕ=0 and ϕ=π. It is also interesting to note that if 2 or 10 consecutive eigenmodes are superposed to construct a 3D medium, the scattered spectral density from such medium satisfies a non-Gaussian profile, exhibiting deviations in large scattering-angle regions. By contrast, if sufficiently many modes, e.g., 100, are superposed for constructing the medium, the scattered intensity gradually

converges to the Gaussian profile, being the same as that scattered from the GSM medium, despite only a few side lobes emerging in the large scattering-angle regions. This result indicates that one can use a certain large number of deterministic modes to approximately model a 3D random medium.

In summary, we have introduced the DMR of a stationary 3D random medium and applied it to the case of weak scattering in the far field. The DMR is developed in analogy with the coherent mode decomposition of stationary optical fields [19-20] and can be adopted for modeling of correlation functions of scattering potentials of various media. As an example, we have determined the modal structure of the GSM medium. The deterministic modes of a GSM medium can be regarded as the 3D generalizations of classic Hermite-Gaussian laser resonator modes.

2.2 Scattering of Light from a Non-uniformly Correlated Medium

In recent decades, non-Gaussian models for representing a variety of media's correlation functions have been introduced to predict unique properties of scattered fields. As representative examples, two spherically symmetric correlation functions [31] are capable to produce flat- and ring-like far-field scattered intensity profiles, and the model in [32] can lead to square or rectangular patterns. The directionality control of the scattered field can be realized by appropriately choosing incident beam properties. For instance, it has been shown that a Bessel-correlated beam incident upon a hard sphere can produce a cone-like scattered profile with no forward scattering [33-35]. In all these literatures, the average refractive index (scattering potential) distribution can be arbitrary since the far-zone intensity is only influenced by the medium's degree of correlation. Moreover, the

analytic models proposed in [31-32] indicate that the distributions and widths of the medium's degree of correlation were chosen to be uniform in the medium's volume.

In this section, we will introduce an analytic model for representing a 3D scattering potential of whose typical width depends on position within the scattered volume. We name such a model medium as Non-Uniformly Correlated (NUC). The original idea of spatially varying correlations in linear and planar radiating sources was introduced [19, 36] and further developed in [37-39].

2.2.1 Far-zone Scattered Field Properties

To model such a random medium, we must notice that any correlation function must obey realizability conditions including non-negative definiteness, Hermiticity and square integrability [17]. Based upon these necessary conditions, we can represent the second-order correlation function of a NUC medium as [40]

$$\begin{aligned} C_F\left(\boldsymbol{r}_1',\boldsymbol{r}_2';\omega\right) &= \left\langle F^*\left(\boldsymbol{r}_1';\omega\right)F\left(\boldsymbol{r}_2';\omega\right)\right\rangle \\ &= \int p\left(\boldsymbol{v}\right)H_0^*\left(\boldsymbol{r}_1',\boldsymbol{v};\omega\right)H_0\left(\boldsymbol{r}_2',\boldsymbol{v};\omega\right)d^3v, \end{aligned} \tag{2.30}$$

where $\boldsymbol{r}_1'$ and $\boldsymbol{r}_2'$ are 3D position vectors in the scatterer's volume, ω is angular frequency, the asterisk denotes complex conjugate, $F(\boldsymbol{r}'; \omega)$ is the scattering potential, H_0 is arbitrary mode function, i.e.,

$$H_0\left(\boldsymbol{r}',\boldsymbol{v};\omega\right) = Q\left(\boldsymbol{r}';\omega\right)\exp\left[-if\left(\boldsymbol{r}'\right)\cdot\boldsymbol{v}\right], \tag{2.31}$$

where Q is a complex function that evaluates the potential amplitude, being generally assumed to be Gaussian. We substitute Eq. (2.31) into Eq. (2.30) and further suppose that functions $p(\boldsymbol{v})$ and H_0 have the following formulations

$$p\left(\boldsymbol{v}\right) = \left(\pi a\right)^{-3/2}\exp\left(-v^2/a^2\right), \tag{2.32}$$

$$H_0(\boldsymbol{r}';\omega)=\exp\left(-\frac{r'^2}{2\delta_0^2}-ik\left[(x'-x_0)^2+(y'-y_0)^2+(z'-z_0)^2\right]v\right), \tag{2.33}$$

where a and δ_0 are real, positive constants, $r_0=(x_0, y_0, z_0)$ is a position with respect to the maximum degree of correlation. Substituting from Eqs. (2.32) and (2.33) into (2.30) implies that the correlation function of the NUC medium becomes

$$C_F(\boldsymbol{r}_1',\boldsymbol{r}_2';\omega)=\exp\left(-\frac{r_1'^2+r_2'^2}{2\delta_0^2}\right)\prod_{j'=x,y,z}\exp\left\{-\frac{\left[(j_2'-j_0)^2+(j_1'-j_0)^2\right]^2}{\delta_c^4}\right\}, \tag{2.34}$$

where $\delta_c=\sqrt{2/ka}$ is the correlation width of the medium. To further analyze the scattered field properties, we express the CSD function in the far-zone via volume integral [17]

$$\begin{aligned}W^{(s)}(r\boldsymbol{s}_1,r\boldsymbol{s}_2;\omega)=&\int_V W^{(i)}(\boldsymbol{r}_1',\boldsymbol{r}_2';\omega)C_F(\boldsymbol{r}_1',\boldsymbol{r}_2';\omega)\\&\times G^*(r\boldsymbol{s}_1,\boldsymbol{r}_1';\omega)G(r\boldsymbol{s}_2,\boldsymbol{r}_2';\omega)d^3r',\end{aligned} \tag{2.35}$$

where integration is performed over the 3D medium volume, G is the Green's function, $\boldsymbol{s}_1$ and $\boldsymbol{s}_2$ are unit vectors of the scattered field. In our study we only concerned with the far-zone scattered field, so that the scattered spectral density (intensity) takes the following expression

$$\begin{aligned}S^{(s)}(r\boldsymbol{s};\omega)=&\frac{32\pi^{5/2}}{a^3r^2}S^{(i)}(\omega)\int_0^\infty\frac{\delta_0^6v^2}{\left[4k^2\delta_0^4v^2+1\right]^{3/2}}\exp\left\{-\frac{v^2}{a^2}-\frac{k^2\delta_0^2}{4k^2\delta_0^4v^2+1}\left[(2vx_0-s_x)^2\right.\right.\\&\left.\left.+(2vy_0-s_y)^2+(2vz_0-s_z+1)^2\right]\right\}dv.\end{aligned} \tag{2.36}$$

It follows from Eq. (2.36) that the far-zone spectral density of the scattered field has neither symmetric nor Gaussian distribution due to the UNC medium effects.

2.2.2 Dependence of Scattered Spectral Densities on Shift of Medium Correlation

We now concentrate on the effects induced by weak scattering of a plane wave from the NUC medium on the spectral density in the far field. Fig. 2.5 is the schematic diagram showing the scattering of a plane wave from a 3D medium. The scattering (azimuthal) angle θ and polar angle ϕ are also marked in the diagram, respectively, "$\perp$" indicates the projective line of the green scattering ray onto the X-Y plane, and "O" represents the origin within the 3D medium.

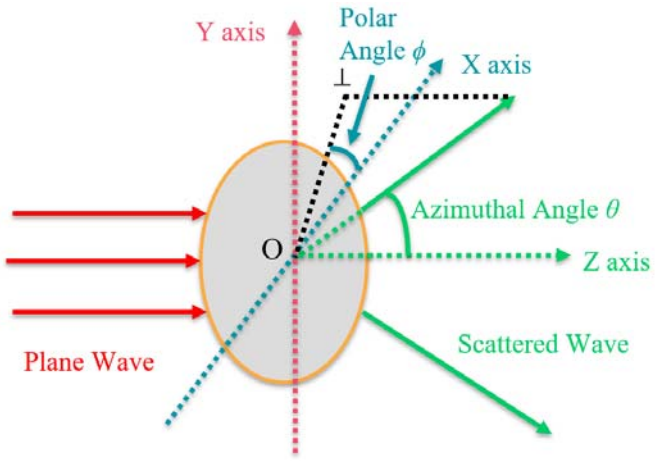

Fig. 2.5 Schematic diagram of the scattering geometry showing plane wave scattering from a 3D medium.

Fig. 2.6 shows that increasing the shift of the correlation center, results in deviation of the peak positions of the scattered spectral densities from the scattering axis. A further increase also leads to the emergence of the sidelobes. When the shift of the correlation center attains a sufficiently large value, i.e., $\Delta x=40\lambda$, the scattered patterns contain sidelobes that have considerable intensity values. According to the reciprocal relations of

light scattering from a quasi-homogeneous random medium, far-zone scattered spectral densities should depend of medium's degree of correlation [18, 41]. Our result extends these relations to cases when the medium is not quasi-homogenous.

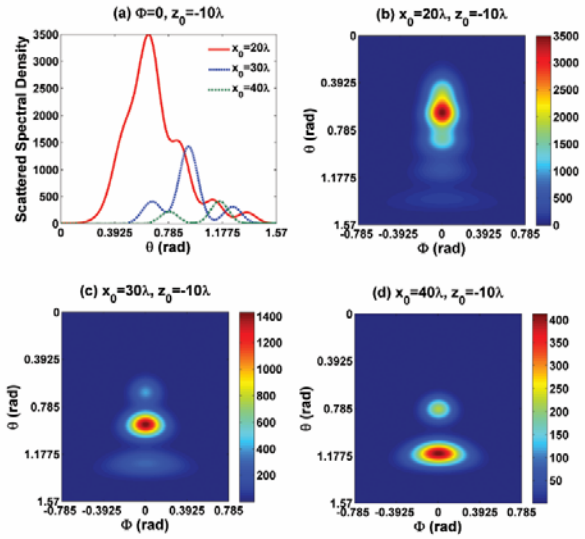

Fig. 2.6 Scattered intensity profiles with sidelobes beyond focused patterns. The correlation width is chosen as δ_c/δ_0=1. (a) ϕ=0, z_0=-10λ. (b), (c), and (d) are the contour plots of scattered intensities corresponding to solid, dashed-dotted, and dashed curves of (a), respectively (from Fig. 3 of [40]).

Fig. 2.7 exhibits the effect of the shift of correlation center in the x-y plane on the azimuthal (scattering) angle θ_{max}. The dependence of correlation strength δ_c/δ_0 on θ_{max} is also shown in the figure. For all plotted curves the x-axis distribution is shown using logarithmic scale. As two extreme cases, δ_c/δ_0=1 indicates that the correlation strength is moderate, while δ_c/δ_0=5 corresponds to the case where the correlation strength is high. Figs. 2.7(a)-(b) illustrate that a larger shift of correlation center on the x-y plane gives rise to a larger θ_{max}, implying that scattered peaks can be generated at a larger azimuthal

scattering angle. Furthermore, the azimuthal angle of the peak intensity finally approaches a constant value. Another essential result implied from Fig. 2.7 is that a NUC medium with stronger correlation leads to the scattered field with larger spreading of intensity off the scattering axis. It can be summarized that the positions of the maximum scattered intensity depend on two key factors: δ_c/δ_0 and the shift of correlation center of the medium.

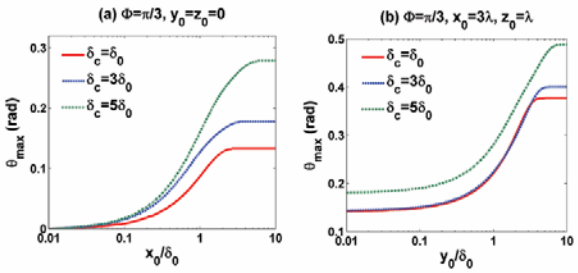

Fig. 2.7 Effect of the correlation center shift and δ_c/δ_0 on the azimuthal angle of the peak scattered intensity. The polar angle is chosen as $\phi=\pi/3$. (a) Effect of the shift along the x axis, $y_0=z_0=0$. (b) Effect of the shift along the y axis, $x_0=3\lambda$, $z_0=\lambda$ (from Fig. 4 of [40]).

2.2.3 Concluding Remarks

In summary, we introduced a mathematical model for characterizing a class of mediua whose degree of correlation obeys the non-uniform profile in the 3D Cartesian coordinates. Such medium type can concentrate the spectral density on or off the scattering axis. We have found that the peak positions of the spectral density scattered from such a medium can be flexibly adjusted by shifting the maximum degree of correlation off the medium's origin centroid. By introducing shifts of the correlation center along a certain axis, 1D sidelobes can be produced. These results are applicable for flexible control of peak scattered intensity on or off the scattering axis and are beneficial to solving the inverse scattering problems where more than one homogeneous medium is

involved. Such situation frequently happens in medical diagnostics when light scatters from bio-tissues containing normal and malignant components [42].

2.3 Modeling of a Statistically Stationary Medium for Cusping of Plane Waves

In recent decades numerous approaches have been introduced to produce cusp-like light intensity profiles, for example, tight focusing of laser beams by high numerical aperture (NA) [43-46], their propagation in double-pass turbulent channel [21], modeling of correlations of random sources [23-25, 47], and bending control of solitons in nonlinear localized media [48-49]. Besides, it has been well known that random stationary media can scatter plane waves to far-field distributions which have tunable shape and size. The typical Gaussian Schell-model medium and the Gaussian quasi-homogeneous medium can scatter incident plane waves into Gaussian intensity distributions which have controllable r.m.s. widths [3]. Recently, a couple of random media models have been introduced for scattering of a plane wave to a specific profile, e.g., flat-topped or ring-like profiles [24-26], rectangles [50], producing intensity maxima off the scattering axis [31], optical frames, cages and azimuthally varying intensity distributions [51].

In this section, we will introduce a scattering medium model, namely the Fractional Multi-Gaussian Schell-model (FMGSM) scattering medium which can produce a sharply peaked intensity in the central region of the far field. Compared with the GSM medium, the FMGSM medium has more advantages to produce a much narrower and stronger spectral density apex in the far-zone of the scattered field.

2.3.1 Fractional Multi-Gaussian Correlation Function

We first introduce the analytical model for characterizing a 3D Schell-model medium whose degree of correlation obeys the FMG distribution with spherical symmetry. To model such a medium, we first recall that any correlation function of a 3D medium must satisfy one of the realizability conditions, i.e., the non-negative definiteness. Following definitions in [27-29] but further generalizing the results from 1D and 2D to 3D case, we show that any genuine, second-order correlation function of the FMGSM medium at position vectors $\boldsymbol{r}_1'$ and $\boldsymbol{r}_2'$ must have integral representation (see Eq. (1) of [31, 52])

$$\begin{aligned} C_F\left(\boldsymbol{r}_1',\boldsymbol{r}_2';\omega\right) &= \left\langle F^*\left(\boldsymbol{r}_1';\omega\right)F\left(\boldsymbol{r}_2';\omega\right)\right\rangle \\ &= \int p\left(\boldsymbol{v}\right)H_0^*\left(\boldsymbol{r}_1',\boldsymbol{v};\omega\right)H_0\left(\boldsymbol{r}_2',\boldsymbol{v};\omega\right)d^3v. \end{aligned} \tag{2.37}$$

For a typical Schell-like model medium, H_0 in Eq. (2.37) must have the Fourier-type profile

$$H_0\left(\boldsymbol{r}',\boldsymbol{v};\omega\right) = Q\left(\boldsymbol{r}';\omega\right)\exp\left(-i\boldsymbol{r}'\cdot\boldsymbol{v}\right), \tag{2.38}$$

where Q is generally a complex-valued function which determines the scattering potential amplitude. For simplicity, we assume that the strength of the scattering potential too satisfies Gaussian distribution, so that H_0 can be represented as

$$H_0\left(\boldsymbol{r}',\boldsymbol{v},\omega\right) = \exp\left(-\frac{r'^2}{2\sigma_s^2} - ik\boldsymbol{r}'\cdot\boldsymbol{v}\right), \tag{2.39}$$

where σ_s is the effective width that may be dependent of frequency. To model the 3D FMGSM medium, we assume that $p(v)$ takes form of the spherical FMG function

$$\begin{aligned} p\left(v\right) &= 1-\left[1-\exp\left(-\delta_s^2v^2/2\right)\right]^{1/M} \\ &= \sum_{n=1}^{\infty}\frac{\left(-1\right)^n\prod_{m=1}^{n}\left[1-\left(m-1\right)M\right]}{}\exp\left(-n\delta_s^2v^2/2\right). \end{aligned} \tag{2.40}$$

Here the fractional binomial mathematics was applied for deducing the expansion coefficients. When M=1, the classic Gaussian Schell-model medium can be obtained. Consequently, the degree of correlation of the FMGSM medium can be derived as (see Eq. (10) of [52] for detailed information)

$$\mu\left(\boldsymbol{r}_2'-\boldsymbol{r}_1';\omega\right)=\sum_{n=1}^{\infty}\frac{(-1)^{n+1}\prod_{m=1}^{n}\left[1-(m-1)M\right]}{L_0(M)\left(n\sqrt{n}\right)n!M^n}\exp\left[-\frac{\left(\boldsymbol{r}_2'-\boldsymbol{r}_1'\right)^2}{2n\delta_s^2}\right], \tag{2.41}$$

where

$$L_0(M)=\sum_{n=1}^{\infty}\frac{(-1)^{n+1}\prod_{m=1}^{n}\left[1-(m-1)M\right]}{\left(n\sqrt{n}\right)n!M^n}, \tag{2.42}$$

is the normalization coefficient.

2.3.2 Far-zone Scattered Intensity from 3D FMGSM Medium

Based upon Eqs. (2.40)-(2.42) the far-zone scattered spectral density scattered from the FMGSM medium becomes

$$S^{(s)}(r\boldsymbol{s};\omega)=\frac{S^{(i)}(\omega)}{r^2}\int p(\boldsymbol{v})\left|H_s(\boldsymbol{K},\boldsymbol{v})\right|^2 d^3v, \tag{2.43}$$

where $\left|H_s(\boldsymbol{K},\boldsymbol{v})\right|$ is calculated from the formula

$$\left|H_s(\boldsymbol{K},v)\right|^2=\left(2\pi\sigma_s^2\right)^3\exp\left[-\sigma_s^2\left|K\right|^2-\sigma_s^2\left(v^2+2\boldsymbol{K}\cdot\boldsymbol{v}\right)\right]. \tag{2.44}$$

To further compare the spectral density scattered from the FMGSM medium with that scattered from the GSM medium, the following normalized formulations of $p(v)$ can be chosen for representing two types of media

$$p_N^{(FMGSM)}(v)=\sum_{n=1}^{\infty}\frac{(-1)^{n}\prod_{m=1}^{n}\left[1-(m-1)M\right]}{C_0(M)n!M^n}\exp\left(-n\delta_s^2v^2/2\right), \tag{2.45}$$

$$p_N^{(GSM)}(v)=\exp\left(-\delta_s^2 v^2/2\right), \tag{2.46}$$

where $C_0(M)$ is the normalization coefficient which is defined as

$$C_0(M)=\sum_{n=1}^{\infty}\frac{(-1)^n\prod_{m=1}^{n}\left[1-(m-1)M\right]}{n!M^n}. \tag{2.47}$$

It is found that the scattered spectral density from the FMGSM medium can be formulated as

$$\begin{aligned}S_{FMGSM}^{(s)}(r,\theta;\omega)=&\frac{S^{(i)}(\omega)}{C_0(M)r^2}\sum_{n=1}^{\infty}\frac{(-1)^n\prod_{m=1}^{n}\left[1-(m-1)M\right]}{n!M^n}\\&\times\left(\frac{4\pi^3\sigma_s^4}{\sigma_s^2+n\delta_s^2/2}\right)^{3/2}\exp\left[-\frac{2nk^2\sigma_s^2\delta_s^2}{\sigma_s^2+n\delta_s^2/2}\sin^2\left(\frac{\theta}{2}\right)\right],\end{aligned} \tag{2.48}$$

where $\theta=\arccos(\boldsymbol{s}\cdot\boldsymbol{s}_0)$ is the scattering angle. For comparison, the spectral density scattered from the GSM medium is given by expression

$$S_{GSM}^{(s)}(r,\theta;\omega)=\frac{S^{(i)}(\omega)}{r^2}\left(\frac{4\pi^3\sigma_s^4}{\sigma_s^2+\delta_s^2/2}\right)^{3/2}\exp\left[-\frac{2k^2\sigma_s^2\delta_s^2}{\sigma_s^2+\delta_s^2/2}\sin^2(\theta/2)\right]. \tag{2.49}$$

Eqs. (2.48) and (2.49) can be used to investigate the scattered intensity profiles from two types of media, as shown by Figs. 2.9 and 2.10. In what follows, numerical calculations are performed and the parameters are fixed as σ_s=50λ, δ_s=5λ, unless stated elsewhere.

2.3.3 Examples and Concluding Remarks

Fig. 2.8 illustrates that the intensity distribution of a plane wave scattered from the FMGSM medium is narrower than that scattered from the GSM medium, being very distinct in profile when mode number M is greater than 2. This is due to the fact the degree of correlation of the medium has larger width than that of the GSM medium, even though they have the same correlation length. If M is sufficiently large, e.g., M=20, the

peak intensity value corresponding to the FMGSM medium is almost twice as large as that produced by the GSM medium.

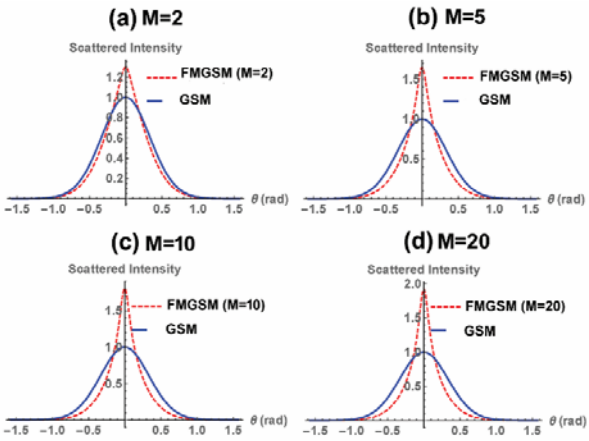

Fig. 2.8 Scattered intensity profiles from the FMGSM medium versus the scattering angle θ (dashed curves). The medium's correlation length $\delta_s=5\lambda$. For comparisons, the solid curves are for the scattered intensities from the GSM medium with the same correlation length. (a) M=2, (b) M=5, (c) M=10, (d) M=20 (from Fig. 2 of [52]).

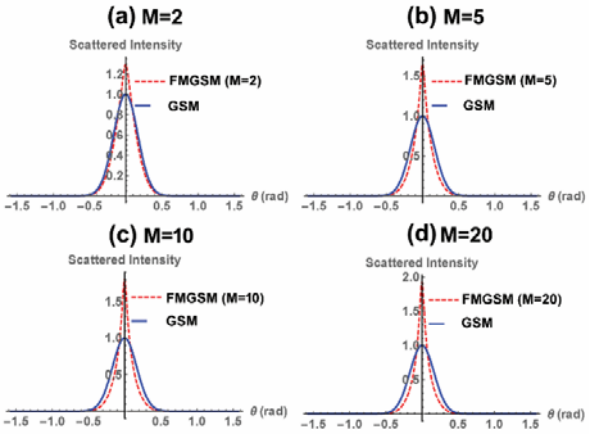

Fig. 2.9 Scattered intensity profiles from the FMGSM (dashed curves) and GSM medium (solid curves). The numerical parameters are the same as those used in Fig. 2.8 except a larger correlation length is chosen, i.e., $\delta_s=10\lambda$. (a) M=2, (b) M=5, (c) M=10, (d) M=20 (from Fig. 3 of [52]).

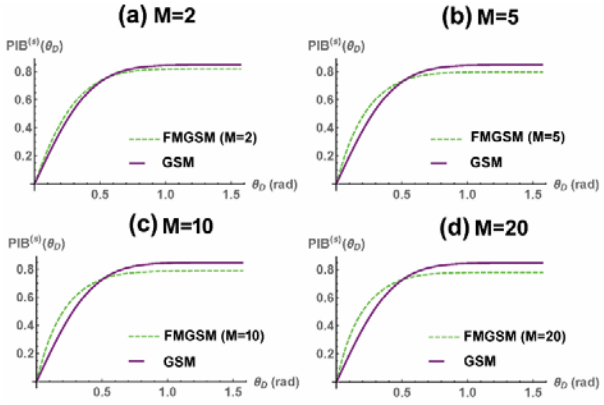

Fig. 2.10 Power-in-bucket (PIB) versus the half-aperture angle (HAA) of a detector in the scattered field. The dashed and solid curves are for the PIB scattered from the FMGSM and GSM media, respectively. The two media share the same correlation length $\delta_s=5\lambda$. (a) M=2, (b) M=5, (c) M=10, (d) M=20 (from Fig. 4 of [52]).

In Fig. 2.9 the correlation length $\delta_s=10\lambda$ of the medium is chosen for calculations. Compared with Fig. 2.8, it is shown that the FMGSM medium having a larger degree of correlation can generate the scattered intensity with narrower distribution. In addition, the discrepancy between the scattered intensities produced by two types of media become more distinct for increased values of M.

Fig. 2.10 displays the Power-In-Bucket (PIB) of the scattered power entering a circular detector which collects a portion of the total scattered power in the far field. The PIBs of the scattered field from two types of media can be analytically derived from Eqs. (2.33) and (2.34) by integrating over the scattering angle region ($-\theta_D/2$, $\theta_D/2$), where θ_D is the half-aperture angle (HAA) of the detector. For a certain value of HAA the PIBs scattered from two types of media show different characteristics. Compared with the GSM medium, the FMGSM medium gives rise to a larger PIB if the HAA is sufficiently

small, e.g., $\theta_D << 0.5\ rad$. However, if θ_D achieves a certain large value, e.g., $\theta_D = 0.5 rad$, the PIBs scattered from both media have the equivalent value denoted by the cross point in Fig. 2.10. By further increasing θ_D, the PIB scattered from the GSM medium exceeds that scattered from the FMGSM medium. These results coincide with those shown in Fig. 2.8.

In summary, we have introduced a 3D model of weakly random, statistically stationary medium whose degree of correlation obeys a FMG function. We find that such medium can produce a strongly focused intensity profile along the scattering axis. Compared with the GSM medium, the FMGSM medium gives rise to the scattered intensity which has a much sharper and higher peak maximum. The PIBs received by a detector in the far-zone scattered field are compared between the FMGSM and GSM cases. For small HAA values, the FMGSM medium produces larger PIB value in the central scattered region, therefore it can be used in applications where strongly localized light must be generated.

Chapter 3

Tuning the Observable Properties of Stationary Light Beams by Structuring Correlations in Their Sources

3.1 Partially Coherent Random Sources for Cusped Beams

During the last several decades, partially coherent beams with particularly designed correlation functions have attracted great interest owing to their unique features while they propagate in free space, pass through optical systems and interact with various deterministic and random media [3, 17]. It became apparent that partially coherent beams can show interesting phenomena upon free-space propagation, for instance, forming flat-topped intensity profiles, multi-ring distributions, exhibit self-focusing effect as well as lateral peak shift, to name a few. These remarkable beam properties are very essential for beam shaping, laser communications and particle guiding.

Up to now, the only issue that has not been completely addressed so far is the mathematical modeling of random sources that can produce beams with narrower spectral density distributions if compared with Gaussian. Experimental solution to this issue has been recently introduced by using the super-Gaussian function to model far-field spectral density [53]. However, the analytical expressions for modeling of source degree of coherence (DOC) are cumbersome. In this section, we intend to propose two analytical source DOC models that can produce strongly peaked far-field spectral densities on the scattering axis. Two beam types are introduced to have the degrees of coherence characterized by the rectangular Lorentz-correlated Schell-model (LSM) and rectangular Fractional Multi-Gaussian-correlated Schell-model (FMGSM) functions, respectively. We show that the two beams can produce highly focused intensity distributions when

they propagate to a far field or to the focal plane of a thin lens. The experimental synthesis of two beams is achieved by using a transmissive Spatial Light Modulator (SLM).

3.1.1 Lorentz-correlated Schell-model Source

First, let us introduce the theoretical model for the source and further analyze its radiated beam propagating through a stigmatic *ABCD* optical system. It is assumed that $p(v)$ of such a source should be the non-negative exponential function (see Eq. (6) of [47])

$$p(\boldsymbol{v}) = \pi\delta^2 \exp\left[-2\pi\delta\left(|v_x| + |v_y|\right)\right], \tag{3.1}$$

and, hence, the DOC of such a source takes form

$$\mu(x_d, y_d) = \frac{\delta^4}{\left(x_d^2 + \delta^2\right)\left(y_d^2 + \delta^2\right)}, \tag{3.2}$$

where $x_d = x_2' - x_1'$, $y_d = y_2' - y_1$, and $\mu(0, 0)=1$ should be valid at two coinciding arguments. Let us term δ appearing in Eqs. (3.1) and (3.2) the source coherence length. Fig. 3.1 shows the DOC of the rectangular LSM source for three different coherence lengths, i.e. δ=0.1mm, 1mm, and 2mm. It is found that the DOC distribution becomes wider when the coherence length increases. For a sufficiently small coherence length, for example δ=0.1mm, the DOC shows as a cusped profile, as denoted by the solid curve in Fig. 3.1(d). If we further assume that the LSM source has the Gaussian intensity distribution, then its CSD function has the following expression

$$W^{(0)}(\boldsymbol{\rho}_1', \boldsymbol{\rho}_2') = \exp\left(-\frac{\rho_1^2 + \rho_2^2}{4\sigma_0^2}\right)\frac{\delta^4}{\left[\left(x_2 - x_1\right)^2 + \delta^2\right]\left[\left(y_2 - y_1\right)^2 + \delta^2\right]}. \tag{3.3}$$

By performing tedious but straightforward integrations, the resultant spectral density of the beam propagating through an *ABCD* optical system shows the analytic form [47]

$$I(\boldsymbol{\rho},z)=\frac{\pi^3k^2\delta^2\sigma_0^2}{2B^2}\exp\left(Q\delta^2\right)\left\{\exp\left(-\frac{k\delta}{B}x\right)erfc\left\{\sqrt{\frac{1}{2}Q}\left[\delta-\frac{kx}{BQ}\right]\right\}\right\}$$
$$+\exp\left(\frac{k\delta}{B}x\right)erfc\left\{\sqrt{\frac{1}{2}Q}\left[\delta+\frac{kx}{BQ}\right]\right\}\left\{\exp\left(-\frac{k\delta}{B}y\right)erfc\left\{\sqrt{\frac{1}{2}Q}\left[\delta-\frac{ky}{BQ}\right]\right\}\right. \quad (3.4)$$
$$\left.+\exp\left(\frac{k\delta}{B}y\right)erfc\left\{\sqrt{\frac{1}{2}Q}\left[\delta+\frac{ky}{BQ}\right]\right\}\right\},$$

where

$$Q=\frac{k^2A^2}{B^2}\sigma_0^2+\frac{1}{4\sigma_0^2}, \quad (3.5)$$

and

$$erfc(u)=1-\frac{2}{\sqrt{\pi}}\int_0^u\exp\left(-t^2\right)dt, \quad (3.6)$$

is the error function.

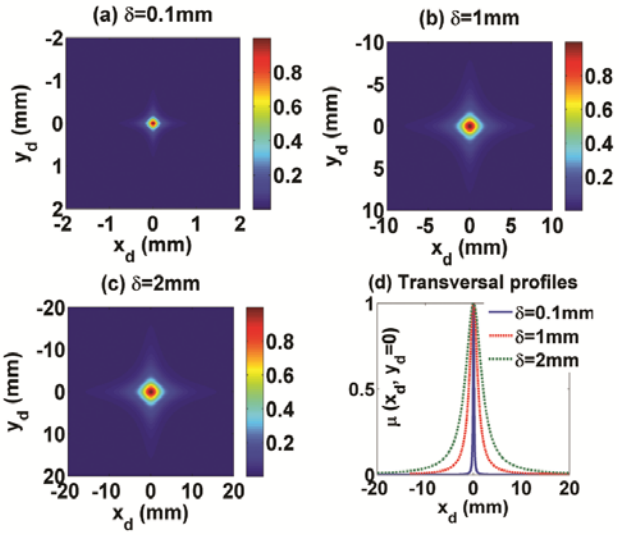

Fig. 3.1 Density plots of the intensity distributions of the LSM source in the focal plane with different coherence lengths. (a) δ=0.1mm, (b) δ=0.5mm, (c) δ=1mm, (d) δ=2mm (from Fig. 1 of [47]).

Fig. 3.1 illustrates the intensity distributions of the propagating beam radiated from the LSM source at the focal plane $z=f$. It is noteworthy that the propagating beam retains the rectangular profile if its coherence length is sufficiently small, e.g., δ=0.1mm. However, its profile gradually gets lost and eventually converts to a circular Gaussian distribution when its coherence length approaches certain magnitude, e.g., δ=2mm. Recalling the reciprocity relations for partially coherent beams, the propagating intensity should be strongly dependent on the source DOC. Because the source produces a strongly focused intensity peak in the focal plane, we can classify the LSM as a typical source which is capable to produce focused partially coherent beam in far field.

3.1.2 Fractional Multi-Gaussian-correlated Schell-model Source

In this section we introduce another class of a random source which can also produce a strongly focused intensity peak when the radiated beam propagates to the far field or focal plane of a thin lens. To model such a source we should first assume that the corresponding $p(\boldsymbol{v})$ takes the form of the rectangular FMGSM function [47, 54]

$$p(\boldsymbol{v})=\left\{1-\left[1-\exp\left(-2\pi^2\delta^2 v_x^2\right)\right]^{1/M}\right\}\cdot\left\{1-\left[1-\exp\left(-2\pi^2\delta^2 v_y^2\right)\right]^{1/M}\right\}, \tag{3.7}$$

where δ has been interpreted in Eq. (3.1), M is a non-negative integer. The DOC of such a source can be derived by performing the Fourier transform of $p(\boldsymbol{v})$ in Eq. (3.7), i.e.,

$$\begin{aligned}\mu(x_d,y_d)=\frac{1}{C_0}&\left\{\sum_{n=1}^{\infty}\frac{(-1)^{n+1}\prod_{m=1}^{n}\left[1-(m-1)M\right]}{\sqrt{n}n!M^n}\exp\left(-\frac{x_d^2}{2n\delta^2}\right)\right\}\\&\times\left\{\sum_{n'=1}^{\infty}\frac{(-1)^{n'+1}\prod_{m'=1}^{n'}\left[1-(m'-1)M\right]}{\sqrt{n'}n!M^{n'}}\exp\left(-\frac{y_d^2}{2n'\delta^2}\right)\right\},\end{aligned} \tag{3.8}$$

where

$$C_0=\sum_{n=1}^{\infty}\frac{(-1)^n\prod_{m=1}^{n}\left[1-(m-1)M\right]}{\sqrt{n}n!M^n}, \tag{3.9}$$

is the normalization coefficient. The intensity distribution of the beam radiated from such a source propagating through an *ABCD* optical system becomes

$$\begin{aligned} I(x,y,z)=\frac{1}{C_0^2}&\left\{\sum_{n=1}^{\infty}\frac{(-1)^{n+1}\prod_{m=1}^{n}\left[1-(m-1)M\right]}{\sqrt{n}n!M^n}\exp\left(-\frac{x^2}{2\sigma_0^2Q'}\right)\right\}\\ &\times\left\{\sum_{n'=1}^{\infty}\frac{(-1)^{n'+1}\prod_{m'=1}^{n'}\left[1-(m'-1)M\right]}{\sqrt{n'}n'!\ M^{n'}}\exp\left(-\frac{y^2}{2\sigma_0^2Q'}\right)\right\}, \end{aligned} \tag{3.10}$$

where

$$Q'=A^2+\frac{B^2}{4k^2\sigma_0^4}+\frac{B^2}{nk^2\sigma_0^2\delta^2}. \tag{3.11}$$

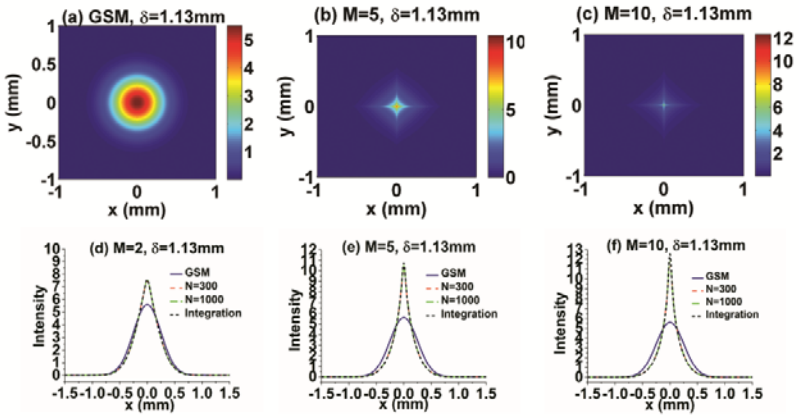

Fig. 3.2 Spectral density of the FMGSM beam at the focal plane. The density plot (a) shows the focused intensity produced by the GSM beam, (b)-(c) show the focused intensity of the FMGSM beam for *M*=5 and 10, respectively. For comparison, the cross-section profiles (d)-(f) show the intensity distributions for *M*=2, 5, 10 and the GSM beam, respectively. As the numerical parameter, the coherence length remains a fixed value δ=1.13mm (from Fig. 5 of [47]).

Based on Eqs. (3.10) and (3.11), the spectral density of the beam radiated from the FMGSM source and propagating through a thin lens in the focal plane can be found. We observing from Fig. 3.2 that the FMGSM source has advantages for producing a narrower intensity profile in the focal plane. By increasing the values of M the intensity peak value can be substantially increased. For M=10 the focused beam pattern looks like a "needle" apex in the central region. Furthermore, the peak intensity of the FMGSM beam in the focal plane of a thin lens is much larger than that produced by the GSM source beam. This comparative result indicates that the FMGSM source can be regarded as a better candidate than the GSM source for producing strongly focused intensity in far field of optical systems.

3.1.3 Experimental Generation of Highly Focused Partially Coherent Beams

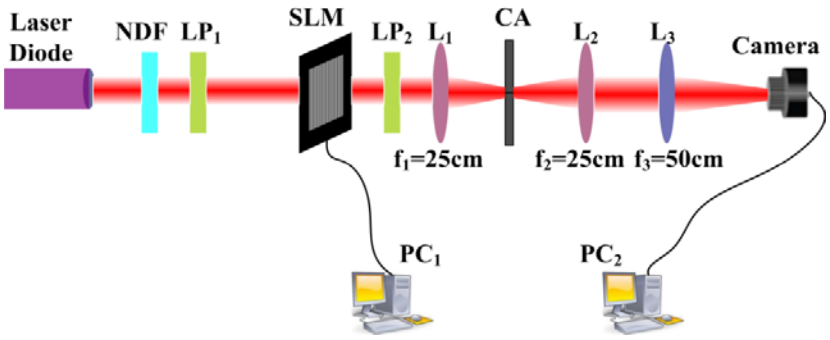

Fig. 3.3 Experimental setup for generating the LSM and the FMGSM beams and measuring their focused intensity distributions. NDF: neutral density filter; LP_1 and LP_2: linear polarizers; CA: circular apertures; SLM: spatial light modulator; L_1, L_2 and L_3: thin lens; PC_1 and PC_2: personal computers (from Fig. 6 of [47]).

Fig. 3.3 illustrates the schematic diagram for generating the two beams by experimental setup. The laser beam emitted from a laser diode (LD, λ=532nm) first passes through a neutral density filter (NDF), and then the resultant beam transmits through a linear polarizer (LP). The transmitted beam from LP_1 subsequently passes through a spatial light modulator (SLM, HOLOEYE LC2012) controlled by a personal computer (PC_1), behaving as a random phase screen for generation of the LSM or the FMGSM source beam. The synthesis methods of random phase screens can be indexed in [53, 55-58]. The second linear polarizer (LP_2) whose the optical axis coincides with LP_1 is placed behind the SLM to block the intensity contributed by other polarization components appeared from the scattering from the SLM. Lenses L_1 and L_2 constitute a 2*f*-imaging system, each having the same focal length *f*=250mm, and a circular aperture (CA) is used to filter out the first-order diffraction order from SLM grating. The lens L_3 is inserted after L_2 to further focus the generated beam. In the focal plane, a CMOS detector (DCC1545M-GL) is placed to capture the focused intensity and further export the experimental data to the personal computer (PC_2).

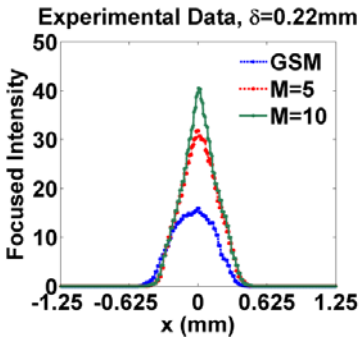

Fig. 3.4 Experimental intensity distributions of the focused FMGSM beam at the cross-section *y*=0. Comparisons are made between the focused intensities of the FMGSM beam with *M*=5, 10 and those produced by the GSM beam (from Fig. 9 of [47]).

The focused intensity distributions of the FMGSM beam and those of the GSM source beam are compared in Fig. 3.4. It is found that the focused intensity profile of the FMGSM beam has narrower width, and its intensity peak is much higher than that produced by the GSM beam which has the same coherence length. In addition, Fig. 3.4 also shows a good agreement with the theoretical results presented in Figs. 3.2(e)-(f). The remarkable self-focusing ability of the FMGSM source beam implies that this beam is a better candidate than the GSM beam for some applications, e.g., the material thermal process and beam shaping in the focal plane.

3.1.4 Concluding Remarks

In summary, we introduce two partially coherent sources whose spectral DOCs obey the rectangular Lorentz and the Fractional Multi-Gaussian functions, respectively. Propagation properties of two beam families through a stigmatic *ABCD* optical system are derived analytically. We show that both random beam families can produce strongly focused intensity profiles in the far field or in the focal plane of a thin lens. For the FMGSM beam, the self-focusing intensity distribution looks like a sharp “needle” type. Experimental synthesis of two beams are presented and shown to be consistent with the theoretical calculation results. These two proposed beams, especially the FMGSM beam, can have prospective applications to the material thermal process and beam shaping in the focal plane.

3.2 Partially Coherent Crescent-like Optical Beams

An optical beam which propagates through linear random media such as atmospheric or oceanic turbulence can experience severe phase fluctuations, giving rise to several effects, in addition to the free-space diffraction, scintillations, beam wander, turbulence-induced spread, etc. As a result, the performance of optical systems operating in these types of media becomes limited. An effective approach to mitigate the perturbations originated from these random media is the spatial phase randomization (partial coherence) of the beam at the source [59-60]. For instance, statistical properties of partially coherent Airy beams have been examined on propagation in the atmospheric turbulence, showing that the beam can still radially accelerate up to a certain propagation distance [61]. Another type of beams that exhibit gradual off-axis shifts of their intensity maxima upon free-space propagation utilizes the non-uniform source correlation effect [27]. Being different from the Airy beam, the non-uniformly correlated beams can produce off-axis shifts in its maximum intensity. When they propagate in free space the emerged shifts in intensity maxima can remain invariant at any distance from the source. However, passing through isotropic linear random media the shifted maxima gradually retrieve back to their original on-axis position at sufficiently large propagation distances [29].

In this section, we will introduce a random source that can produce a ring-like profile or a “crescent” distribution around the optical axis, while its intensity maximum is shifted off axis. Such a beam can be generated by a source that has a Gaussian intensity profile and a specifically designed DOC represented by the generalized Laguerre polynomials [62]. Based upon the derived expressions, we perform analysis on the propagation dynamics of the crescent beam in free space and in linear random media

(atmospheric turbulence). We show that the new beam is not the same as the non-uniformly correlated beams, as its maximum intensity position shifts further from the propagation axis when it propagates in free space or turbulence. Furthermore, we also find that the increment of the intensity tilt angle of the beam can be slightly suppressed by turbulence.

3.2.1 Fundamentals of Crescent Random Beam

We start our analysis by introducing the class of random sources which radiates beams having crescent-like spectral density in the far field. Recall that profile function $p(\boldsymbol{v})$ determines the intensity distribution in the far field and, therefore, the correlation function of the source should satisfy the reciprocal relation. In our case, let us assume that $p(\boldsymbol{v})$ is a function separable in polar coordinates, defined as [63]

$$p(\boldsymbol{v}) = \frac{k^2\delta^2(k\delta v)^{2n}}{2^n n!\pi}\exp\left(-\frac{k^2\delta^2 v^2}{2}\right)\cos^2(\theta/2), \tag{3.12}$$

where n is a positive integer, δ denotes the r.m.s of the coherence length, $v = |\boldsymbol{v}|$, θ=arctan(v_y/v_x) denotes the azimuthal angle of vector $\boldsymbol{v}$ in polar coordinate system, respectively. By performing the 2D Fourier transform of Eq. (3.12), it is found that the degree of coherence of the random source takes form [63]

$$\mu(\boldsymbol{r}_d) = L_n^0\left(\frac{r_d^2}{2\delta^2}\right)\exp\left(-\frac{r_d^2}{2\delta^2}\right) - \frac{i\sqrt{2}(n-1/2)!}{2n!}\frac{r_d}{\delta}\exp\left(-\frac{r_d^2}{2\delta^2}\right)L_{n-1/2}^1\left(\frac{r_d^2}{2\delta^2}\right)\cos\varphi_d, \tag{3.13}$$

where L_n^0 represents the generalized Laguerre polynomial with indices n and 0. Here r_d and φ_d are the magnitude and phase of the difference between two position vectors, i.e., $\boldsymbol{r}_d=\boldsymbol{r}_2-\boldsymbol{r}_1$. We need to point out that the DOC shown in Eq. (3.13) is a complex function in the source plane, meaning that the far-field spectral density is not an even function, i.e., it

eventually loses rectangular or circular symmetry. For free-space propagation of the radiated beams, the spectral density of the beam at one position vector $\boldsymbol{\rho}$ results in the following form

$$S(\boldsymbol{\rho},z)=\frac{1}{Q^3}\exp\left(-\frac{\rho^2}{\sigma_0^2 Q_3}\right)\left\{\left(\frac{Q_2}{Q_3}\right)^n L_n^0\left(-\frac{2z^2\rho^2}{k^2\sigma_0^4\delta^2 Q_3 Q_2}\right)\right.$$
$$\left.-\frac{(n-1/2)!}{n!}\frac{\sqrt{2}z\rho}{k\sigma_0^2\delta Q_2}\left(\frac{Q_2}{Q_3}\right)^{n+1/2} L_{n-1/2}^1\left(-\frac{2z^2\rho^2}{k^2\sigma_0^4\delta^2 Q_3 Q_2}\right)\cos\phi\right\}, \tag{3.14}$$

where

$$Q_2=1+\frac{z^2}{k^2\sigma_0^4},\ Q_3=Q_2+2z^2/k^2\sigma_0^2\delta^2, \tag{3.15}$$

and L_n^m is the associated Laguerre polynomial with order n and radial index m, ρ and θ are the radial distance and polar angle corresponding to position vector $\boldsymbol{\rho}$ in the polar coordinate system.

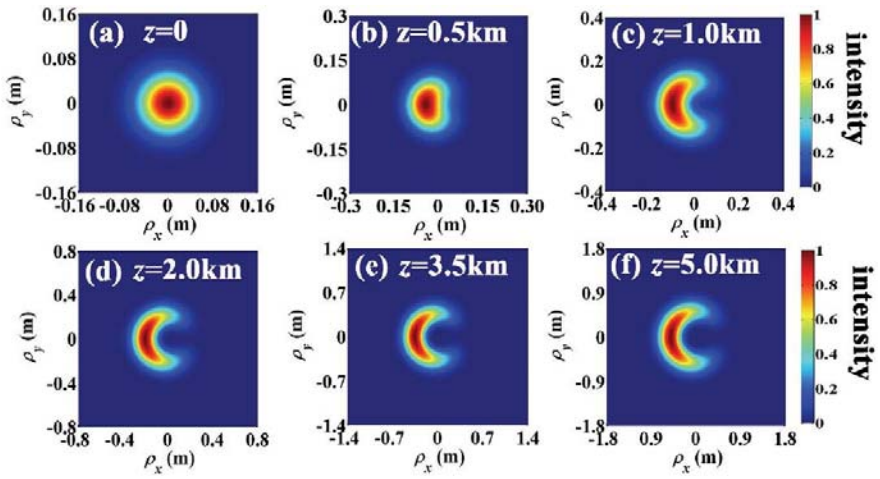

Fig. 3.5 Spectral density of the random beam in free space for several propagation distances (from Fig. 1 of [63]).

Fig. 3.5 shows the spectral density of the random beam at a couple of propagation distances in free space, which are plotted by using Eqs. (3.14) and (3.15). The beam values of source parameters for the plots are chosen as σ_0=50mm, δ=2mm, n=3, λ=532nm, unless is specified elsewhere. Results show that the beam's intensity distribution gradually converts from Gaussian at the source plane to a crescent-like profile due to effects contributed by the specifically tuned correlation function of the source. For sufficiently large propagation distance, the crescent beam retains its far-field shape while its spot size expands due to the diffraction effect.

3.2.2 Synthesis Procedures of Crescent Beam

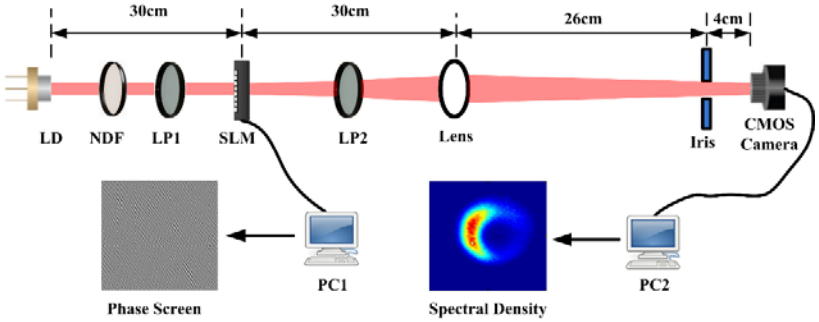

Fig. 3.6 Schematic diagram of the experimental generation of the crescent beam. LD: laser diode; NDF: neutral density filter; SLM: spatial light modulator; LP: linear polarizer. The distances between LD and SLM, SLM and lens, lens and iris are 30cm, 30cm and 26cm, respectively. The CMOS camera is placed 4cm behind the iris to capture instantaneous intensity profile of the crescent beam (from Fig. 2 of [63]).

Generation of the crescent random beam can be realized by setting up the LD source and using the nematic SLM operating in the transmissive mode. The SLM (HOLOEYE LC2012, pixel resolution 1024×768, pixel size: 36μm×36μm) is further connected to

the personal computer 1 (PC_1) which is placed behind the LD (λ=532nm), the NDF and the LP_1. To synthesize the partially coherent crescent random source, a sequence of phase screens whose correlation functions shown by Eq. (3.13) are generated on the computer. The method for generation of the random phase screen with specified correlation statistics were discussed in detailed manner in Refs. [58, 64-66]. Then the sequence of these phase screens is loaded and cycled on the SLM. The frame per second is set up to 50Hz. After transmitting through the SLM the beam further passes through the LP_2, the Lens *L* (focal length 300mm) and the circular iris *I*. The polarizers are utilized to eliminate the LD's and SLM's polarization effects and the iris is adopted to block the unneeded diffraction orders produced from the SLM's grating array. The CMOS camera (Thorlabs, Monochromatic, pixel resolution 1280 × 1024) captures long-time video sequence for obtaining the average intensity distribution of the beam in the focal plane.

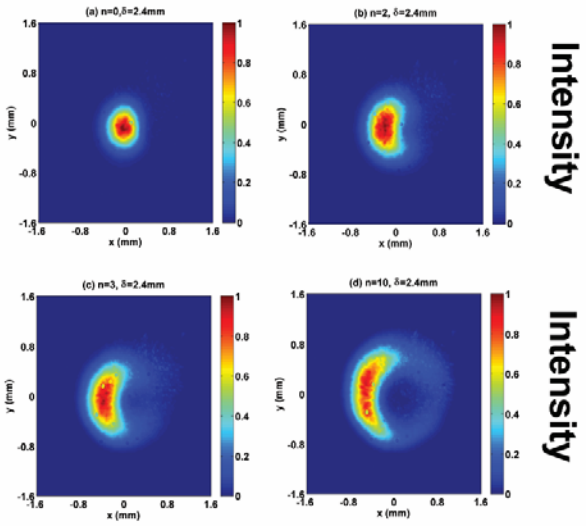

Fig. 3.7 Normalized spectral density profiles of the crescent beam propagating through thin lens (focal length *f*=30cm). The coherence length of the beam is kept uniform as

δ=2.4mm, and the index number are chosen as (a) n=0, (b) n=2, (c) n=3, (d) n=10 (from Fig. 3 of [63]).

Fig. 3.7 exhibits the spectral density distribution of the random beam which has the coherence length δ=2.4mm and the mode index values n=0, 2, 3 and 10, respectively. With the index n increase the crescent beam profile becomes more pronounced, while the intensity maximum position shifts further from the propagation axis. The beam with index n=3 is chosen as optimal since it contains a well-pronounced off-axis shift of maximum intensity. However, its average intensity does not spread too much.

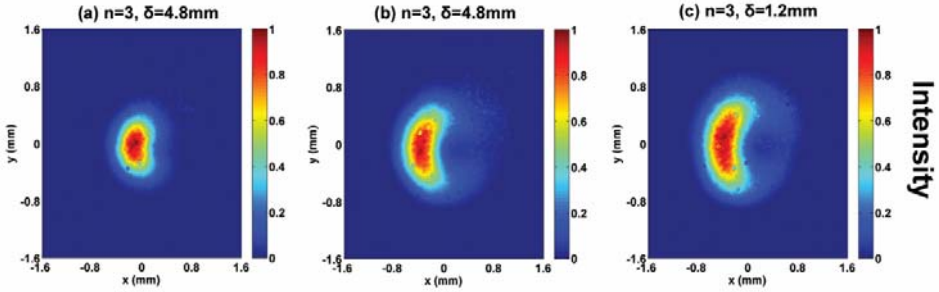

Fig. 3.8 Normalized spectral density profiles of the crescent beam propagating through thin lens (focal length f=30cm). The index number is kept uniform as n=3, and the coherence lengths are chosen as (a) δ=4.8mm, (b) δ=2.4mm, (c) δ=1.2mm (from Fig. 4 of [63]).

Fig. 3.8 shows the source coherence effect on the generated crescent beam which has the same index (n=3). As the coherence length decreases the crescent-like distribution becomes broader and more pronounced. In our experiment, the coherence length δ is used in the computer-generated phase screen for controlling the coherence properties of the generated source. The scaling of the beam profile for long free-space propagation

distance, as shown in Figs. 3.8(d)-(f), is much larger than that at the focal plane, as captured by the experiment, even though the spectral density profiles in two cases are almost the same.

3.2.3 Interaction of the Crescent Beams with Turbulence

We will now investigate the behavior of the crescent beam, and the changes of its intensity maximum position upon propagation in an isotropic, homogeneous atmospheric turbulence. To do this, we first assume that the power spectrum of the refractive index fluctuations of turbulence obeys the von Karman distribution [21]

$$\Phi_n(\kappa) = 0.033 C_n^2 \left(\kappa^2 + \kappa_0^2\right)^{-11/6} \exp\left(-\kappa^2 / \kappa_m^2\right), \tag{3.16}$$

where C_n^2 is the refractive-index structure constant with unit $m^{-2/3}$, $\kappa_0 = 2\pi / L_0$ with L_0 being the outer scale of the turbulence, $\kappa_m = 5.92 / l_0$, with l_0 being the inner scale of the turbulence. In what follows the values of L_0 and l_0 will be fixed as $1m$ and $0.01m$, respectively. The spectral density of the crescent random beam propagating in atmospheric turbulence is then given by the formula [63]

$$\begin{aligned} S(\boldsymbol{\rho}, z) = \frac{1}{Q_3^T} \exp\left(-\frac{\rho^2}{\sigma_0^2 Q_3^T}\right) \Bigg\{ \left(\frac{Q_2^T}{Q_3^T}\right)^n L_n^0\left(-\frac{2z^2\rho^2}{k^2\sigma_0^4\delta^2 Q_3^T Q_2^T}\right) \\ - \frac{(n-1/2)!}{n!} \frac{\sqrt{2}z\rho}{k\sigma_0^2\delta Q_2^T} \left(\frac{Q_2^T}{Q_3^T}\right)^{n+1/2} L_{n-1/2}^1\left(-\frac{2z^2\rho^2}{k^2\sigma_0^4\delta^2 Q_2^T Q_3^T}\right)\cos\phi \Bigg\}, \end{aligned} \tag{3.17}$$

where

$$Q_2^T = 1 + \frac{z^2}{k^2\sigma_0^4} + \frac{2\pi^2 T z^3}{3\sigma_0^2},\ Q_3^T = Q_2^T + 2z^2 / k^2\sigma_0^2\delta^2. \tag{3.18}$$

By using Eqs. (3.17) and (3.18), we show numerical plots for the propagation properties of the crescent beam in atmospheric turbulence. Fig. 3.9 illustrates the spectral density of

the beam at several propagation distances in turbulence. It is found that when the distance is sufficiently small, i.e., less than 1km, the resultant beam profiles are like those in free space (see Figs. 3.5(a) and (b)). Nevertheless, when considering larger distances, the crescent beam distribution gradually retrieves back to Gaussian due to the turbulence-induced diffraction effects.

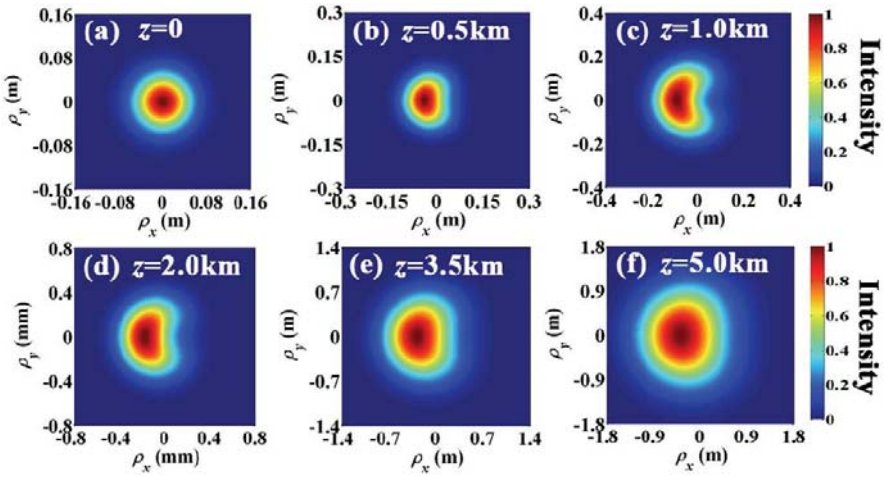

Fig. 3.9 Spectral density of the random beam propagation through atmospheric turbulence for several propagation distances. The structure parameter of turbulence is $C_n^2 = 5\times10^{-13} m^{-2/3}$ (from Fig. 5 of [63]).

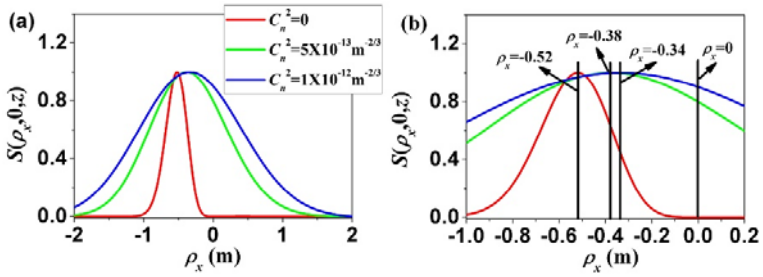

Fig. 3.10 (a) Spectral density of the random beam at the cross-line $\boldsymbol{\rho}_y$=0 with the propagation distance z=5km for three different values of structure parameters. (b) The corresponding spectral density shown in Fig. 3.10(a) with ρ_x in the range from -1m to 0.2m (from Fig. 6 of [63]).

Fig. 3.10 presents the cross-section (ρ_y=0) of the spectral density profile at the propagation distance z=5km in free space and turbulence, respectively, while different refractive index structure constants are chosen for comparison purpose. It is shown that the intensity maxima position is much closer to the on-axis point in the presence of turbulence, if it is compared with that considered in the free space case. To clearly demonstrate the evolution of intensity maxima position, we particularly show in Fig. 3.10(b) the cross section of the spectral density distribution in Fig. 3.10(a), while confining radial distance ρ_x to range from -1.0m to 0.2m. The vertical black curve notates the intensity maxima position for cases with different strengths of turbulence. The corresponding intensity maxima positions for these cases is -0.52m, -0.38m and -0.34m, respectively, while the refractive-index structure constant is chosen as $C_n^2 = 0$, $C_n^2 = 5\times10^{-13} m^{-2/3}$ and $C_n^2 = 1\times10^{-12} m^{-2/3}$, respectively.

3.2.4 Discussions and Concluding Remarks

In summary, we have studied the behavior of a class of optical beams, named as crescent random beam, which can be generated from uniformly correlated source with the complex-valued degree of coherence. We perform detailed investigations on its propagation properties in free space and homogeneous atmospheric turbulence, respectively. This random source has been shown to be capable of producing an off-axis intensity maximum at a certain propagation distance from the source plane. The crescent beam is generated experimentally by using a transmissive, nematic SLM.

We also have found that the crescent beam propagating in turbulence produces the increasing shift of maximum intensity positions from its propagation axis when the

propagation distance is increased. This means that such a beam can produce a radially accelerating maximum average intensity. This result can be compared to the one generated from the non-uniformly correlated beam whose shift of maximum intensity gradually retrieves back to its propagation axis. This transversally accelerating random beam may be of interest for optical systems for operation in curved atmospheric channels for security or convenience purposes.

Although we have introduced one beam type which shows non-symmetric spectral density distribution, its acceleration effect that we have highlighted is also similar to those produced by other sources, for example, those with the uniformly correlated, complex-valued CSD functions. The control of such radial evolution can be achieved by appropriately selecting the source type and its parameters. We have the prospect that such class of random beams which can exhibit non-linear titling phenomenon can be applicable in practical optical systems where it is essential to balance low scintillations and intensity maximum locations. In addition, since the maximum intensity of the beam traces a curved trajectory upon propagation, it can be also applied in the situations where the optical beams should be expected to pass by an obstacle embedded in the random medium.

3.3 I_m-Bessel-correlated Beam and Its Generation via Coherent Modes

The coherent laser modes have been determined for the 1D and 2D Gaussian correlation functions [34, 67-68], the 2D anisotropic Gaussian correlation function [69] and the J_0-Bessel correlation function [70]. The beams radiated from sources which were discussed

in [67-70] are all obey of the Schell type, i.e., their degrees of coherence are solely dependent on the difference between two spatial arguments. The Schell-type sources can be synthesized by using a laser beam passing through ground-glass diffusers or liquid crystals [57, 71]. Nevertheless, some stationary sources which are expressed by superposition of coherent modes are not restricted to the Schell type. A typical example is attributed to the I_{m}-Bessel-correlated source with a separable phase, which was initially introduced by Ponomarenko [72]. Such kind of source can be analytically represented as a linear superposition of the Laguerre-Gaussian (LG) modes carrying optical vortices [73].

In order to generate the source modes we use a phase-only SLM providing continuous spatial phase control of the incident beam. As a consequence, we generate a sufficiently long random sequence of frames that contain the first ten LG modes, each occupying the number of entries proportional to its eigenvalue in the coherent mode decomposition [72]. It is also shown that the produced coherent modes can carry specific Orbital Angular Momentum (OAM) index by phase conjugation approach which uses two identical SLMs having the same or opposite OAM indexes.

3.3.1 Eigenmodes and Eigenvalues of I_{m}-Bessel-Correlated Source

By recalling the approach of deterministic mode decomposition of partially coherent random sources, the eigenfunctions of the I_{m}-Bessel-correlated source satisfy the following expression [72-73]

$$\psi_n^m(\boldsymbol{\rho};\omega)=\left(\frac{\sqrt{2}\rho}{\sigma}\right)^m L_n^m\left(\frac{2\rho^2}{\sigma^2}\right)\exp\left(-\frac{\rho^2}{\sigma^2}\right)\exp(-im\phi), \tag{3.19}$$

where (ρ, ϕ) are the polar coordinates of $\boldsymbol{\rho}$, σ is the beam width at source plane, m is the OAM index, L_n^m is the associated Laguerre polynomial with order n, while the eigenvalues of such source take the form

$$\lambda_{nm} = n!\xi^n / (n+m)!. \tag{3.20}$$

Accordingly, the CSD function of the source can be represented as [72]

$$W(\boldsymbol{\rho}_1, \boldsymbol{\rho}_2; \omega) = \frac{\xi^{-m/2}}{1-\xi} \exp\left[-\frac{1+\xi}{1-\xi}\frac{\rho_1^2+\rho_2^2}{\sigma^2}\right] I_m\left(\frac{4\sqrt{\xi}}{1-\xi}\frac{\rho_1\rho_2}{\sigma^2}\right) \exp\left[-im(\phi_1-\phi_2)\right]. \tag{3.21}$$

In Eq. (3.21), I_m is the modified Bessel function of the first kind, and order m. ξ in Eq. (3.21) is real coefficient which obeys $0<\xi<1$. As two limiting situations, $\xi=0$ stands for a coherent beam, $\xi\approx1$ corresponds to an incoherent beam [72]. Therefore, the spectral density function can be obtained from Eq. (3.21) by setting $\boldsymbol{\rho}_1=\boldsymbol{\rho}_2=\boldsymbol{\rho}$ as

$$S(\boldsymbol{\rho}; \omega) = \frac{\xi^{-m/2}}{1-\xi} \exp\left[-\frac{1+\xi}{1-\xi}\frac{2\rho^2}{\sigma^2}\right] I_m\left(\frac{4\sqrt{\xi}}{1-\xi}\frac{\rho^2}{\sigma^2}\right). \tag{3.22}$$

3.3.2 Synthesis Principles and Results

We now focus on the optical system for synthesis of the LG modes and the I_m-Bessel correlated beams. The schematic diagram of the experimental setup is displayed in Fig. 3.11. First, we let a laser beam to pass through an SLM whose function is to produce the sequence of individual LG modes in the far zone. We then cycle a random sequence of phase screens (holograms) generated on the SLM. Each hologram consists of a grating which is modulated so that we only utilize the phase of diffracted beam with the first diffraction order [74]. The random sequence of phase screens is chosen in such a way that the probability of displaying a specific LG mode is proportional to its eigenvalue. It is

noteworthy that the ensemble average of all sequence frames is in agreement with the source CSD distribution.

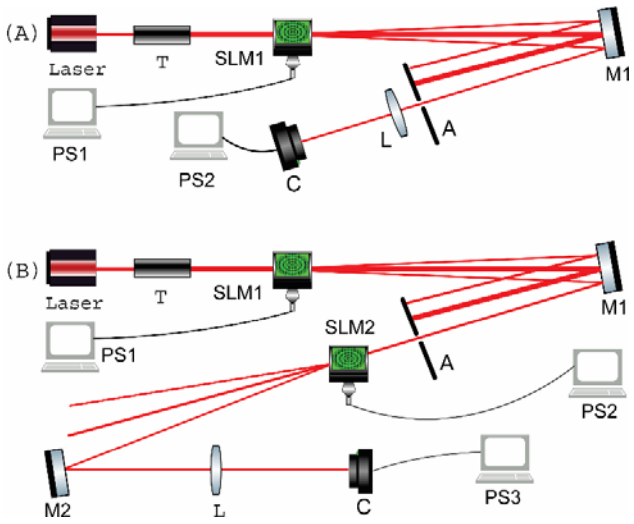

Fig. 3.11 Experimental setup for (A) generation of the individual LG modes and their sequences; (B) validation of OAM indices (from Fig. 1(B) of [75]).

In the optical setup, a 1*mm* diameter He-Ne laser beam with wavelength 633*nm* is first expanded by 15x telescope T, then passes through a SLM1 (HOLOEYE LC2012) with 1024×724 pixel array, which is controlled by computer PS1. SLM1 is placed 30cm after the telescope. SLM1 acts as a grating which generates a 2D array with multiple diffraction orders. The LG modes are picked from the first diffraction order and further reflected by mirror M1 placed at distance 200cm after SLM1, being separated from other modes by iris A placed at 155cm after M1. The resultant field further passes through a thin lens (focal length 50cm, located at 8cm after A) and is captured by a CMOS Thorlabs camera C which is at distance 30cm after L. The sequence of modes used for ensemble average incorporates 5000 frames.

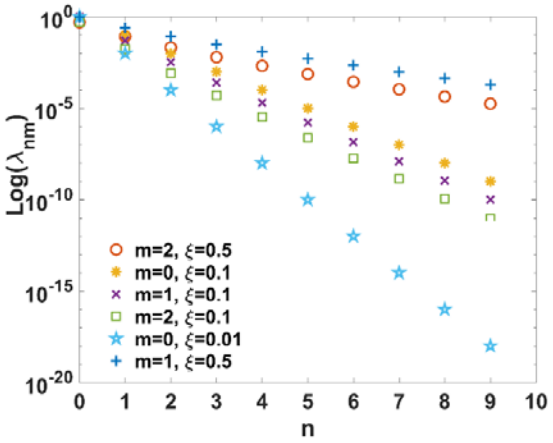

Fig. 3.12 Eigenvalues of the I_m-Bessel correlated source for values m and ξ, plotted by using Eq. (3.20) (from Fig. 6 of [75]).

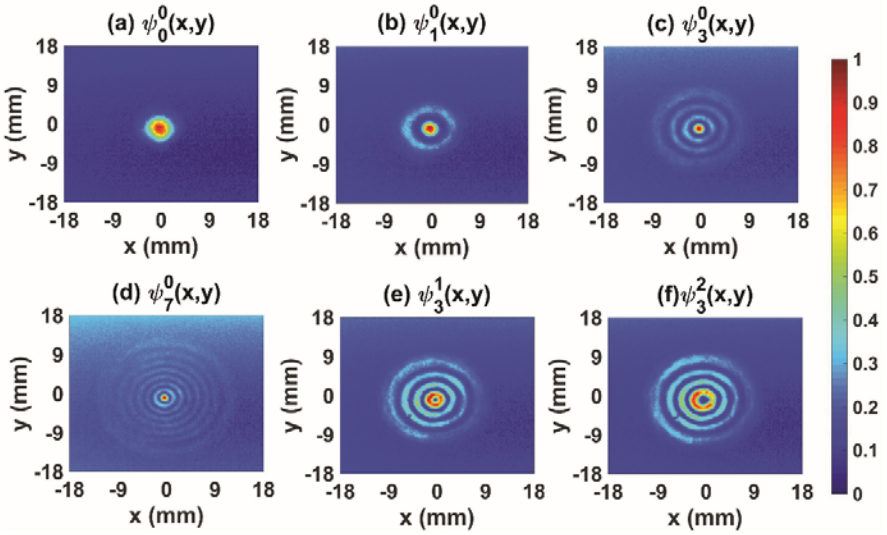

Fig. 3.13 Laguerre-Gaussian coherent modes (from Fig. 2 of [75]).

Fig. 3.12 shows the dependence of eigenvalues for the I_m-Bessel correlated source on different pairs of m and ξ, while the mode number n is chosen from 0 to 9. Results indicate that the eigenvalues become smaller when the mode number n increases. Moreover, the damping ratio of eigenvalues versus n is strongly dependent of ξ. For

smaller ξ, the corresponding eigenvalue also gives a smaller value, implying that higher-order LG mode has less influence on the source CSD distribution.

Fig. 3.13 exhibits the average intensities of the individual LG modes, which are plotted by normalization by their maximum values. Modes with n=0, 1,…,9 are produced and used for synthesis of the random source. The system using this particular type of SLM is limited to producing modes with n<9 since the outer rings of modes n>9 cannot be spatially separated from other diffraction orders. It is also shown that the modes with OAMs higher than 0 have the characteristic intensity ring in the center.

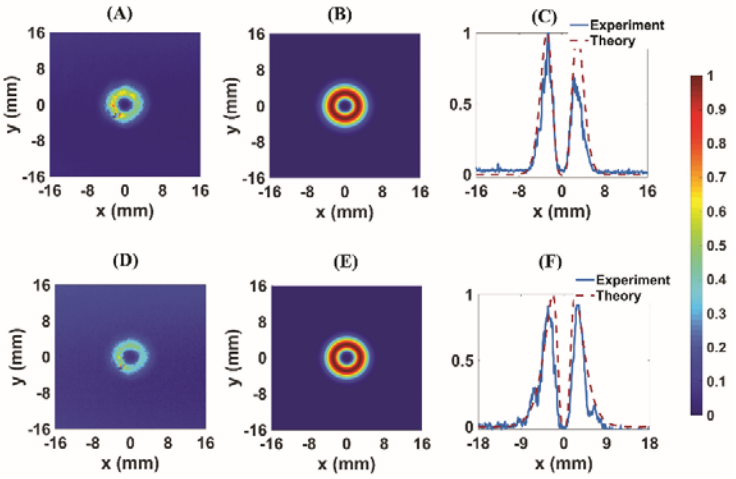

Fig. 3.14 Normalized average intensities of I_m-Bessel correlated beam with m=2. (A)-(C): ξ=0.1, (D)-(F): ξ=0.5 (from Fig. 5 of [75]).

Fig. 3.14 shows the normalized spectral density of the I_m-Bessel correlated beam recorded by the camera in configuration shown in Fig. 3.11(A). It is shown that the experimental result is in good agreement with the theoretical ones in [72]. For larger values of ξ and m the spectral density greatly spreads, and particularly, contains an outer tail with a larger size. It is also indicated in the outer tails of the higher OAM modes, for

example m=2, that the experimental data has a slight artifact. This is because larger than 10 coherent modes are necessary for precise reconstruction of the spectral density (see Fig. 3.12).

3.3.3 Phase Conjugation for Measuring Orbital Angular Momentum

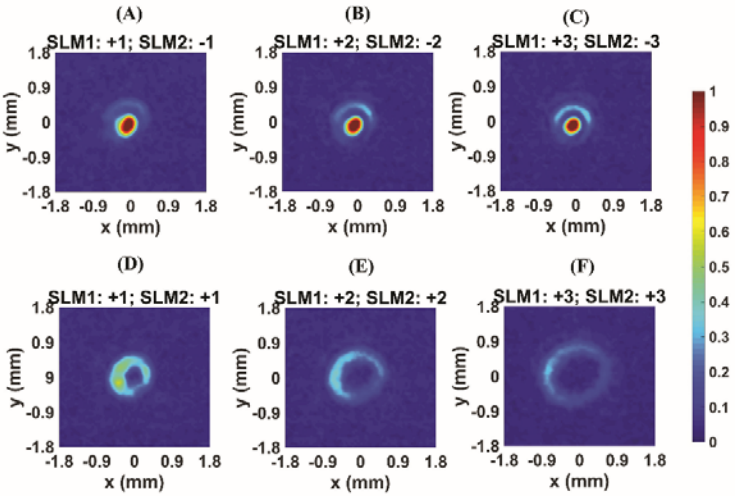

Fig. 3.15 Validation of the OAM of the beam by phase conjugation method (from Fig. 7 of [75]).

Fig. 3.15 exhibits the validation of the proper OAM of several synthesized LG modes. The first diffraction order with OAM=1, 2, 3 passes through SLM2 on which the OAM screen with $m = \pm 1, \pm 2, \pm 3$ is placed, respectively. When the phases on two SLMs take opposite signs, the corresponding total OAM is zero due to phase conjugation. Therefore, the resultant beam shows a bright spot in the central region, resembling the Gaussian beam, shown in Figs. 3.15(A)-(C). Otherwise, when the OAMs on two SLMs are the same, the total OAM is their summed value, producing a higher LG mode, i.e., a larger ring appears, as shown by Figs. 3.15(D)-(F).

3.3.4 Concluding Remarks

In summary, we showed the novel approach for the experimental synthesis of a random, stationary source for the first time, which is generated by superposition of its coherent modes passing through an SLM. Since the characteristic coherent time of the He-Ne laser source is much smaller than the cycling rate of the SLM, the modes can display random phases. It is shown that a temporally randomized, truncated sequence of coherent LG modes whose probabilities of occurrence are proportional to their corresponding eigenvalues, can be generated to reconstruct the spectral density distribution of the I_m-Bessel correlated beam. The individual LG modes can be generated by letting the He-Ne Gaussian laser beam pass through the phase-only SLM. The experimental verification of the generated OAM of individual LG modes is realized by using the phase conjugation approach. These results can be further utilized to generate random sources with other coherent mode distributions or can be applied to situations in which mode distributions are known but their CSDs do not have a closed analytic form. Our synthesis approach is essential to the free-space communication system operating in natural environments for mitigation of turbulent effects.

Chapter 4

Tuning of Properties of Laser Beams in Atmospheric Turbulence

4.1 Measurement of Anisotropy Ellipse of Atmospheric Turbulence

The theory of the Earth's atmospheric boundary layer was first proposed in 1950s in which the existence of anisotropic features of turbulence is established [76]. Then, the presence of turbulence anisotropy within several meters above ground has been reported by using the relative motion of beam centroids which are parallelly aligned and sent through the same turbulence channel [77]. There exists a strong evidence that the temperature structure function, as well as the refractive index structure function in vertical direction to ground are different from those which are evaluated in horizontal direction parallel to ground. A variety of experiments showed that anisotropy of atmospheric turbulence can exist in a wide range of altitudes [78-80]. The propagation of light through anisotropic turbulence was also introduced for both the vertical and horizontal optical channels [81-86]. The numerical simulations for describing light interactions with atmospheric turbulence mimicked by phase screens has shown good agreement with the theory [87-88]. We have also carried out experimental measurements by utilizing single-mode Gaussian He-Ne laser beam propagating close to the Earth's surface, in horizontal direction parallel to ground.

In this section, we will show the results of conducted experiments which took place in a tropical climate during summer season, at a grassy field with different meteorological conditions and heights from the ground. The instantaneous intensity of a laser beam was recorded by a CCD camera and its statistics were analysed. The beam characteristics

were used for evaluating the turbulent anisotropy parameters, i.e., the degree of ellipticity and the orientation angle of the anisotropy ellipse. Our results indicate that the two-point intensity correlation function of the beam manifests evident anisotropic features, i.e., anisotropic coefficient and orientation angle of the ellipse.

4.1.1 Configuration of Experimental Setup

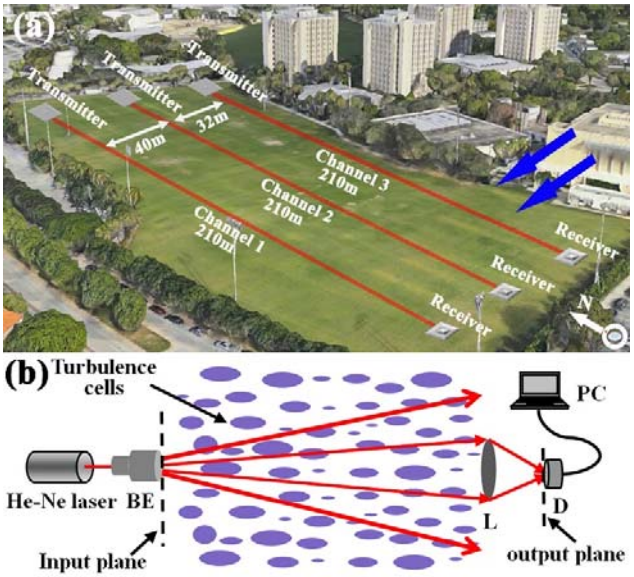

Fig. 4.1 3D map of the Yaron field at the UM. Red lines denote three atmospheric propagation channels. Wind direction was prevalently East-South-East (ESE), links are all oriented North-to-South. (b) Schematic diagram of the experimental setup. BE: beam expander; L: lens; D: detector; PC: personal computer (from Fig. 1 of [89]).

The instantaneous intensity of the He-Ne laser beam propagating through anisotropic turbulence was measured at three different heights and channels, respectively. For each channel, the distance between the transmitter and the receiver was chosen to be 210m, and the distance between channel 1 and channel 2, and between channel 2 and 3 were chosen as 40$m$and 32m, respectively. Fig. 4.1(A) shows the top view of the field

with three different propagation channels. Fig. 4.1(B) is the schematic diagram of the experimental setup. The transmitter includes a He-Ne laser with wavelength 632.8*nm* and a BE. The optical field after the BE obeys a Gaussian distribution

$$E(\boldsymbol{r},0)=E_0\exp\left(-\frac{\boldsymbol{r}^2}{\omega_0^2}-\frac{ik\boldsymbol{r}^2}{2F_0}\right), \tag{4.1}$$

where E_0 is the initial beam amplitude, k=2π/λ is the wave number, ω_0 and F_0 are the beam waist width and the radius of curvature, respectively. To minimize the beam wander effect at the receiver, we carefully adjusted the radius of curvature of the beam by via the BE adjustment, controlled by the shear plate interferometer (SPI), so that the resultant beam propagates in a slightly divergent manner. The used beam waist width and radius of curvature were about 1cm and 30m, respectively. The receiver includes a circular lens *L* with diameter 5cm and focal length 5cm, a CMOS camera and a personal computer. A part of the beam was captured by the lens and further received by the camera which was located about the focal plane of the lens. A narrow bandpass filter (632.8*nm*, *FWHM*=3*nm*) and a couple of neutral density filters were placed on the camera aperture to block the background sunlight and meanwhile adjust the intensity level of the received beam. The distance between the lens *L* and the camera was chosen about 46cm and the integrated time of the camera was set at 5ms.

4.1.2 Measurement of Average Intensity and Intensity Correlation Function

Based on the setup of above-mentioned optical links for experiments, we utilized the camera to record a sequence of 3000 frames of the instantaneous intensity. Each frame can be regarded as one realization of the beam intensity, being represented by a matrix

$I^{(m)}(x,y)$ where (x, y) denotes the coordinate values at each pixel. The superscript m indicates the number of realizations ranged from 1 to 3000. By recalling the intensity correlation function (ICF) of the propagating beam at two points, the discrete formula of ICF takes the form [21, 89]

$$B_I(\boldsymbol{\rho}_1,\boldsymbol{\rho}_2)=\frac{\sum_{m=1}^{M} I^{(m)}(\boldsymbol{\rho}_1)I^{(m)}(\boldsymbol{\rho}_2)/M}{\left(\sum_{m=1}^{M} I^{(m)}(\boldsymbol{\rho}_1)/M\right)\cdot\left(\sum_{m=1}^{M} I^{(m)}(\boldsymbol{\rho}_2)/M\right)}-1, \tag{4.2}$$

where

$$\left\langle I(\boldsymbol{\rho}_i)\right\rangle=\sum_{m=1}^{M} I^{(m)}(\boldsymbol{\rho}_i)/M, \quad (i=1, 2) \tag{4.3}$$

stands for the average intensity at position vector $\boldsymbol{\rho}_i$. In Eqs. (4.2) and (4.3), $\boldsymbol{\rho}_i=(x_i, y_i)$ are two points at the focal plane. Therefore, the ICF of the beam results in the following expression

$$B_I(\boldsymbol{\rho}_1,\boldsymbol{\rho}_2)=\frac{\left\langle I(\boldsymbol{\rho}_1)I(\boldsymbol{\rho}_2)\right\rangle}{\left\langle I(\boldsymbol{\rho}_1)\right\rangle\left\langle I(\boldsymbol{\rho}_2)\right\rangle}-1. \tag{4.4}$$

Based upon Eq. (4.2) or (4.4), we obtained the ICF evaluated at two points $\boldsymbol{\rho}_1=\boldsymbol{\rho}$, $\boldsymbol{\rho}_2=0$, and the scintillation index (SI) distribution that can be obtained by setting $\boldsymbol{\rho}_1=\boldsymbol{\rho}_2=\boldsymbol{\rho}$.

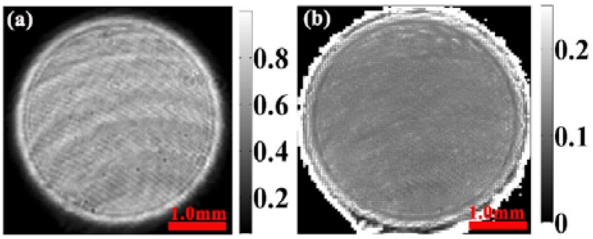

Fig. 4.2 (a) Average intensity distribution in the output plane. (b) The corresponding scintillation index across the beam received at channel 1 (typical for all links). The height of the He-Ne laser above the ground is 39cm (from Fig. 2 of [89]).

Fig. 4.2 illustrates the normalized average intensity distribution from experiments and the SI across the focal plane. The black spots in Fig. 4.2 are owing to some dust on filters. Furthermore, the dark and bright regions produced by the interference effects between the front and rear surfaces of the protecting window. Both the average intensity and the scintillation index show uniform distributions across the beam cross section, except for the instability of intensity around the edge, as shown by Fig. 4.2(b). From Fig. 4.2, we can also find that the turbulence anisotropy cannot be reflected from the average intensity and scintillation index distributions.

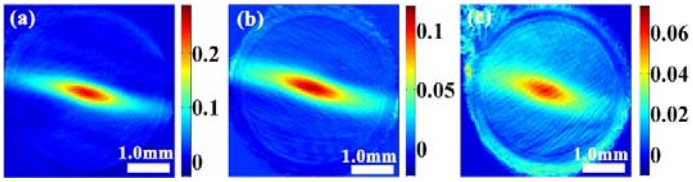

Fig. 4.3 Experimental results of the ICF distributions in the detector plane at channel 1 for three different heights of the He-Ne laser above the ground: (a) 39cm, (b) 84cm, (c) 139cm (from Fig. 3 of [89]).

Fig. 4.3 presents the experimental results of the ICF profiles at the focal plane for channel 1. The heights of the He-Ne laser above ground, shown in Figs. 4.3(a)-(c) are chosen to be 39cm, 84cm, and 139cm, respectively. It is indicated that the ICF exhibits a strong elliptical profile. Moreover, the long axis of the ellipse forms an angle θ with the horizontal axis. The values of angle θ for three different heights are almost equivalent ($\theta \approx -16°$). If we utilize a Gaussian fitting function to the long and short axes of the ellipse and evaluate the effect width of the Gaussian distribution, the corresponding degrees of ellipticity in Figs. 4.3(a)-(c) are computed as 0.32, 0.33, and 0.38, respectively, which

slightly increased with the increase of height. The on-axis scintillation index reduces when the height increases, showing that the anisotropy of turbulence becomes weakened when the height increases, as expected.

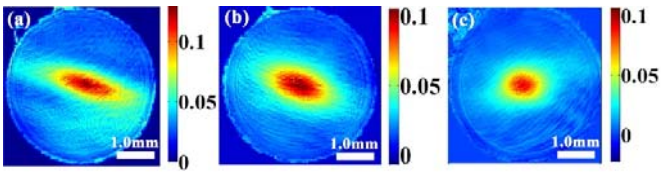

Fig. 4.4 (a) The experimental results of the ICF distributions in the detector plane at (a) channel 1, (b) channel 2 and (c) channel 3. The height of the He-Ne laser above the ground is 84cm (from Fig. 4 of [89]).

Fig. 4.4 illustrates the ICF distributions measured from experiments for three different channels. It is interesting to note that the ICF distributions measured from three channels show quite different features. If we consider channels 1 and 2, the corresponding tilt angles are around -16° and -20°, and the degrees of ellipticity are around 0.35 and 0.64, respectively. The ICFs in Fig. 4.4 are plotted by using the data from two different channels; however, the results are the same, despite the background noise is different. For channel 3, the degree of ellipticity is around 0.9, indicating for almost isotropic turbulence, in the channel close to the building. Furthermore, the tilt angle in Fig. 4.4(c) appears to show an opposite direction to those in Figs. 4.4(a)-(b).

4.1.3 Comparison of Results and Concluding Remarks

For confirmation of the validity of the obtained results, the numerical simulation based on the Wave Optics Simulation (WOS) is carried out for the laser beam propagation in anisotropic turbulence. The detailed introduction to the WOS approach for generation of

random phase screens can be found in [90]. Here we apply the Von Karman Power Spectrum Density (PSD) which satisfies the Kolmogorov power law [21]

$$\Phi_n\left(\kappa_x,\kappa_y\right)=0.033C_n^2\frac{\mu_x\mu_y\exp\left(-\kappa_x^2/\kappa_{mx}^2-\kappa_y^2/\kappa_{my}^2\right)}{\left(\mu_x^2\kappa_x^2+\mu_y^2\kappa_y^2+\kappa_0^2\right)^{11/6}}, \tag{4.5}$$

where C_n^2 is named as the structure constant of refractive index, μ_x and μ_y are the so-called anisotropic coefficients along x and y axes, respectively, κ_x and κ_y represent the spatial wave numbers along x and y axes, respectively, $\kappa_{mx(y)}=5.92/\mu_{x(y)}l_0$, $\mu_x l_0$ and $\mu_y l_0$ denote the inner scales, $\kappa_0=2\pi/L_0$ with L_0 being the outer scale.

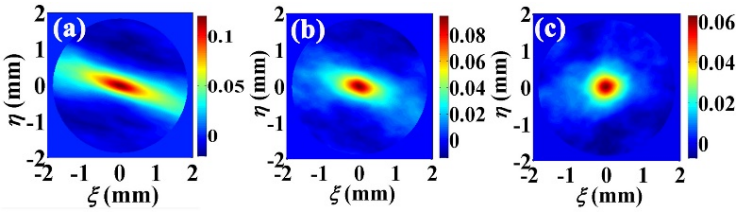

Fig. 4.5 Numerical simulation results of the ICFs for different ratios of the anisotropic factor μ_y/μ_x (a) 0.33, (b) 0.60, and (c) 0.9. The other parameters used in the simulation are the same as in Fig. 4.2 (from Fig. 6 of [89]).

Fig. 4.5 presents the numerical simulation results of the ICF distributions at the focal plane by considering different values of μ_y/μ_x. It is shown that the ICF distribution is susceptible to different values of μ_y/μ_x. The degrees of ellipticity obtained from Figs. 4.5(a)-(c) are 0.35, 0.59, and 0.88, respectively, which are close to the ratios μ_y/μ_x used in the simulation. The tilt angle of the ICF also coincides with the angle θ used in the simulation. Moreover, our simulation results (omitted here for saving space) also show that both the degree of ellipticity and tilt angle of ICF have no dependence on the strength

of turbulence. For the non-Kolmogorov case, specifically, as the power exponent in the denominator of Eq. (4.5) changes from 1.5 to 2, the corresponding degree of ellipticity and tilt angle of the ICF almost stay invariant.

Overall, we have shown that the anisotropic features of atmospheric turbulence, including the anisotropic coefficient and the angle of ellipse cannot be obtained from the average intensity or the scintillation index of the beam, however, the anisotropy of turbulence is feasible to be detected out from the two-point intensity correlation distribution. In addition, the orientation angle of ellipse needs further investigation, due to the unclear physical reasons behind its formation. The numerical simulation of beam propagation in anisotropic turbulence for the experimental scenario is also shown and further compared with the experimental data to verify its validity. These obtained results are essential to design and optimization of optical systems which are operated in the presence of anisotropic turbulence. Our discovery can also be applied for determining the parameters of anisotropic turbulence. Remarkably, our results reported on anisotropic features of atmospheric turbulence have already attracted interest by peers in our field who performed their recent studies [91-94] based on parts of our findings published in [89].

4.2 Enhanced Back-Scatter in Double-Pass Channels with Non-Classical Turbulence

The spatial redistribution of the receiving power in the double-pass atmospheric turbulence channels with mirrors or retroreflectors has been investigated for a couple of decades [95-97]. This phenomenon can be observed only when the transmitter and

receiver have overlapped field of view, and it vanishes when their fields of view are sufficiently separated. For the monostatic case which utilizes the retroreflector the corresponding on-axis intensity is stronger than that in the bistatic case, both of which produce the Enhanced Back Scattering (EBS) effect. The experimental verification of the EBS effect has been done in numerous reports [98-101]. The computer simulations have been performed for building the connection between the theoretical and experimental frames [102-103]. In most of these studies the statistics of turbulence were considered as homogeneous, isotropic and non-stationary (but with stationary increments), corresponding to the case of classic Kolmogorov turbulence. However, in a variety of practical cases the turbulence channels can be considered to have non-classic characteristics. The double-pass optical channels embedded in the non-classic atmospheric turbulence have not been considered so far and will become our primary investigation target.

In this section, we will reveal the effects of different types and the locations of non-classic turbulence in double-pass turbulence channel with 21 meter in length. The weak background laboratory environment perturbed by the locally strong turbulence is simulated by one of two approaches: by means of a single heat gun which blows hot air in a direction toward to the laser beam and by means of a 1.8-meter long turbulent chamber which contains spatially partially homogeneous and isotropic temperature. In both cases the local turbulence is created and, we aim to find how the location of the generated turbulence induces the EBS effect. Furthermore, we also found out the differences in the EBS effect due to different locations of turbulence, being produced by either heat guns or by the turbulent chamber.

4.2.1 Experimental Setup for Measuring EBS Effect

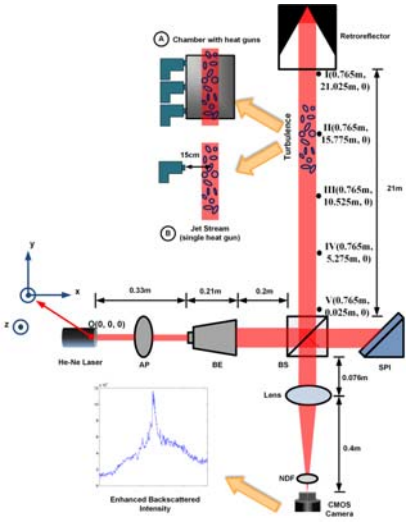

Fig. 4.6 Schematic diagram of the experimental setup used for generation and measurement of the beam intensity statistics in the monostatic double-pass link. AP: Attenuation Plate; BE: Beam Expander; BS: Beam Splitter; NDF: Neutral Density Filter; SPI: Shear Plate Interferometer. The embedded plotted curve shows the average intensity captured by the CMOS camera at the cross-section which passed through the maximum intensity plot. The NDF and AP were used to guarantee the generated images were not saturated (from Fig. 1 of [104]).

To conduct our experiment, we adopted two different methods to synthesize the non-classic turbulence along the double-passage turbulence channels, which is shown in Fig. 4.6. The first method is to utilize a jet stream produced by a single heat gun (Porter Cable, 1500W), which is tuned to the highest temperature (1100°F) and the highest fan speed. The second one is to use a parallelepiped-like wooden chamber (15cm×15cm×180cm in size), which is entirely wrapped by aluminum foil, leaving 9 holes drilled into

single lateral side. Either one or three heat guns were placed into these holes, as discussed above. When doing each measurement, the heat guns were fired from the same side of the channel to ensure consistency for comparison purposes. Fig. 4.6 is the diagram of the double-pass channel which can be alternated between the two methods described above. All the distances used in the experiment have been labeled in the diagram. First, a He-Ne Laser (wavelength 632.nm, average power 2mW) produced a 1mm (in radius) collimated beam which passed through an attenuation plate, a 15x beam expander and then a beam splitter (5cm side length, 50:50). The BS splits the beam into two perpendicular paths, one subsequently passes through the optical channel (21m long in propagation length), reflecting from the retroreflector, and going back along the opposite direction. After passing through the BS for the second time the backward beam was focused by a thin lens (focal length f=50cm) into a CMOS camera (Thorlabs, Color, pixel resolution 1280 $\times$1024). For each measurement the camera captured 1000 image sequence by using frame rate 6.55Hz and the exposure time 0.02 milliseconds.

For easier understanding of the non-classic turbulence produced at different locations, we show in Fig. 4.6 the 3D Cartesian coordinate system shown. The sign "⊙" indicates that +z axis is pointing outside of the screen. In the experiment either a single heat gun or a turbulent chamber was placed at five locations marked by I, II, III, IV, and V, which separate the whole turbulence channel into four equal distance (5.25m each). Either the heat gun was placed at one location or at the end of the chamber nearest to the retroreflector. To guarantee the beam has been well collimated the split beam at the second path was passed through the SPI (Thorlabs, SI254) where the interference pattern was generated to test whether the propagating beam has been collimated or not.

4.2.2 Turbulent Jet-stream and Non-Classical Turbulence Results

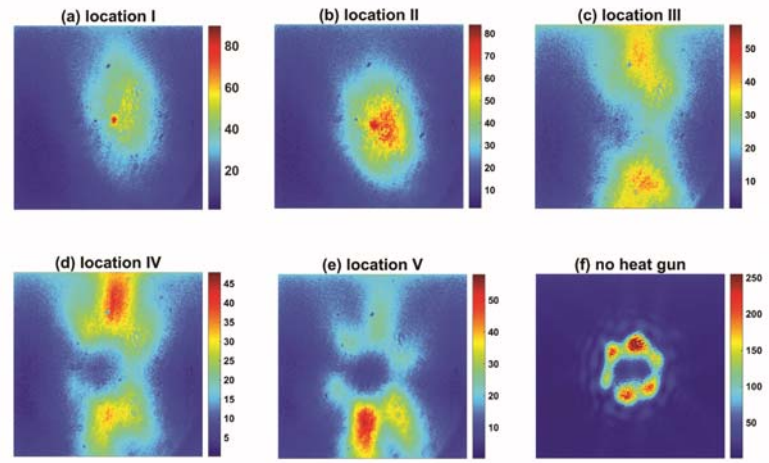

Fig. 4.7 Average intensity captured by the camera and calculated for the ensemble of 1000 frames. The localized turbulence was generated by one heat gun with no chamber. The heat gun was located at (a) I, (b) II, (c) III, (d) IV, (e) V, and (f) no heat gun was placed (from Fig. 2 of [104]).

Fig. 4.7 displays the average intensity distributions of the focused beam captured by the camera. The non-classic turbulence of the jet-stream type that can be produced by using a single heat gun, is placed along the $+x$ axis at distance 15cm from the propagating beam path. The bright spot at the central region of the beam can be clearly observed when the heat gun is fired next to the retroreflector at location I. By contrast, it becomes less pronounced when the heat gun is put at location II. The EBS effect entirely disappears when the heat gun is placed at location III-V. It is also found that the location of the beam centroid in Fig. 4.7(a) does not exactly agree with the EBS position. Besides, just like the average intensity distribution in the double-passage channel with no turbulence, as shown in Fig. 4.7(f), the average intensity captured by the camera for the

cases where the heat gun is placed at locations III and IV can be partially separated into two patterns in vertical directions, as shown by Figs. 4.7(c) and 4.7(d). Moreover, if we compare Figs. 4.7(e) with 4.7(f), it is interesting to find that the average intensity profile obtained for the case where turbulence is generated at location V is similar to the no-turbulence pattern. The deterioration of the EBS effect in Figs. 4.7(b)-(e) when comparing with that shown in Fig. 4.7(a) can be attributed to the presence of considerable deterministic phase discrepancy between the emitted and reflected beams. Such phase difference is induced by the free space diffraction effect from the propagating beam.

Fig. 4.8 illustrates the average intensity distributions of the reflected beam captured by the camera in the case of chamber-induced turbulence. The chamber turbulence produced by using one heat gun inside and placed at three different distances from the retroreflector, i.e., locations I, II, and III. The EBS effect can be only observed for turbulence at location I. It is shown that the beam centroid greatly shifts from the central region of camera for locations II and III, as shown in Figs. 4.8(b) and 4.8(c). This is because when the beam propagates through the chamber turbulence the tilt of phase generated by the temperature gradient in vertical direction among chamber is stronger, which results in a more distinct centroid shift from the central region of camera.

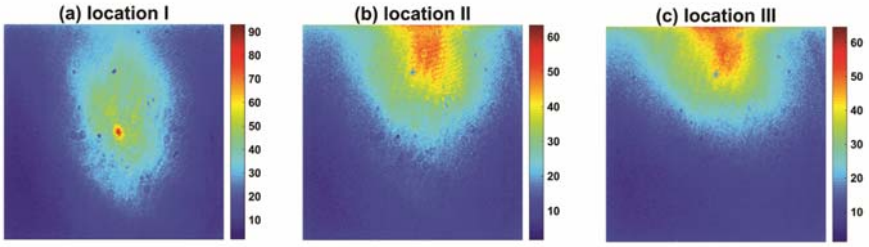

Fig. 4.8 Average intensities captured by the camera over 1000 frames. The localized turbulence was generated by using a chamber with one heat gun. The chamber is located at (a) I, (b) II, and (c) III (from Fig. 3 of [104]).

4.2.3 Comparisons of Results from Two Types of Turbulence

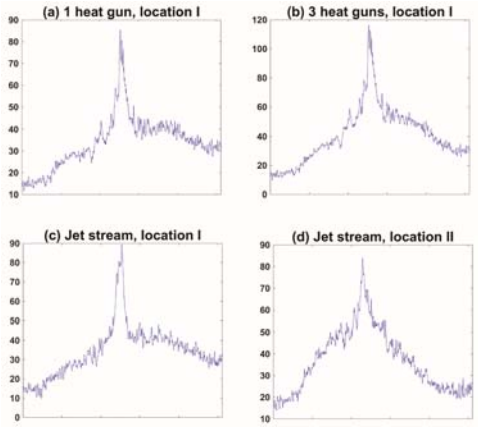

Fig. 4.9 Average intensities at vertical cross-section captured by the CCD camera over 1000 frames. The localized turbulence was generated by using either (a) single heat gun inside chamber at location I, (b) 3 heat guns inside chamber at location I, (c) single heat gun at location I, and (d) single heat gun at location II (from Fig. 5 of [104]).

Fig. 4.9 exhibits the EBS profile at the vertical cross-section of the camera plane for the double-pass optical channel embedded in four typical classes of localized turbulence. The results indicate that the EBS manifested by bright spots can be observed for these four cases. The localized turbulence produced by applying the turbulent chamber with three heat guns leads to the strongest EBS effect at the central region, when comparing with other three cases. This phenomenon emerges because the chamber preserves the flowing heat produced by heat guns, so that three heat guns can produce stronger turbulence. Furthermore, the chamber with three heat guns can produce more spatially

uniform temperature, as shown by Fig. 4.9(b). Even though, the jet stream generated at position II, which is produced by using single heat gun is still able to induce the EBS effect at the central region, as shown by Fig. 4.9(d).

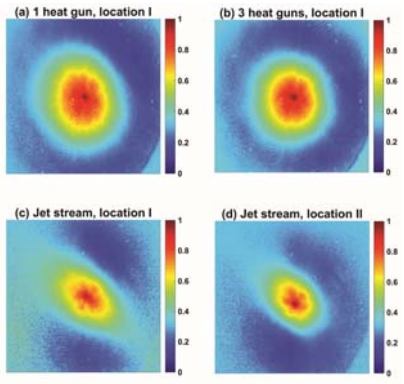

Fig. 4.10 Normalized ICF of the EBS intensity captured by the camera. The localized turbulence in (a)-(d) were generated in the same ways as that in Figs. 4.9(a)-(d), respectively (from Fig. 6 of [104]).

Fig. 4.10 shows the normalized ICF profiles of the beam captured by camera by using different types of non-classic turbulence. Each plot was normalized to the correlation at its maximum value at a certain pixel. In such case, the two-point ICF of the focused beam can be formulated as [104]

$$C_N\left(\boldsymbol{r}_1,\boldsymbol{r}_2\right)=\left\langle I\left(\boldsymbol{r}_1\right)I\left(\boldsymbol{r}_2\right)\right\rangle/\left\langle I\left(\boldsymbol{r}_1\right)I\left(\boldsymbol{r}_2\right)\right\rangle_{\max}, \tag{4.6}$$

where $\boldsymbol{r}_1$ and $\boldsymbol{r}_2$ are two position vectors specified at the double-pass turbulence channel, while the subscript denotes the maximum value of the ICF. Compared with Eq. (4.4), Eq. (4.6) defines the normalization regarding to its maximum value, however, Eq. (4.4) introduces the normalization with respect to the product of the average intensities at two positions. It is clear that the ICF shows circular distributions for the turbulence cases when either one or three heat guns were fired inside the chamber. As the comparison, the

ICF obtained in double-pass turbulence for the jet stream case shows elliptical profile, which indicates that the jet stream can produce very strong anisotropic turbulence [89, 105], especially when we compare Figs. 4.10(c) and 4.10(d) with Figs. 4.10(a) and 4.10(b). Furthermore, the effective sizes of the ICF profiles for the turbulent chamber cases are much larger than those shown in the jet stream cases which have no chamber, as shown by the comparison between Figs. 4.10(c)-4.10(d) and Figs. 4.10(a)-4.10(b). This result indicates that the strength of turbulence generated by a single heat gun without chamber is much stronger than that any other cases. Our findings are of importance for future studies which rely upon using EBS effect to measure statistics of non-classic turbulence.

4.2.4 Concluding Remarks

In summary, we have conducted laboratory experiments to measure the EBS statistics of a He-Ne laser beam in the double-pass turbulence channel containing a retroreflector and heat-induced localized turbulence. The results show that in two cases where the turbulence is produced by utilizing a highly directional jet stream or by applying an enclosed turbulent chamber, the resultant EBS effect is greatly dependent on the input turbulence location, while it is the strongest at the position next to the retroreflector. Moreover, in both cases, for the heat-gun and the chamber induced turbulence the temperature gradient was found to shift the EBS beam spot from the beam centroid in two entirely different directions: the centroid moves upward for the chamber case and along the direction of air flow from the heat gun for the jet steam case.

Chapter 5

Structuring Light Properties by its Interaction with Soft Biological Tissue

5.1 Laser Light Scintillation in Soft Biological Tissue

In recent decades numerous studies have been performed to reveal the characteristics of great variety of optical/infrared beams upon propagation through soft biological tissues, e.g., [106-107]. These research works were done by using the extended Huygens-Fresnel integral [21] for evaluation of the second-order wave statistics, for example, average intensity, state of polarization, spectral distribution, etc. Nevertheless, so far investigation of typical distances inside the bio-tissue where coherent beam intensity experiences weak, moderate and strong fluctuations has not been tackled [21]. Such type of analysis can be made using the Scintillation Index (SI) of a plane wave, which is also named as the Rytov variance. The moderate fluctuations of instantaneous intensities occur once the Rytov variance reaches unity value [21]. Recently scientists have attempted to investigate the behavior of SI of coherent waves propagating in bio-tissues [108-109]. However, the former study only handled the tissues with power law 11/3 which coincides with the classic atmospheric turbulence, while the later one only confines to the study of the spherical wave. Furthermore, the SI of beams passing through other natural random media with power-law spectra, e.g., atmospheric turbulence and oceanic turbulence, have been also investigated in detail [110-111].

In this section, we will reveal the behavior of the SI of a plane wave, a spherical wave and of a Gaussian beam upon propagation through a typical soft bio-tissue and demonstrate its applicability limits of the Rytov test.

5.1.1 Scintillation Indices of Plane and Spherical Waves in Tissue

First let us concentrate on the SI of a plane wave (Rytov variance) upon propagation through bio-tissues to find the applicability limits of the Rytov test: *the incident wave experiences weak fluctuations induced by tissues when the Rytov variance is smaller than unity*. For a general Gaussian wave, we start by defining Λ_0 and Θ_0 as non-dimensional parameters relating to its initial source parameters by [21]

$$\Theta_0 = 1 - L / F_0,\ \Lambda_0 = 2L/\left(kW_0^2\right), \tag{5.1}$$

where k=2π/λ is the wave number, λ denotes the wavelength, L represents the propagation distance, F_0 is called wave front radius of curvature of source, and W_0 is effective radius of source. For such Gaussian beam, its propagation properties at a certain output plane can be characterized by a pair of parameters Λ and Θ, i.e.

$$\Theta = \Theta_0\left(\Theta_0^2+\Lambda_0^2\right)^{-1},\ \Lambda = \Lambda_0\left(\Theta_0^2+\Lambda_0^2\right)^{-1}. \tag{5.2}$$

Regarding to the cases of plane wave (Λ=0 and Θ=1) and spherical wave (Λ=0 and Θ=0), the radial part of SI σ_r^2 vanishes, while only the longitudinal part of SI σ_l^2 remains [21]. For the plane wave case, the radial part of its SI takes the integral form [21]

$$\sigma_l^2\left(0,L\right) = 8\pi^2k^2L\int_0^1\int_0^\infty \kappa\Phi_n\left(\kappa\right)\left[1-\cos\left(L\kappa^2\xi/k\right)\right]d\kappa d\xi, \tag{5.3}$$

where L is the propagation distance in bio-tissue, Φ_n is the 3D power spectrum of the tissue medium, κ is the spatial frequency amplitude. The normalized correlation function and 3D power spectrum of bio-tissues have the following analytical expressions, respectively [112-113]

$$C\left(r\right) = \frac{2}{\Gamma\left(\alpha-3/2\right)}\left(\frac{r}{2L}\right)^{\alpha-3/2}K_{\alpha-3/2}\left(\frac{r}{L}\right),\qquad (1.5<\alpha<2), \tag{5.4}$$

$$\Phi_n(\kappa)=\frac{\sigma^2 L_0^3\Gamma(\alpha)}{\pi^{3/2}\Gamma(\alpha-3/2)\left(1+\kappa^2L_0^2\right)^{\alpha}},\qquad (1.5<\alpha<2). \tag{5.5}$$

By substituting from Eq. (5.5) into Eq. (5.3) and by changing the integral variable $t=\kappa^2L_0^2$, we readily obtain the longitudinal part of SI as the following form

$$\sigma_l^2(0,L)=\frac{4\sqrt{\pi}k^2L\sigma^2L_0\Gamma(\alpha)}{\Gamma(\alpha-3/2)}\left[\frac{1}{\alpha-1}-\frac{kL_0^2}{L}\int_0^{\infty}\frac{1}{t(1+t)^{\alpha}}\sin\left(\frac{Lt}{L_0^2k}\right)dt\right]. \tag{5.6}$$

Eq. (5.6) needs further numerical integration to obtain an analytical solution. To this effort, in what follows uniform parameters for incident wave and bio-tissue are chosen: λ=1.55μm, σ^2 =5 × 10^{-4}. Fig. 5.1 illustrates the Rytov variance changes versus propagation distance L in (a) and (b); and versus power law constant α in (c). Fig. 5.1(a) shows that the Rytov variance becomes larger for small outer scale. Figs. 5.1(b) and 5.1(c) reveals the dependence of Rytov variance on α and L_0. It is found that the weak regime of refractive index fluctuations of bio-tissue is confined to several tens of microns. This result indicates that the refractive capacity of bio-tissue induced by large scales weakens at this range meanwhile the scattering effects caused by small scales become dominant.

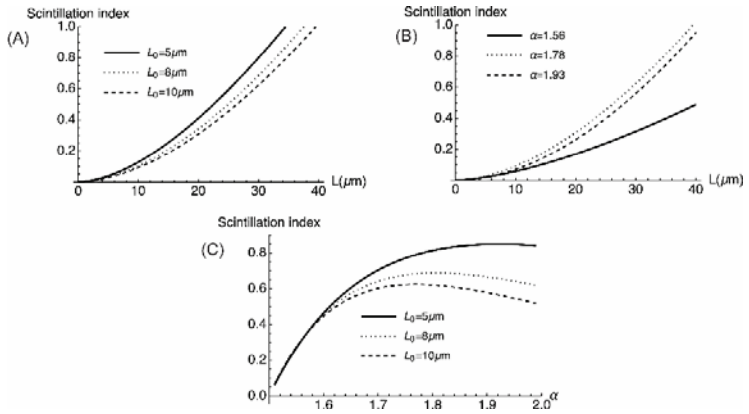

Fig. 5.1 Rytov variance: (a) α=1.78; (b) L_0=10μm; (c) L=30μm (from Fig. 1 of [113]).

For the spherical incident wave which has propagation parameters Λ=0 and Θ=0, the radial part σ_r^2 of its SI vanishes and its longitudinal part results in the expression [113]

$$\sigma_l^2(0,L)=\frac{8\sqrt{\pi}k^2L\sigma^2L_0^3\Gamma(\alpha)}{\Gamma(\alpha-3/2)}\left[\frac{1}{2L^2(\alpha-1)}-\int_0^1\int_0^\infty\frac{\kappa}{\left(1+\kappa^2L_0^2\right)^\alpha}\cos\left[L\kappa^2\xi(1-\xi)/k\right]d\kappa d\xi\right]. \quad (5.7)$$

Based on Eq. (5.7), further numerical integration can be performed to plot Fig. 5.2 which shows the SI of the spherical wave changing versus different parameters of bio-tissues.

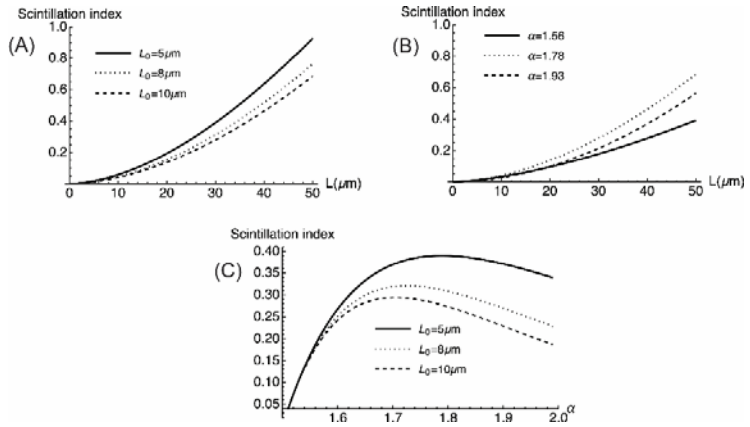

Fig. 5.2 SI distributions of the spherical wave: (a) α=1.78; (b) L_0=10μm; (c) L=30μm (from Fig. 2 of [113]).

Through comparing Fig. 5.1 with Fig. 5.2 it can be noticed that the primary behavior of the SI are the same but the values for the spherical wave case is smaller.

5.1.2 Scintillation Index of Gaussian Beam in Tissue

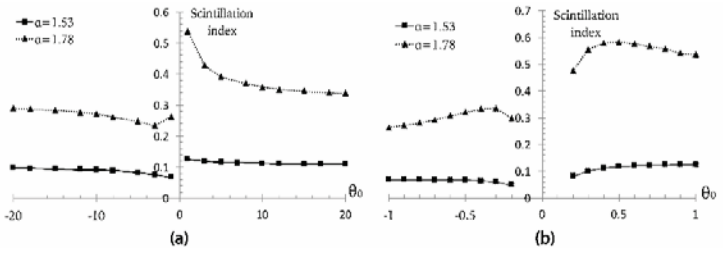

Fig. 5.3 On-axis SI of Gaussian beam (r=0) with Λ_0=0.1, L=30μm, L_0=8μm (from Fig. 4 of [113]).

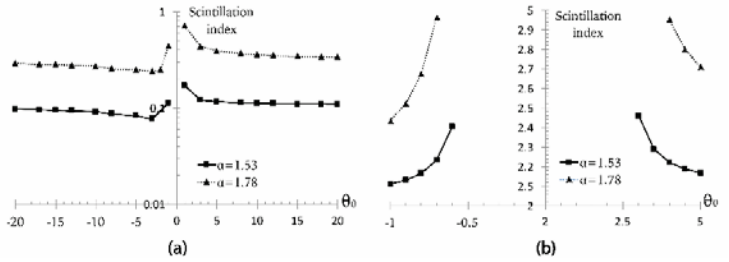

Fig. 5.4 Off-axis SI of incident Gaussian beam with r=10μm, Λ_0=0.1, L=30μm, L_0=8μm (from Fig. 5 of [113]).

Figs. 5.3 and 5.4 display the dependence of the on-axis and off-axis SI on Θ_0 and α, respectively, while subfigures (b) show the zoom-in portion of plots in (a). It is shown that the SI attains its minimum when Θ_0=0 and achieves its maximum value when Θ_0=1. However, such result no longer holds true when Θ_0 increases to even larger values. As shown by Fig. 5.4, by choosing r=10μm and W_0=12μm, the corresponding SI exhibits a singularity when Θ_0=0 due to the reason that the propagation distance chosen here is the same as the focusing parameter of the beam. Besides, the SI approaches a constant value when Θ_0 increases to larger values. In general, the SI of the collimated Gaussian beam (Θ_0=1) is larger than that for focused or defocused beam cases. Remarkably, in both the on- and off-axis cases the values of their SI are always larger when α becomes smaller.

Fig. 5.5 reveals the dependence of the SI of the Gaussian beam on Λ_0, while collimated beam in (a) and focused beam in (b) are considered, respectively. For the on-axis case the SI of the collimated beam (r=0) takes minimum value at the region of its first Fresnel zone (Λ_0=1), while for the case of the diffractive beam edge (r=W) the corresponding SI reaches its maximum value at the region of its first Fresnel zone. However, considering the cases of near field (Λ_0<<1) and far field (Λ_0>>1), the SI

evaluated at the beam edge diminishes. Regarding the focused Gaussian beam, when α=1.78, the SI is almost the same as that from the collimated beam case. By contrast, when α=1.53 the peak position of the SI at the beam edge shifts to $\Lambda_0 \approx 0.1$.

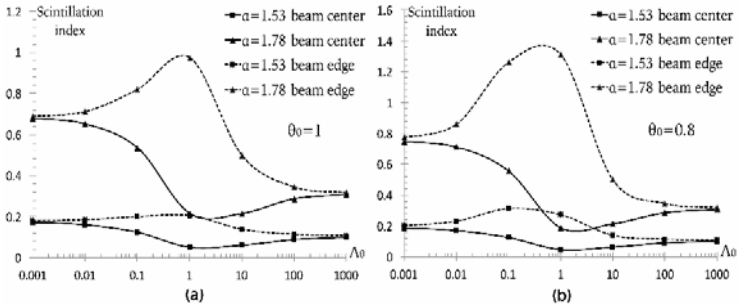

Fig. 5.5 The SI of Gaussian beam: (a) collimated beam (Θ_0=1), (b) focused (Θ_0=0.8). Other parameters are chosen as L=30μm, L_0=8μm (from Fig. 6 of [113]).

5.1.3 Concluding Remarks

Overall, we have applied the second-order Rytov phase perturbation theory to investigate the SI behavior of a Gaussian laser beam propagating in an isotropic and homogeneous bio-tissue which has a typical fractal-like power spectrum of refractive index fluctuations and a finite outer scale. Our discovery provides deep insight into the interaction mechanism between a variety of waves and the bio-tissues, separating the predominantly refractive-based regime of weak fluctuations from the scattering regime of moderate and strong fluctuations. As a result, the expressions of the SI of the plane and the spherical waves are derived, respectively, and are further adopted for determining the threshold between weak and moderate fluctuation regimes. Regarding typical tissues and waves such distance is verified to be limited to few tens of micrometers. Therefore, the bio-tissue effects implemented on the waves pertinent to the weak regime can be almost omitted when comparing to other types of natural media. Furthermore, we also have

overviewed the spatial power spectra of turbulence for different dimensions. We envision that our results may attract interest in medical imaging and diagnostics field.

5.2 Weak Scattering of Light from Quasi-Homogeneous Biological Tissue

It has been well known that the variation of the refractive index of the classic soft biological tissues can be regarded as a stationary, homogeneous and isotropic random process. Considering most tissues, their average optical statistics, e.g., the mean and the variance of the refractive index, the scattering and absorption coefficients have been in-depth explored [114]. However, some finer structure parameters of bio-tissues, for example, their particle size distribution, remains poorly characterized. In the seminar work [115] the 2D power spectra of human and animal tissue have been determined from the microscopy images and further fitted to the power law curves with a high frequency cutoff pertinent to the outer scale of the tissue, i.e., the largest scale which represents the constant refractive index in bio-tissues. The smallest scale incorporated in light scattering process, which is also named as the inner scale, has not been systematically addressed due to the resolution limit of microscopy technique, and, therefore, was not involved in the theoretical bio-tissue models. The correlation function of the tissues' refractive index can be determined by using its power spectrum reported in [116] which is interpreted as a 2D Fourier transform of the correlation function. It is verified to belong to the Whittle-Matern correlation family [117]. The 1D and 2D statistics of tissues so far have attracted great interest since thin tissue slices are frequently in medical diagnostics [34].

5.2.1 Direct Problem of Weak Scattering from Soft Tissue

In this section, we aim to obtain the correlation function of the 3D biological tissue which is characterized by the 3D Whittle-Matern correlation family [118-120]

$$\eta_F\left(\boldsymbol{r}_1',\boldsymbol{r}_2';\omega\right)=\frac{2}{\Gamma\left(m-3/2\right)}\left(\frac{\boldsymbol{r}_2'-\boldsymbol{r}_1'}{2L_0}\right)^{m-3/2}K_{m-3/2}\left(\frac{\boldsymbol{r}_2'-\boldsymbol{r}_1'}{L_0}\right), \tag{5.8}$$

where $K_{m\text{-}3/2}$ denotes the second-order modified Bessel function with order m-3/2, L_0 represents outer scale of bio-tissue, Γ stands for the Gamma function, m is defined as the fractal exponent of the 3D tissue medium which takes values between the interval (1.5, 2). For such case, we can obtain the CSD function of the far-zone scattered field from a bio-tissue medium (see Eq. (9) of [119])

$$W^{(s)}\left(r_1\boldsymbol{s}_1,r_2\boldsymbol{s}_2;\omega\right)=\frac{\exp\left[ik\left(r_2-r_1\right)\right]}{r_1r_2}\frac{8\pi^{3/2}L_0^3\Gamma\left(m\right)}{\Gamma\left(m-3/2\right)}\tilde{I}_F\left(k\boldsymbol{s}_{\boldsymbol{d}};\omega\right)\left[1+k^2L_0^2\left|\boldsymbol{s}_s-\boldsymbol{s}_0\right|^2\right]^{-m}, \tag{5.9}$$

where

$$\tilde{I}_F\left(k\boldsymbol{s}_{\boldsymbol{d}};\omega\right)=\int_V I_F\left(\boldsymbol{r}_s';\omega\right)\exp\left(-ik\boldsymbol{s}_d\cdot\boldsymbol{r}_s'\right)d^3r_s' \tag{5.10}$$

is defined as the 3D Fourier transform of the strength of potential of the biological tissue. The spectral density of the far-zone scattered field can be derived from Eq. (5.9) by considering $r_1=r_2=r$ and $\boldsymbol{s}_1=\boldsymbol{s}_2=\boldsymbol{s}$

$$S^{(s)}\left(r\boldsymbol{s};\omega\right)=\frac{1}{r^2}\frac{8\pi^{3/2}L_0^3\Gamma\left(m\right)}{\Gamma\left(m-3/2\right)}S^{(i)}\left(\omega\right)\tilde{I}_F\left(0;\omega\right)\left[1+\boldsymbol{K}^2L_0^2\right]^{-m}, \tag{5.11}$$

where $\boldsymbol{K}=k(\boldsymbol{s}\text{-}\boldsymbol{s}_0)$ is called the momentum transfer vector of which the magnitude $K=\left|\boldsymbol{K}\right|=2k\left|\sin\left(\theta/2\right)\right|$, and $\theta=\arccos\left(\theta\cdot\theta_0\right)$ is the azimuthal scattering angle. Eq. (5.11) indicates that the spectral density of the scattered field is only dependent of the distribution of the tissue's degree of correlation η_F, and it is only scaled by the maximum

value of the Fourier transform of the strength of potential, i.e., $\tilde{I}_F(0;\omega)$. Such result has been well interpreted as the reciprocal relation for any QH media type [120]. Eq. (5.9) can be alternatively utilized to derive the degree of coherence of the scattered field by applying another reciprocal relation.

Fig. 5.6 illustrates the dependence of the far-zone scattered spectral density plotted by using Eq. (5.11), and using a logarithmic scale, on the scattering angle θ, on the outer scale L_0, as well as on the fractal exponent m of the tissue, respectively. By assuming that the biological tissue is homogeneous within its volume, so that its strength of potential is equal to its VRI, i.e. $I_F(\boldsymbol{r}';\omega)=\langle \delta n^2 \rangle$, and its corresponding Fourier transform is $\tilde{I}_F(0;\omega)=\langle \delta n^2 \rangle V$, where V is the tissue volume. As numerical parameters, we keep fixed the wavelength λ=632.8nm and VRI $\langle \delta n^2 \rangle = 0.004$, which are typical values used in the previous work [115]. We also setup the amplitude coefficient as unity, i.e., $S^{(i)}(\omega)V/r^2=1$. The result shows that the spectral density of the scattered field specified at a certain scattering angle increases with larger values of the outer scale and fractal exponent. Specifically, larger values of the outer scale can produce weaker scattering effect of tissue. Furthermore, the spectral density of scattered field monotonically drops down to zero by increasing the azimuthal scattering angle θ, and it eventually approaches zero when the scattering angles is chosen as $\pi/3$.

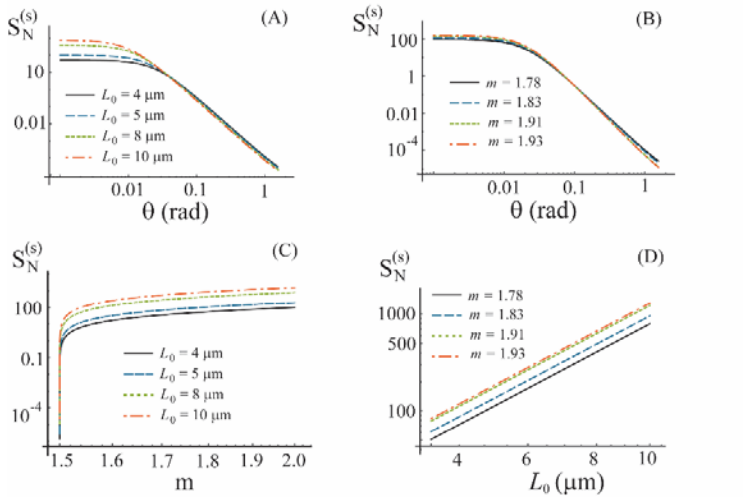

Fig. 5.6 The spectral density scattered from a biological tissue (logarithmic scale), plotted from Eq. (5.11). The parameters used for the plots: (A) m=1.78; (B) L_0=5μm; (C) and (D) θ=0 (from Fig. 1 of [119]).

5.2.2 Inverse Problem of Weak Scattering from Soft Tissue

Let us now address the inverse-scattering problem which aims to determine three parameters of the 3D biological tissue: m, L_0 and $\tilde{I}_F(0;\omega)$ by obtaining the angular scattered spectral density in the far zone, as given by Eq. (5.11). As the initial step, the maximum spectral density can be obtained by setting θ=0 or $\boldsymbol{K}$=0 in Eq. (5.11) such that

$$S^{(s)}(0;\omega)=\frac{8\pi^{3/2}L_0^3}{r^2}\frac{\Gamma(m)}{\Gamma(m-3/2)}S^{(i)}(\omega)\tilde{I}_F(0;\omega). \tag{5.12}$$

Subsequently, we obtain the normalized spectral density of scattered field at any arbitrary scattering angle θ by taking the ratio of Eqs. (5.12) to (5.11)

$$S_N^{(s)}(\theta;\omega)=\frac{S^{(s)}(\theta;\omega)}{S^{(s)}(0;\omega)}=\left[1+4k^2L_0^2\sin^2(\theta/2)\right]^{-m}. \tag{5.13}$$

As a result, the fractal exponent m has the following form

$$m = \frac{\ln\left[S_N^{(s)}(\theta;\omega)\right]}{\ln\left[1+4k^2L_0^2\sin^2(\theta/2)\right]}. \tag{5.14}$$

The typical values of the outer scale L_0 indexed in [111] indicate that kL_0>>1 should be satisfied. Therefore, we can readily get the following approximation from by assuming that the scattering angle θ is sufficiently large, i.e.

$$1+4\mathrm{k}^2\sin^2(\theta/2)L_0^2 \approx 4k^2\sin^2(\theta/2)L_0^2. \tag{5.15}$$

Then Eq. (5.14) turns out to be

$$m' = -\frac{\ln\left[S_N^{(s)}(\theta_1;\omega)\right]}{2\ln\left(kL_0'\right)+\ln\left[2\sin(\theta_1/2)\right]} = \frac{\ln\left[S_N^{(s)}(\theta_2;\omega)\right]}{\ln\left(kL_0'\right)+\ln\left[2\sin(\theta_2/2)\right]}. \tag{5.16}$$

where we used m' and L_0' to distinguish the reconstructed values from the original ones. By performing measurements at two different scattering angles, namely θ_1 and θ_2, the value of m should remain invariant, such that

$$\frac{\ln\left[S_N^{(s)}(\theta_1;\omega)\right]}{\ln\left(kL_0'\right)+\ln\left[2\sin(\theta_1/2)\right]} = \frac{\ln\left[S_N^{(s)}(\theta_2;\omega)\right]}{\ln\left(kL_0'\right)+\ln\left[2\sin(\theta_2/2)\right]}. \tag{5.17}$$

Then the reconstructed value of the outer scale L_0' can be derived as

$$L_0' = \frac{1}{2k}\sin\left(\frac{\theta_1}{2}\right)^{-\alpha}\sin\left(\frac{\theta_2}{2}\right)^{-\beta}, \tag{5.18}$$

where

$$\alpha = \ln\left[S_N^{(s)}(\theta_2;\omega)\right] / \ln\left[\frac{S_N^{(s)}(\theta_1;\omega)}{S_N^{(s)}(\theta_2;\omega)}\right], \tag{5.19}$$

$$\beta = \ln\left[S_N^{(s)}(\theta_1;\omega)\right] / \ln\left[\frac{S_N^{(s)}(\theta_1;\omega)}{S_N^{(s)}(\theta_2;\omega)}\right]. \tag{5.20}$$

The reconstructed value of the fractal exponent can be further obtained by substituting from Eqs. (5.18)-(5.20) into (5.16)

$$m' = -\ln\left[S_N^{(s)}\left(\theta_1;\omega\right)\right] / \left\{2\ln\left[\frac{\sin^{\alpha}\left(\theta_2/2\right)}{\sin^{\beta}\left(\theta_1/2\right)}\right]\right\}. \tag{5.21}$$

Finally, we can also determine the Fourier transform of the reconstructed strength of potential of bio-tissue by using Eq. (5.13)

$$\tilde{I}_F\left(0;\omega\right)' = \frac{r^2}{8\pi^{3/2}L_0'^3}\frac{\Gamma\left(m'-3/2\right)}{\Gamma\left(m'\right)}\frac{S^{(s)}\left(0;\omega\right)}{S^{(i)}\left(\omega\right)}, \tag{5.22}$$

where m' and $L_0^{'}$ have been determined from Eq. (5.21) and (5.18), respectively. As a particular case, the VRI for a homogeneous tissue with volume V can be derived as

$$\left\langle \delta n^2 \right\rangle' = \frac{\tilde{I}_F\left(0;\omega\right)'}{V}, \tag{5.23}$$

where volume V of the tissue has been known in advance. Eqs. (5.21)-(5.23) and (5.18) can be regarded as the solutions to the inverse-scattering problem. It is shown that to determine three parameters of biological tissue it is necessary to take measurements of the scattered field along three directions in the far zone: spectral density at any arbitrary two directions off the scattering axis, namely θ_1 and θ_2, and the forward direction spectral density θ=0. It can be noticed that the scattered field along the forward direction cannot be practically distinguished from the total field beyond tissue medium (Chapter 13 of [1]), however, the scattered component of the spectral density can be approximated obtained by computing the difference between total field and incident one

$$S^{(s)}\left(0;\omega\right) \approx S^{(t)}\left(0;\omega\right) - S^{(i)}\left(0;\omega\right). \tag{5.24}$$

When determining tissue's parameters, it is also assumed that the incident spectral density $S^{(i)}(\omega)$ and distance r from the medium's origin to reference points located in the far field should also be known. Based on such assumption, only two measurements of the spectral density of the scattered field along the forward direction with and without the bio-tissue, respectively, are needed for running the calculations.

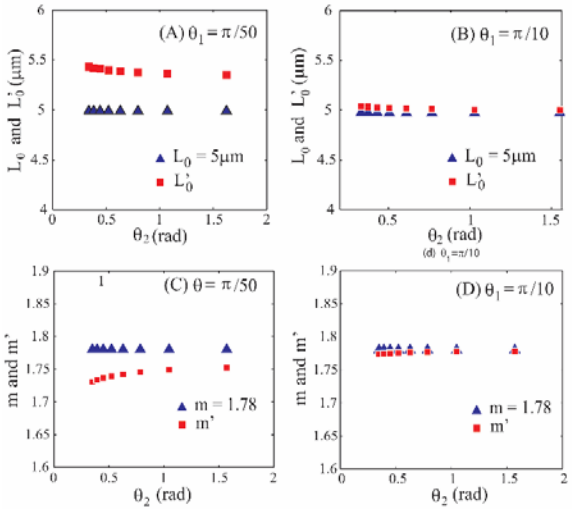

Fig. 5.7 Comparison between the assumed and reconstructed values: (A) and (B) the outer scale (L_0, L_0'); (C) and (D) the fractal exponent (m, m') for the mouse dermis (L_0=5μm, m=1.78). The figures are plotted from Eqs. (5.18) and (5.21) (from Fig. 2 of [119]).

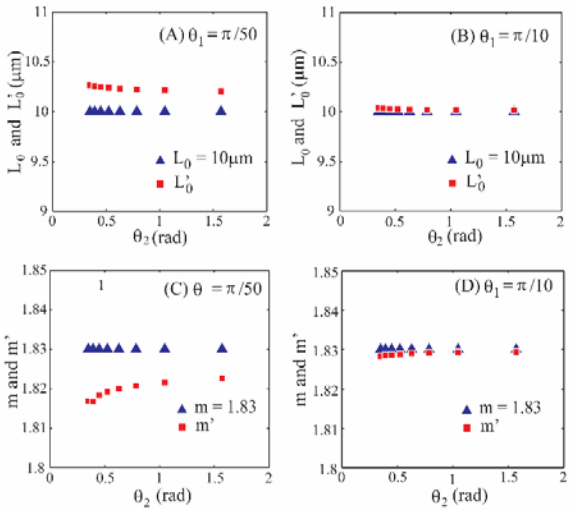

Fig. 5.8 Comparison between the assumed and reconstructed values of (A) and (B) the outer scale (L_0, L_0'); (C) and (D) the fractal exponent (m, m') for the mouse dermis (L_0=10μm, m=1.83). The figures are plotted from Eqs. (5.18) and (5.21) (from Fig. 3 of [119]).

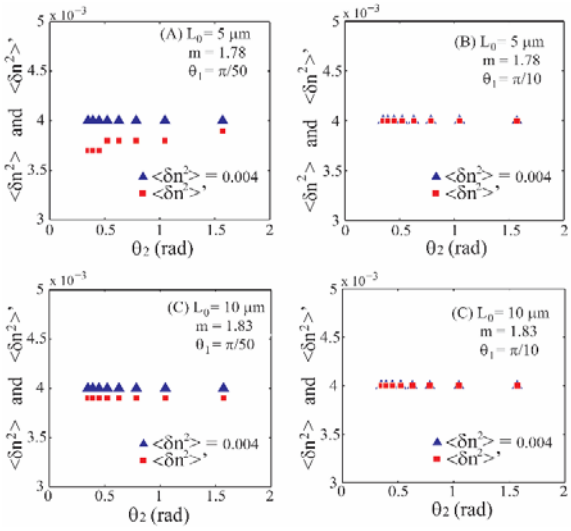

Fig. 5.9 Comparison between the assumed and reconstructed VRI ($\langle \delta n^2 \rangle$ and $\langle \delta n^2 \rangle'$) of biological tissues: (A) and (B) deep dermis of mouse with L_0=5μm, m=1.78;

(C) and (D) intestinal epithelium of mouse with L_0=10μm, m=1.83. The figures are plotted from Eqs. (5.18), (5.22) and (5.23) (from Fig. 4 of [119]).

Plots shown in Figs. 5.7-5.9 specifically compare the original values of tissue parameters and their reconstructed values which are determined from Eqs. (5.18), (5.21)-(5.23): the deep dermis of mouse (L_0=5μm, m=1.78), the intestinal epithelium of mouse (L_0=10μm, m=1.83), and for both types of tissues $\left\langle \delta n^2 \right\rangle = 0.004$. Results indicate that the solution to the inverse problem is valid for various situations where one of two scattering angles is sufficiently small, e.g. $\theta_1=\pi/10$.

5.2.3 Concluding Remarks

In summary, we apply the 3D correlation function of a soft biological tissue to theoretically solve the direct and inverse scattering problems, while the first-order Born approximation is utilized to obtain our primary results. We first evaluate the distribution of angular spectral density of the scattered field throughout the far zone of tissue, and then, propose approaches to use the far-field scattered spectral density to solve the inverse scattering problem: two on-axis measurements, each obtained with and without tissue medium, and off-axis measurements, each obtained at different scattering angles. Based on these measured spectral density values of the scattered field in far zone, we further derive the analytical forms for determining three parameters of bio-tissue. Through comparing the assumed and reconstructed values of tissue parameters we test the validity of our method. These obtained results have potential applications in medical diagnostics as we have provided analytical determination approach to estimate these

parameters of soft biological tissues from several intensity measurements in far-zone scattered field.

Chapter 6

Summary

Throughout all the chapters we have explored several approaches to flexibly tune statistical properties of partially coherent optical fields when they propagate through or scatter from a variety of random media. By appropriately designing either the degree of coherence of a planar source or a correlation function of a 3D medium, we demonstrated the capabilities of modulating the desired far-zone beam properties, including the average intensity distribution, the two-point CIF profile, as well as the scintillation index. The major contributions by the author to the optical community included in this thesis are outlined as follows:

1. Mathematical models are introduced for the class of media which have the capacity to focus the spectral density on or off the scattering axis; or producing a strongly peaked intensity profile along the scattering axis. With suitable design of the correlation function of the medium, a variety of intensity profiles in the far-zone scattered field can be generated. Furthermore, we also introduce the DMR method which can be effectively employed for design of media correlation functions from coherent modes.
2. Three partially coherent beam families are proposed for the first time and their propagation properties through an *ABCD* optical system and atmospheric turbulence are investigated. By using an SLM and coherent He-Ne Laser beam we experimentally generated these beams. Moreover, we also conducted the very first experiment on synthesis of a random, stationary light beam from a laser via superposition of its coherent modes produced on passage through an SLM. These

results are of importance for applications of partially coherent beams in free space optical communications.

3. We present a simple method for measuring the anisotropic factor and ellipse angle of anisotropic turbulence from the two-point light intensity correlation. The method is of importance for designing and optimizing optical systems operating in the presence of anisotropic turbulence: it can be used as a simple technique for determining the parameters of anisotropic turbulence. In addition, we provide experimental verification of observation of the EBS effect of the He-Ne laser beam in the double-passage channel with retroreflector and the heat-induced atmospheric turbulence. These studied situations may appear in a variety of non-classic atmosphere regimes and are of importance for free-space optical communications with retro-modulation.
4. The SI properties of a Gaussian laser beam propagating in an extended isotropic and homogeneous bio-tissue with fractal-like power spectrum of refractive index fluctuations and a finite outer scale are investigated. We have overviewed the spatial power spectra of turbulence for different dimensions envisioning that our study might be of interest in medical imaging and diagnostics. Besides, we also introduced analytical solutions to both the direct and the inverse far-field light scattering problems from a soft biological tissue. This method may be of importance in medical diagnostics providing a simple technique for measuring the parameters of soft biological tissues.

References

1. M. Born and E. Wolf, *Principles of Optics* (Cambridge U. Press, 1999).

2. F. Zernike, "The concept of degree of coherence and its application to optical problems", *Physica***5**, 785-795 (1938).

3. E. Wolf, *Introduction to the Theory of Coherence and Polarization of Light* (Cambridge U. Press, 2007).

4. L. C. Andrews and R. L. Phillips, *Laser Beam Propagation through Random Media* (SPIE Press, 2005).

5. O. Korotkova, *Random Light Beams: Theory and Applications* (CRC Press, 2013).

6. E. Wolf, "Diffraction of radiation of any state of spatial coherence on media with periodic structure", *Opt. Lett.***38**, 4023-4025 (2013).

7. P. Vahimaa and J. Turunen, "Finite-elementary-source model for partially coherent radiation", *Opt. Express***14**, 1376-1381 (2006).

8. O. Korotkova and G. Gbur, "Angular spectrum representation for propagation of random electromagnetic beams in a turbulent atmosphere", *J. Opt. Soc. Am. A***24**, 2728-2736 (2007).

9. G. Gbur and O. Korotkova, "Angular spectrum representation for the propagation of arbitrary coherent and partially coherent beams through atmospheric turbulence", *J. Opt. Soc. Am. A***24**, 745-752 (2007).

10. M. A. Alonso, "Wigner functions in optics: describing beams as ray bundles and pulses as particle ensembles", *Adv. Opt. Photonics***3**, 272-365 (2011).

11. J. W. Goodman, *Speckle Phenomena in Optics: Theory and Applications* (Roberts and Company Publishers, 2007).

12. S. B. Raghunathan, T. D. Visser, and E. Wolf, "Far-zone properties of electromagnetic beams generated by quasi-homogeneous sources", *Opt. Commun.***295**, 11-16 (2013).

13. A. Apostol and A. Dogariu, "Spatial correlations in the near field of random media", *Phys. Rev. Lett.***91**, 093901 (2003).

14. H. Roychowdhury and E. Wolf, "Effects of spatial coherence on near-field spectra", *Opt. Lett.***28**, 170-172 (2003).

15. J. Greffet, M. D. Gutierrez, P. V. Ignatovich, and A. Radunsky, “Influence of spatial coherence on scattering by a particle”, *J. Opt. Soc. Am. A***20**, 2315-2320 (2003).

16. S. Sahin, G. Gbur, and O. Korotkova, “Scattering of light from particles with semisoft boundaries”, *Opt. Lett.***36**, 3957-3959 (2011).

17. L. Mandel and E. Wolf, *Quantum Coherence and Quantum Optics* (Cambridge U. Press, 1995).

18. F. Gori and M. Santarsiero, “Devising genuine spatial correlation functions”, *Opt. Lett.***32**, 3531-3533 (2007).

19. E. Wolf, “New spectral representation of random sources and of the partially coherent fields that they generate”, *Opt. Commun.***38**, 3-6 (1981).

20. F. Gori, “Mode propagation of the field generated by Collett-Wolf Schell-model sources”, *Opt. Commun.***46**, 149-154 (1983).

21. L. C. Andrews and R. L. Phillips, *Laser Beam Propagation in Turbulent Atmosphere* (2nd edition, SPIE Press, 2005).

22. F. Gori, “Collett-Wolf sources and multimode lasers”, *Opt. Commun.***34**, 301-305 (1980).

23. J. Huttunen, A. T. Friberg, and J. Turunen, “Scattering of partially coherent electromagnetic fields by microstructured media”, *Phys. Rev. E***52**, 3081-3092 (1995).

24. C. C. Young, Y. V. Gilchrest, and B. R. Macon, “Turbulence induced beam spreading of higher order mode optical waves”, *Opt. Eng.***41**, 1097-1103 (2002).

25. T. Shirai, A. Dogariu, and E. Wolf, “Mode analysis of spreading of partially coherent beams propagating through atmospheric turbulence”, *J. Opt. Soc. Am. A***20**, 1094-1102 (2003).

26. C. Schwartz and A. Dogariu, “Mode coupling approach to beam propagation in atmospheric turbulence”, *J. Opt. Soc. Am. A***23**, 329-338 (2006).

27. T. Voipio, K. Blomstedt, T. Setala, and A. T. Friberg, “Conservation of electromagnetic coherent mode structure on propagation”, *Opt. Commun.***340**, 93-101 (2005).

28. G. Gbur, *Nonradiating sources and the inverse source problem*, Ph.D. dissertation (University of Rochester, 2002).

29. M. Erkintalo, M. Surakka, J. Turunen, A. T. Friberg, and G. Genty, “Coherent-mode representation of supercontinuum”, *Opt. Lett.***37**, 169-171 (2012).

30. J. Li and O. Korotkova, “Deterministic mode representation of random stationary media for scattering problems”, *J. Opt. Soc. Am. A***34**, 1021-1028 (2017).

31. O. Korotkova, “Design of weak scattering media for controllable light scattering”, *Opt. Lett.***40**, 284-287 (2015).

32. O. Korotkova, “Can a sphere scatter light producing rectangular intensity patterns?”, *Opt. Lett.***40**, 1709-1712 (2015).

33. Y. Wang, H. F. Fchouten, and T. D. Visser, “Tunable, anomalous Mie scattering using spatial coherence”, *Opt. Lett.***40**, 4779-4782 (2015).

34. Y. Wang, S. Yan, D. Kuebel, and T. D. Visser, “Dynamic control of light scattering using spatial coherence”, *Phys. Rev. A***92**, 013806 (2015).

35. Y. Wang, H. F. Fchouten, and T. D. Visser, “Strong suppression of forward or backward Mie scattering by using partial coherence”, *J. Opt. Soc. Am. A***33**, 513-518 (2016).

36. H. Lajunen and T. Saastamoinen, “Propagation characteristics of partially coherent beams with spatially varying correlations”, *Opt. Lett.***36**, 4104-4106 (2011).

37. H. Lajunen and T. Saastamoinen, “Non-uniformly correlated partially coherent pulses”, *Opt. Express***21**, 190-195 (2013).

38. Z. Tong and O. Korotkova, “Nonuniformly correlated light beams in uniformly correlated media”, *Opt. Lett.***37**, 3240-3242 (2012).

39. Z. Mei, Z. Tong, and O. Korotkova, “Electromagnetic non-uniformly correlated beams in turbulent atmosphere”, *Opt. Express***20**, 26458-26463 (2012).

40. J. Li and O. Korotkova, “Scattering of light from a stationary nonuniformly correlated medium”, *Opt. Lett.***41**, 2616-2619 (2016).

41. T. D. Visser, D. G. Fischer, and E. Wolf, “Scattering of light from quasi-homogeneous sources by quasi-homogeneous media”, *J. Opt. Soc. Am. A***23**, 1631-16338 (2006).

42. M. Hunter, V. Backman, G. Popescu, M. Kalashnikov, C. W. Boone, A. Wax, V. Gopal, K. Badizadegan, G. D. Stoner, and M. S. Feld, “Tissue self-affinity and polarized light scattering in the Born approximation: a new method for precancer detection”, *Phys. Rev. Lett.***97**, 138102 (2006).

43. Z. Chen and D. Zhao, “4Pi focusing of spatially modulated radially polarized vortex beams”, *Opt. Lett.***37**, 1286-1288 (2012).

44. C. J. R. Sheppard, “Cylindrical lenses-focusing and imaging: a review”, *Appl. Opt.***52**, 538-545 (2013).

45. J. Pu and P. H. Jones, “Devil’s lens optical tweezers”, *Opt. Express***23**, 8190-8199 (2015).

46. J. Lin, O. G. Rodríguez-Herrera, F. Kenny, D. Lara, and J. C. Dainty, “Fast vectorial calculation of the volumetric focused field distribution by using a three-dimensional Fourier transform”, *Opt. Express***20**, 1060-1069 (2012).

47. J. Li, F. Wang, and O. Korotkova, “Random sources for cusped beams”, *Opt. Express***24**, 17779-17791 (2016).

48. C. Travis, G. Norris, G. McConnell, and G. L. Oppo, “Energy shedding during nonlinear self-focusing of optical beams”, *Opt. Express***21**, 23459-23470 (2013).

49. Z. Yan, Z. Wen, and C. Hang, “Spatial solitons and stability in self-focusing and defocusing Kerr nonlinear media with generalized parity-time-symmetric Scarff-II potentials”, *Phys. Rev. E***92**, 022913 (2015).

50. O. Korotkova, “Random sources for rectangular far fields”, *Opt. Lett.***39**, 64-67 (2014).

51. G. Zheng, D. Ye, X. Peng, M. Song, and Q. Zhao, “Tunable scattering intensity with prescribed weak media”, *Opt. Express***24**, 24169-24178 (2016).

52. J. Li and O. Korotkova, “Random medium model for cusping of plane waves”, *Opt. Lett.***42**, 3251-3254 (2017).

53. X. Xiao, O. Korotkova, and D. G. Voelz, “Laboratory implementation of partially coherent beams with super-Gaussian distribution”, *Proc. of SPIE*, **9224**, 92240N (2014).

54. Y. Li, “Flat-topped beam with non-circular cross-sections”, *J. Mod. Opt.***50**, 1957-1966 (2003).

55. S. Basu, M. W. Hyde IV, X. Xiao, D. G. Voelz, and O. Korotkova, “Computational approaches for generating electromagnetic Gaussian Schell-model sources”, *Opt. Express***22**, 31691-31707 (2014).

56. M. W. Hyde IV, S. Basu, D. G. Voelz, and X. Xiao, “Generating partially coherent Schell-model sources using a modified phase screen approach”, *Opt. Eng.***54**, 120501 (2015).

57. M. V. Hyde IV, S. Basu, D. G. Voelz, and X. Xiao, "Experimentally generating any desired partially coherent Schell-model source using phase-only control", *J. Appl. Phys.***118**, 093102 (2015).

58. M. V. Hyde IV, S. Basu, X. Xiao, and D. G. Voelz, "Producing any desired far-field mean irradiance pattern using a partially-coherent Schell-model source", *J. Opt.***17**, 055607 (2015).

59. G. Gburand E. Wolf, "Spreading of partially coherent beams in random media", *J. Opt. Soc. Am. A***19**, 1592-1598 (2002).

60. O. Korotkova, L. C. Andrews, and R. L. Phillips, "A model for a partially coherent Gaussian beam in atmospheric turbulence with application in LaserCom", *Opt. Eng.***43**, 330-341 (2004).

61. H. T. Eyyuboglu and E. Sermutlu, "Partially coherent Airy beam and its propagation in turbulent atmosphere", *Appl. Phys. B***110**, 451-457 (2013).

62. F. Wang and O. Korotkova, "Random sources for beams with azimuthal intensity variation", *Opt. Lett.***41**, 516-519 (2016).

63. F. Wang, J. Li, G. Martinez-Piedra, and O. Korotkova, "Propagation dynamics of partially coherent crescent-like optical beams in free space and turbulent atmosphere", *Opt. Express***25**, 26055-26066 (2017).

64. F. Wang and O. Korotkova, "Random sources for beams with azimuthally varying polarization properties", *Opt. Express***24**, 15446-15455 (2016).

65. C. Nelson, S. Avramov-Zamurovic, O. Korotkova, S. Guth, and R. Malek-Madani, "Scintillation reduction in pseudo Multi-Gaussian Schell-model beams in the maritime environment", *Opt. Commun.***364**, 145-149 (2016).

66. D. Voelz, X. Xiao, and O. Korotkova, "Numerical modeling of Schell-model beams with arbitrary far-field patterns", *Opt. Lett.***40**, 352-355 (2015).

67. A. Starikov and E. Wolf, "Coherent-mode representation of Gaussian Schell-model sources and their radiation fields", *J. Opt. Soc. Am.***72**, 923-928 (1982).

68. F. Gori, "Mode propagation of the field generated by Collett-Wolf Schell-model sources", *Opt. Commun.***46**, 149-154 (1983).

69. K. Sundar, N. Mukunda, and R. Simon, "Coherent-mode decomposition of general anisotropic Gaussian Schell-model beams", *J. Opt. Soc. Am. A***12**, 560-569 (1995).

70. F. Gori, G. Guattari, and C. Padovani, "Modal expansion for J_0-correlated Schell-model sources", *Opt. Commun.***64**, 311-316 (1987).

71. C. Liang, F. Wang, X. Liu, Y. Cai, and O. Korotkova, "Experimental generation of cosine-Gaussian-correlated Schell-model beams with rectangular symmetry", *Opt. Lett.***39**, 769-772 (2014).

72. S. A. Ponomarenko, "A class of partially coherent beams carrying optical vortices", *J. Opt. Soc. Am. A***18**, 150-156 (2001).

73. M. S. Soskin, V. N. Gorshkov, M. V. Vasnetsov, J. T. Malos, and N. R. Heckenberg, "Topological charge and angular momentum of light beams carrying optical vortices", *Phys. Rev. A***56**, 4064-4075 (1997).

74. V.Arrizón, U. Ruiz, R. Carrada, and L. A. González, "Pixelated phase computer holograms for the accurate encoding of scalar complex fields", *J. Opt. Soc. Am. A***24**, 3500-3507 (2007).

75. X. Chen, J. Li, S. H. Rafsanjani, and O. Korotkova, "Synthesis of I_m-Bessel correlated beams via coherent modes", *Opt. Lett.***43**, 3590-3593 (2018).

76. A. C. Monin and A. M. Yaglom, *Statistical Hydromechanics: Mechanics of Turbulence* (Nauka Press, 1967).

77. A. Consortini, L. Ronchi, and L. Stefanutti, "Investigation of atmospheric turbulence by narrow laser beams", *Appl. Opt.***9**, 2543-2547 (1970).

78. L. Biferale and I. Procaccia, "Anisotropy in turbulent flows and in turbulent transport", *Phys. Rep.***414**, 43-164 (2005).

79. C. Robert, J. Conan, V. Michau, J. Renard, C. Robert, and F. Dalaudier, "Retrieving parameters of the anisotropic refractive index fluctuations spectrum in the stratosphere from balloon-borne observations of stellar scintillation", *J. Opt. Soc. Am. A***25**, 379-393 (2008).

80. V. A. Gladkikh, I. V. Nevzorova, S. L. Odintsov, and V. A. Fedorov, "Turbulence anisotropy in the near-ground atmospheric layer", *Proc. of SPIE*, **9292**, 92925F (2014).

81. F. Wang and O. Korotkova, "Random optical beam propagation in anisotropic turbulence along horizontal links", *Opt. Express***24**, 24422-24434 (2016).

82. M. Cheng, L. Guo, J. Li, and Q. Huang, "Propagation properties of an optical vortex carried by a Bessel-Gaussian beam in anisotropic turbulence", *J. Opt. Soc. Am. A***33**, 1442-1450 (2016).

83. S. Kotiang and J. Choi, "Temporal frequency spread of optical wave propagation through anisotropic non-Kolmogorov turbulence", *J. Opt.***17**, 125606 (2015).

84. L. Cui, B. Xue, and F. Zhou, "Generalized anisotropic turbulence spectra and applications in the optical waves' propagation through anisotropic turbulence", *Opt. Express***23**, 30088-30103 (2015).

85. J. P. Bos, M. C. Roggemann, and V. S. Gudimetla, "Anisotropic non-Kolmogorov turbulence phase screens with variable orientation", *Appl. Opt.***54**, 2039-2045 (2015).
86. Y. Baykal, "Intensity fluctuations of asymmetrical optical beams in anisotropic turbulence", *Appl. Opt.***55**, 7462-7467 (2016).

87. I. Toselli, O. Korotkova, X. Xiao, and D. G. Voelz, "SLM-based laboratory simulations of Kolmogorov and non-Kolmogorov anisotropic turbulence", *Appl. Opt.***54**, 4740-4744 (2015).

88. X. Xiao, D. G. Voelz, I. Toselli, and O. Korotkova, "Gaussian beam propagation in anisotropic turbulence along horizontal links: theory, simulation, and laboratory implementation", *Appl. Opt.***55**, 4079-4084 (2016).

89. F. Wang, I. Toselli, J. Li, and O. Korotkova, "Measuring anisotropy ellipse of atmospheric turbulence by intensity correlations of laser light", *Opt. Lett.***42**, 1129-1132 (2017).

90. J. D. Schmidt, *Numerical Simulation of Optical Wave Propagation, with Examples in MATLAB* (SPIE Press, 2010).

91. M. Beason, L. Andrews, and R. Phillips, "Study on the effect of anisotropy on a propagating beam", *Proc. of SPIE*, **10408**, 104080B (2017).

92. M. Beason, F. Sanzone, J. Coffaro, C. Smith, J. Spychalsky, B. Berry, F. Titus, R. Crabbs, L. Andrews, and R. Phillips, "Near ground measurements of beam shaping and anisotropic turbulence over concrete runway and grass range", *Proc. of SPIE*, **10770**, 107700L (2018).

93. M. Beason, C. Smith, J. Coffaro, S. Belichki, J. Spychalsky, F. Titus, R. Crabbs, L. Andrews, and R. Phillips, "Near ground measure and theoretical model of plane wave covariance of intensity in anisotropic turbulence", *Opt. Lett.***43**, 2607-2610 (2018).

94. M. Beason, J. Coffaro, C. Smith, J. Spychalsky, S. Belichki, F. Titus, F. Sanzone, B. Berry, R. Crabbs, L. Andrews, and R. Phillips, "Evolution of near-ground turbulence over concrete runway throughout multiple days in summer and winter", *J. Opt. Soc. Am. A***35**, 1393-1400 (2018).

95. J. L. Bufton, R. S. Iyer, and L. S. Taylor, "Scintillation statistics caused by atmospheric turbulence and speckle in satellite laser ranging", *Appl. Opt.***16**, 2408-2413 (1977).

96. L. C. Andrews, R. L. Phillips, and W. B. Miller, "Mutual coherence function for a double-passage retroreflected optical wave in atmospheric turbulence", *Appl. Opt*. **36**, 698-708 (1997).

97. L. C. Andrews, R. L. Phillips, and A. R. Weeks, "Rytov approximations of the irradiance covariance and variance of a retroreflected optical beam in atmospheric turbulence", *J. Opt. Soc. Am. A***14**, 1938-1948 (1997).

98. A. N. Bogaturov, A. S. Gurvich, S. S. Kashkarov, and V. A. Myakinin, "Backscattering from different objects in turbulent media", *Waves Random Media***1**, S1-S9 (1991).

99. J. H. Churnside and J. J. Wilson, "Enhanced backscatter of a reflected beam in atmospheric turbulence", *Appl. Opt.***32**, 2651-2655 (1993).

100. R. Mahon, C. I. Moore, H. R. Burris, M. Ferraro, W. S. Rabinovich, M. Suite, and L. M. Thomas, "Probability density of irradiance fluctuations observed over terrestrial ranges", *Appl. Opt.***50**, 6476-6483 (2011).

101. W. Nelson, J. P. Palastro, C. Wu, and C. C. Davis, "Enhanced backscatter of optical beams reflected in turbulent air", *J. Opt. Soc. Am. A***32**, 1371-1378 (2015).

102. D. H. Nelson, D. L. Walters, E. P. Mackerrow, M. J. Schmitt, C. R. Quick, W. M. Porch, and R. R. Petrin, "Waves optics simulation of atmospheric turbulence and reflective speckle effects in CO2 lidar", *Appl. Opt.***39**, 1857-1871 (2000).

103. G. Yang, S. You, M. Bi, B. Fan, Y. Lu, X. Zhou, J. Li, H. Geng, and T. Wang, "Wave-optics simulation of the double-pass beam propagation in modulating retro-reflector FSO systems using a corner cube reflector", *Appl. Opt.***56**, 7474-7483 (2017).

104. J. Li, G. Martinez-Piedra, and O. Korotkova, "Enhanced Back-Scatter in double-pass optical links with non-classic turbulence", *Opt. Express***26**, 10128-10139 (2018).

105. F. Wang, I. Toselli, J. Li, and O. Korotkova, "Finding anisotropic ellipse of atmospheric turbulence by intensity correlations of laser light", in *Aerospace Conference* (IEEE, 2017).

106. W. Gao, "Changes of polarization of light beams on propagation through tissue", *Opt. Commun*. **260**, 749-754 (2006).

107. W. Gao and O. Korotkova, "Changes in the state of polarization of a random electromagnetic beam propagating through tissue", *Opt. Commun.***270**, 474-478 (2007).

108. L. Cui, B. Xue, L. Cao, S. Zheng, W. Xue, X. Bai, X. Cao, and F. Zhou, "Irradiance scintillation for Gaussian-beam wave propagating through weak non-Kolmogorov turbulence", *Opt. Express***19**, 16872-16884 (2011).

109. X. Yi, Z. Liu, P .Yue, “Inner- and outer-scale effects on the scintillation index of an optical wave propagating through moderate-to-strong non-Kolmogorov turbulence”, *Opt. Express***20**, 4232-4247 (2012).

110. O. Korotkova, N. Farwell, and E. Shchepakina, “Light scintillation in oceanic turbulence”, *Wave Random Complex***22**, 260-266 (2012).

111. Y. Baykal, “Scintillation index of optical spherical wave propagating through biological tissue”, *J. Mod. Opt.***64**, 138-142 (2017).

112. L. C. Andrews and R. L. Phillips, *Laser Beam Propagation through Random Medium* (2nd edition, SPIE Press, 2005).

113. X. Chen, J. Li, and O. Korotkova, “Laser light scintillation in soft biological tissues”, *Wave Random Complex*, in press.

114. V. Tuchin, *Handbook of Optical Biomedical Diagnosis: Light-tissue Interaction* (2nd edition, SPIE Press, 2016).

115. J. M. Schmidt, G. Kumar, “Turbulent nature of refractive-index variations in biological tissue”, *Opt. Lett.***21**, 13010-1312 (1996).

116. C. J. R. Sheppard, “Scattering by fractal surfaces with an outer scale”, *Opt. Commun.***122**, 178-188 (1996).

117. C. J. R. Sheppard, “Fractal model of light scattering in biological tissue and cells”, *Opt. Lett.***32**, 142-144 (2007).

118. J. D. Rogers, I. R. Capoglu, and V. Backman, “Nonscalar elastic light scattering from continuous random media in the Born approximation”, *Opt. Lett.***34**, 1891-1893 (2009).

119. J. Li and O. Korotkova, “Direct and inverse problems of weak scattering from quasi-homogeneous biological tissue”, *Wave Random Complex*, in press.

120. W. H. Carter and E. Wolf, “Scattering from quasi-homogeneous media”, *Opt. Commun.***67**, 85-90 (1988).